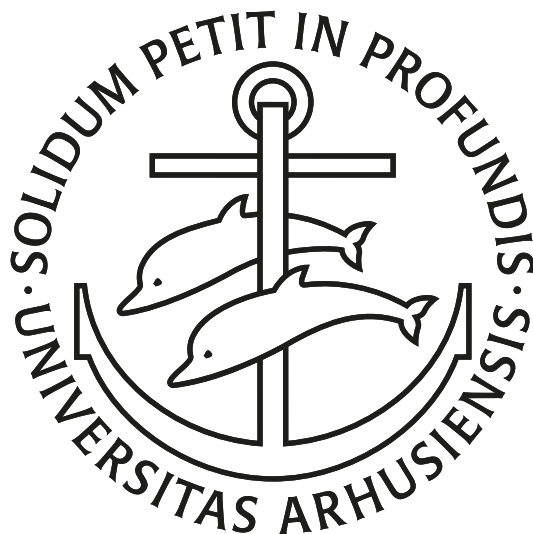


---

# Positronium Formation & Cooling in Meso-Structured Silica Films

---



**SØREN LINDHOLT ANDERSEN**

DEPARTMENT OF PHYSICS AND ASTRONOMY  
AARHUS UNIVERSITY, DENMARK

**PHD THESIS**  
MARCH 2015

Søren Lindholt Andersen  
Department of Physics and Astronomy  
Aarhus University  
Ny Munkegade 120  
8000 Aarhus C  
Denmark  
E-mail: [sla@phys.au.dk](mailto:sla@phys.au.dk)

1<sup>st</sup> edition, March 2015

This thesis has been submitted to the Graduate School of Science and Technology at Aarhus University, Denmark, in order to fulfill the requirements for obtaining the PhD degree in physics. The scientific work presented has been performed in the period from August 2010 to March 2015 under the supervision of Ulrik I. Uggerhøj. The experimental work was carried out mainly at Aarhus University, but also in part at the University College London, England.



---

# Contents

<b>Contents</b>	<b>iii</b>
<b>Acknowledgements</b>	<b>v</b>
<b>List of Publications</b>	<b>vii</b>
<b>Abstract</b>	<b>ix</b>
<b>Dansk resumé</b>	<b>xi</b>
<b>1 Introduction</b>	<b>1</b>
1.1 Positrons . . . . .	1
1.2 Positronium . . . . .	2
<b>2 Slow positrons</b>	<b>7</b>
2.1 Trap based positron beams . . . . .	8
2.2 Characterisation of the Aarhus positron beam line . . . . .	17
<b>3 Meso-structured silica films for positronium production</b>	<b>31</b>
3.1 Glancing angle deposition of SiO <sub>2</sub> . . . . .	31
3.2 Characterisation of the structured films . . . . .	36
3.3 Structured silica films supported by graphene . . . . .	43
<b>4 Positronium formation in solids</b>	<b>47</b>
4.1 Positronium formation in metals and semiconductors . . . . .	47
4.2 Positronium formation in insulators . . . . .	53
4.3 Positronium formation in transmission . . . . .	57
4.4 Quantifying positronium formation . . . . .	64

<b>5</b>	<b>Positronium formation: experiment</b>	<b>69</b>
5.1	Experimental setup . . . . .	69
5.2	Calibrating the $3\gamma$ method . . . . .	72
5.3	Ps emission from meso-structured silica in reflection . . . . .	75
5.4	Ps emission from meso-structured silica in transmission . . . . .	80
5.5	Comparison of SSPALS and the $3\gamma$ method . . . . .	84
<b>6</b>	<b>Ps cooling in meso-structured silica</b>	<b>89</b>
6.1	Collisional cooling of Ps . . . . .	89
6.2	Experimental setup . . . . .	92
6.3	Ps cooling in reflection from meso-structured silica . . . . .	95
6.4	Ps cooling in transmission from meso-structured silica . . . . .	100
<b>7</b>	<b>Conclusions and outlook</b>	<b>107</b>
	<b>Bibliography</b>	<b>109</b>
	<b>List of Figures</b>	<b>119</b>
	<b>List of Tables</b>	<b>127</b>

---

# Acknowledgements

During the past four and a half years I have worked with a number of great people. First, I would like to thank Ulrik I. Uggerhøj for giving me the opportunity to do fundamental research by accepting me as a Phd student. I am truly grateful for his trust in my dispositions, and I thank him many times for his ever-optimistic supervision. Many thanks also to Helge Knudsen for his intriguing interest in the work I do and for his quirky sense of humour. All current and former members of the group also deserves a great thank in particularly for good company at the yearly lunches at Kohalen; Heine D. Thomsen, Kristoffer K. Andersen, Jakob Esberg, Rune Mikkelsen, Tobias N. Wistisen, Rasmus R. Johansen, Jakob B. Overgaard.

I would also like to thank Poul Aggerholm, Per Christensen, Jens Vestergaard, Torben Hyltoft, Folmer Lyckegaard, Bine Hansen and Jacques Chevalier for excellent technical support to the experimental work conducted during these studies.

It has been a great honour to work with leading experts within the field of positron physics at University College London. Thanks to Nella Laricchia for giving me the opportunity to work at UCL during 5 month of my Phd-studies. You welcomed both my family and me in the best way I could think of. A big thank also goes to the rest of Nella's group: Simon Brawley, Michael Shipman, Piers Fransman and especially to Sam Fayers, whom I worked with on the electrostatic beam line at UCL. You have all made my time at UCL much more comfortable by nice demonstrations of the diversities of British culture. I also thank David Cassidy, Adam Deller and Ben S. Cooper for good collaboration regarding both the multi photon ionisation experiment and also for allowing me to bring some samples to UCL for the Ps cooling measurements presented in this thesis.

My time at Aarhus University has also given me some very good friends. Thanks to Kasper L. Laursen, Tobias Basse, Lars F. Paulsen and Jan Engdahl

for the many hours we spend together since we started studying physics in 2006.

At last, I would like to thank Gitte for always being supportive and patient with what I do, and for following me to London for a great summer in 2013. This work was only possible with Gitte's support, and I dedicate it to you and our two children Eigil and Neel, who were both born during my phd studies.

*Søren Lindholt Andersen*  
*Aarhus, March 2015*

---

# List of Publications

## Publications directly related to this thesis

- I **S. L. Andersen**, R. R. Johansen, J. B. Overgaard, J. K. Mortensen, K. K. Andersen, H. D. Thomsen, M. D. Lund, J. Chevallier, H. Knudsen and U. I. Uggerhøj, *Positronium formation from porous silica in backscattering and transmission geometries*, Eur. Phys. J. D **68**, 124 (2014).
- II **S. L. Andersen**, D. B. Cassidy, J. Chevallier, A. Deller, B. S. Cooper, T. E. Wall and U. I. Uggerhøj, *Positronium emission and cooling in reflection and transmission from thin meso-structured silica films*, submitted to Micropor. Mesopor. Mat. (2015).

## Additional publications

- I K. K. Andersen, **S. L. Andersen**, J. Esberg, H. Knudsen, R. Mikkelsen, U. I. Uggerhøj, P. Sona, A. Mangiarotti, T. J. Ketel and S. Ballestrero (CERN NA63), *Direct Measurement of the Formation Length of Photons*, Phys. Rev. Lett. **108**, 071802 (2012).
- II K. K. Andersen, **S. L. Andersen**, J. Esberg, H. Knudsen, R. Mikkelsen, U. I. Uggerhøj, T. N. Wistisen, A. Mangiarotti, P. Sona and T. J. Ketel (CERN NA63), *Experimental investigation of the Landau-Pomeranchuk-Migdal effect in low-Z targets*, Phys. Rev. D **88**, 072007 (2013).
- III K. K. Andersen, **S. L. Andersen**, J. Esberg, H. Knudsen, R. Mikkelsen, U. I. Uggerhøj, T. N. Wistisen, A. Mangiarotti, P. Sona and T. J. Ketel (CERN NA63), *Measurements of the spectral location of the structured target resonance for ultrarelativistic electrons*, Phys. Lett. B **732**, 309-314 (2014).

IV A. I. Williams, D. J. Murtagh, S. E. Fayer, **S. L. Andersen**, J. Chevallier, Á. Köver, P. Van Reeth, J. W. Humberston and G. Laricchia, *Positron moderation and diffusion: W meshes and foils*, submitted to J. Appl. Phys. (2015).

---

# Abstract

In the present studies, the Aarhus positron beamline has been characterised in terms of its performance via measurements of several properties. The main components of the beamline are the source and moderator, the beam transport system, the three-stage Surko trap, and the buncher. Although some inconsistencies occur from time to time, the positron beam is performing momentarily as expected, and pulses of many positrons can be extracted within a short time. The energy spread of the positrons is also very narrow, and simulations show that the buncher only increases the energy spread slightly in the current configuration. Finally, regarding the beam line, a new timing system was implemented in order to maintain a full control of the timing between hardware elements.

After establishing a good quality positron beam, the positrons are to be converted into Ps. This is done in the meso-structured silica films produced via glancing angle deposition. The films have been characterised in terms of morphological properties through quantitative and qualitative analysis of scanning electron micrographs of the films. The results obtained in this analysis were seen to be in good agreement with the results obtained for the Ps emission and cooling. Ways of optimising parameters critical to the formation and cooling of Ps are given.

The formation of positronium has been approached theoretically and the experimental results show the expected behaviour. Two distinct methods are used in the measurements to find the fraction of Ps formed when positrons are impinging upon the meso-structured silica samples. The Ps formation is investigated in the transmission geometry, and the analysis shows that the formation of Ps is strictly dependent upon the stopping of positrons inside the silica sample. Thus, the probability for the Ps to diffuse to the surface is very similar for diffusion from different positions in the sample.

The Ps has been shown to cool down both when formed in transmission

and reflection geometries. And the samples used here can be employed in a geometry where the Ps atoms can be probed optically through the sample itself. This way the longitudinal component of the Ps energy was probed via Doppler spectroscopy using single-shot positron annihilation lifetime spectroscopy to measure the Doppler shifted Lyman- $\alpha$  resonance. Similarly, the transverse energy was probed to reveal the Doppler broadened profile for the transverse Ps energy component.

---

## Dansk resumé

I disse studier er Aarhus positron beamlinen blevet karakteriseret via adskillige målinger af beamets egenskaber. De vigtigste elementer i beamlinen er kilden, moderatoren, beam transport systemet, positronfælden og buncheren. Til trods for visse eksperimentelle udfordringer kunne det lade sig gøre momentant at se en beamline der performer godt, og pulser der indeholder mange positroner kan ekstraheres fra beamlinen indenfor et kort tidsrum. Energispredningen af positronerne er også meget lille, og simuleringer viser at der kun sker en lille grad af forringelse af denne når buncheren comprimerer beamet i tid. Et nyt timing system er blevet implementeret for at kunne opretholde fuld kontrol af timingen mellem forskellige hardware elementer.

Efter etableringen af et positron beam af en god kvalitet konverteres positronerne nu til positronium. Konverteringen sker i de meso-strukturerede silica film, produceret via deponering ved en lille vinkel. Filmene er blevet karakteriseret i forhold til morfologiske egenskaber gennem kvantitativ og kvalitativ analyse af scanning electron micrografer af filmene. De opnåede resultater ses at være i god overensstemmelse med resultaterne fra positronium udsendelse og køling. Der gives også forslag til hvordan parametre der er kritiske for positronium dannelse og køling kan optimeres.

Positroniums dannelse diskuteres teoretisk og de eksperimentelle resultater viser den forventede opførsel. To forskellige metoder anvendes her til at finde positronium dannelsesforholdet når positronerne skydes ind i de strukturerede silica targets. Positronium dannelsen undersøges både i transmissions og reflektions geometrien og afhænger entydigt af, hvor i target den enkelte positron bliver stoppet. Derfor er sandsynligheden for at det dannede positronium difunderer til over overfladen stort set konstant for diffusion fra forskellige dybder i filmen.

Positronium køling er blevet vist både for dannelse i transmissions og i reflektions geometrierne. De prøver der bruges her kan anvendes i en geometry,

hvor positronium atomet kan probes optisk gennem prøven selv. Sådan blev den longitudinale komponent af positronium energien probet via Doppler spectroscopy med brug af enkelt-skuds positron annihilation levetids spectroscopi til måling af Lyman- $\alpha$  resonansen i positronium. På samme måde blev den transversale energikomponent målt via en måling af Doppler forbredningen.

---

# Introduction

Central to the work presented in this thesis is the creation of positrons and in particular positronium. The elementary positron plays a role in many aspects of physics and constitutes - as the antiparticle of the electron - one of the building blocks of the standard model of physics. In the context of this thesis the application of non-relativistic low energy positrons to the formation of positronium (Ps) - the bound state of an electron and a positron - is of main interest. The present chapter shortly introduces the low energy positron and fundamental properties of positronium.

## 1.1 Positrons

The positron is the antiparticle of the electron. It was predicted by Dirac in 1931 [1] as an interpretation of the negative energy eigenvalues of the Dirac equation and found experimentally two years later by Anderson [2] in the famous experiment illustrated in Fig. 1.1. According to the CPT theorem the positron has the same mass, lifetime and gyromagnetic as the electron, whereas the charge of the positron is  $+e$  in contract to  $-e$  for the electron. This implies also that the free positron is a stable particle that can life for a long time in the interstellar media before it eventually annihilates [3]. Positrons are created in two distinct interactions: (i) by pair creation from a photon of energy above the sum of the rest mass of the electron and the positron,  $\hbar\omega = 2 \times 511\text{keV}$ , and (ii) via  $\beta^+$  decay of radioactive nuclei. The latter process is the most common method to create positrons in the laboratory, and it is also used in the present work as a source of positrons. However, for the positrons to be useful for the purposes described here they must be moderated in energy so form a monoenergetic beam.

Once the low energy positrons have been created they can be used in a range of scientific applications such as antihydrogen production [4], scat-

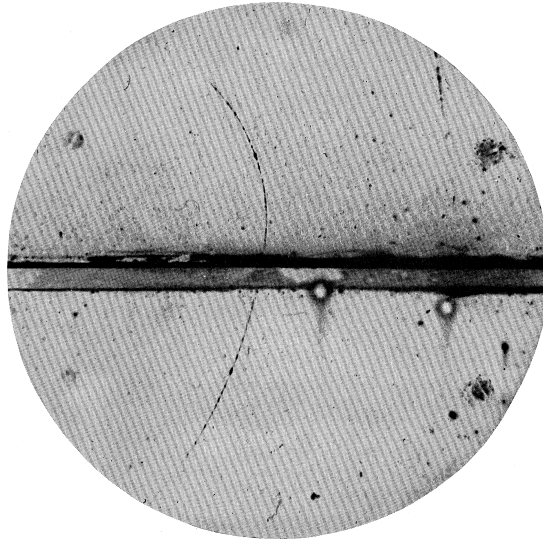


**Figure 1.1:** The positron was first observed by Anderson in 1933, who interpreted the loss of energy of a positive particle passing through a lead plate in a magnetic field as being due to a positron entering from below. From [2].

tering experiments with gasses [5] and characterisation of porous materials [6]. Positrons also find applications within medicine where the technique of positron emission tomography (PET) [7] is an indispensable imaging tool for diagnosis within oncology. The most important property and application of positrons in this work is the ability to form Ps upon implantation into different materials, and in particular for form Ps inside the specially produced meso-structured silica samples to be described in Chapter 3.

The production of a monoenergetic pulse beam of low energy positrons in a trap-based beam system is discussed in detail in Chapter 2 and the implications of positron implantation into the meso-structured silica is a major theme throughout the thesis.

## 1.2 Positronium

The formed Ps can be employed in several experiments such as Ps scattering experiments [8] and antihydrogen production [9]. But Ps is also interesting in its own right where exciting experiments include gravitational measurements on Ps [10, 11], Bose-Einstein condensation of Ps [12], precision tests of bound state QED [13] and the Ps-Ps interaction in porous silica that led to the production of the dipositronium molecule [14]. For the present studies the focus is on the production and cooling of Ps in meso-structured silica

films [15, 16]. The silica samples used here can be employed in a transmission geometry, which is practical in many experiments, and measurements of Ps formation and cooling both in reflection and in transmission geometries will be presented. The basic properties of free Ps are considered below.

The energy eigenvalues of the Ps Hamiltonian,  $H$ , can be found by solving the non-relativistic Schrödinger equation for the two-body problem,  $H\psi(\mathbf{r}_1, \mathbf{r}_2) = E\psi(\mathbf{r}_1, \mathbf{r}_2)$ , after separation of the time variable from the spacial variables. The procedure is very similar to that of the hydrogen atom. However, as a consequence of the CPT theorem, the mass and magnetic moment of the electron and the positron are equal. Therefore the reduced mass of the system is half the mass of the electron (and positron),  $m_\mu = m_{e^-}/2$ , and the results from hydrogen can be scaled to apply for Ps. The spacial extent of Ps is thus twice the Bohr radius,  $2a_0 = 1.06 \text{ \AA}$ , and the  $E_n = -\frac{1}{2}m_\mu c^2 \frac{\alpha^2}{n^2}$ , where  $\alpha$  is the fine structure constant. The binding energy of Ps in vacuum is half the binding energy for hydrogen,  $E_{B,\text{vacuum}} = \alpha m_\mu c^2 / 2 = 6.80 \text{ eV}$ . Corrections to the Bohr energies can be calculated from perturbation theory, and since Ps is a purely leptonic system it is a good candidate for both experimental and theoretical precision studies of bound state QED [13].

Because the magnetic moments of the electron and the positron are equal, the hyperfine splitting is much larger in Ps than in hydrogen, and the spin-spin coupling is made before the spin-orbit coupling. The hyperfine splitting provides new energy eigenstates that can be found from linear combinations of the old eigenstates,  $|m_{s,e^-}, m_{s,e^+}\rangle$ , in which the individual spins give the good quantum numbers.

From the two spin-1/2 particles one can form a singlet of total spin  $S = 0$  that is anti symmetric,

$$|S = 0, M_S = 0\rangle = \frac{1}{\sqrt{2}} (|\uparrow_{e^-}, \downarrow_{e^+}\rangle - |\downarrow_{e^-}, \uparrow_{e^+}\rangle), \quad (1.1)$$

and a triplet with total spin  $S = 1$  consisting of three eigenstates,

$$|S = 1, M_S = -1\rangle = |\downarrow_{e^-}, \downarrow_{e^+}\rangle, \quad (1.2)$$

$$|S = 1, M_S = 0\rangle = \frac{1}{\sqrt{2}} (|\uparrow_{e^-}, \downarrow_{e^+}\rangle + |\downarrow_{e^-}, \uparrow_{e^+}\rangle), \quad (1.3)$$

$$|S = 1, M_S = +1\rangle = |\uparrow_{e^-}, \uparrow_{e^+}\rangle. \quad (1.4)$$

So the spin-spin coupling splits the ground state energy into two distinct energy levels due to the two eigenvalues of  $\mathbf{S}^2$ ,  $S = 0, 1$ , called para-Ps and ortho-Ps, respectively. With the general nomenclature being  $n^{2S+1}L_J$ , the singlet is written as  $1^1S_0$ , and the triplet is written as  $1^3S_1$ . In the ground state of positronium,  $n = 1$ , and therefore  $L = 0$  so there is no energy shift or additional splitting due to the spin-orbit coupling. However, the usual relativistic

correction and a correction due to the motion of the centre of mass of the system do shift the energy. The energy is also shifted by a correction that stems from the probability that the positron and the electron annihilate.

To lowest order in perturbation theory the energy difference between para-Ps and ortho-Ps is found to be  $\Delta E_{1^1S_0-1^3S_1} = 0.846\text{meV}$ , but more advanced calculations in QED yields the more precise value of [13]

$$\Delta E_{1^1S_0-1^3S_1} = 0.841\text{meV} . \quad (1.5)$$

With this very small energy splitting the kinematics of Ps formation ensures an equal formation of Ps in the four states that constitutes the ground state. The energy levels for  $n = 1$  and  $n = 2$  are shown in Fig. 1.2, where the Lyman- $\alpha$  transition is also shown. This transition can be driven optically to measure the emission energy of Ps formed in a given sample via Doppler spectroscopy [17]. This is exactly what was done for the experiment described in Chapter 4 and [16]. In the experiments to be described here the ionisation is facilitated by the absorption of a second photon by Ps in the excited state, and the resonance wavelength can be revealed.

When Ps is formed in vacuum it will decay into a number,  $n_\gamma$ , of photons with a rate that is characteristic of the total spin state in which it is created. The spin states of the Ps ground state are eigenstates of parity,  $P$ , and charge conjugation,  $C$ . The eigenvalue equation for the parity operator gives

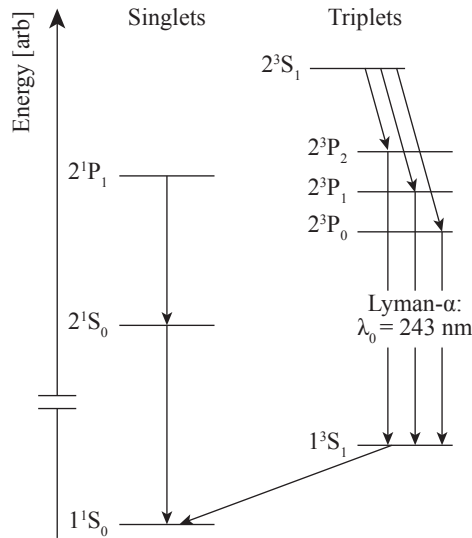


**Figure 1.2:** The  $n = 1$  and  $n = 2$  energy levels of Ps separated into singlet and triplet states. The Lyman- $\alpha$  transition driven by the UV laser in the Ps cooling experiment described in Chapter 6 is also shown. Adapted from [5].

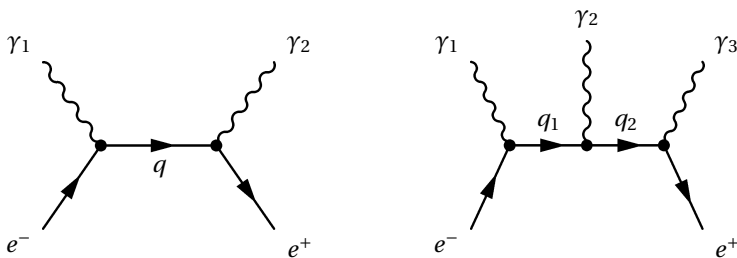


**Figure 1.3:** Feynman diagrams for the decay of para-Ps (left) into two photons and ortho-Ps into three photons (right). The time is running upwards.

an eigenvalue, which is a product of the eigenvalues of the spacial wave function and the spin state, and parity conservation in the decay process constrains the parity of the final state. The charge conjugation operator again yields an eigenvalue which is  $(-1)^{L+S}$ , and because the charge conjugation of a photon state with  $n_\gamma$  photons gives  $C | n_\gamma \rangle = (-1)^{n_\gamma} | n_\gamma \rangle$ , the conservation of  $C$  determines a selection rule for the number of photons in the decay [18]. It is clear that for the ground state  $L = 0$ , and  $(-1)^{L+S} = (-1)^S = (-1)^{n_\gamma}$ . Therefore, the ground state singlet can only decay into an even number of photons, while the triplet state only decays into an odd number of photons. This is illustrated in Figure 1.3, where the annihilation of ground state Ps is seen. The decay into one photon is forbidden due to energy- and momentum conservation for positronium in vacuum. Other possibilities for Ps annihilation presupposes the transfer of momentum to for instance the nucleus of a gas or structures in the local region where Ps exists. Thus for pick-off annihilation with the pore wall in porous silica, the annihilation into one photon is also possible. The typical decay of excited states goes through the ground state first before annihilation, since this process has the largest probability of occurring.

We now go back to the decay rates of positronium (to be considered more detailed in the next chapter). The available phase space of final states is larger for the decay into fewer photons, and the decay of para-positronium into  $n_\gamma = 2$  photons,  $(e^+ + e^-)_{S=0} \rightarrow 2\gamma$ , is more likely to occur than the decay of ortho-positronium into  $n_\gamma = 3$  photon,  $(e^+ + e^-)_{S=1} \rightarrow 3\gamma$ . The decay rate of para-positronium is therefore larger than the decay rate of ortho-positronium, corresponding to a longer lifetime of ortho-positronium than for para-positronium. The lifetimes can quite easily be obtained to lowest order from the Feynman rules and the diagrams in Figure 1.3, but to obtain the most precise results, one must do some complicated calculations, where higher order Feynman diagram are included.

The best result found from such calculations for the lifetime of para- and

ortho-Ps respectively are (from [13] and [19]):

$$\tau_{2\gamma}(1^1S_0) = 125.1623(6)\text{ps}, \quad \tau_{3\gamma}(1^3S_1) = 142.0459(2)\text{ns}, \quad (1.6)$$

which are the vacuum lifetimes of Ps. The actual lifetime is reduced due to pick-off annihilations at the vacuum chamber or other parts in the vicinity of the Ps formation site.

In the following chapters I will give a comprehensive discussion of the Ps formation and cooling in the meso-structured silica films (discussed in Chapter 3) both in the reflection and transmission geometries .

## Slow positrons

The slow positron beam utilised in the experiments conducted in Aarhus originates from the trap-based positron beamline, which was acquired by the ASACUSA collaboration [20] in 2008 and located at Aarhus University for commissioning. The beamline is a turnkey device developed by First Point Scientific, Inc. (FPSI) [21, 22] and consists of a sodium-22 source, a rare gas moderator, and a three stage Surko trap with a rotating wall compression implemented on the third stage. The positrons are magnetically guided along the beam axis to ensure easy beam transport, and ultra-high vacuum ( $\sim 10^{-9}$  mbar) is maintained using turbo molecular pumps as roughing for an ion- and a cryogenic pump (see Figure 2.1). The Aarhus positron beamline including the recent buncher extension and the new trigger system is discussed in the

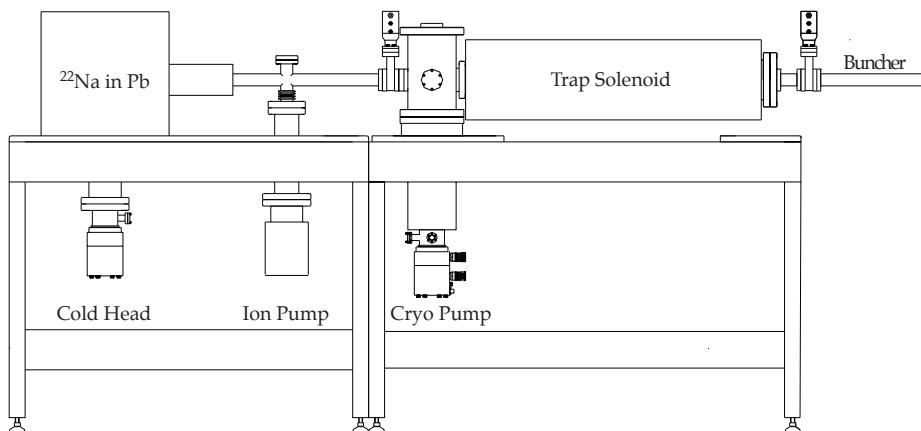


**Figure 2.1:** Overview of the Aarhus positron beam line. The first section contains the source and rare gas moderator, whereas the second section includes the trap and the buncher. Modified from original FPSI drawing.

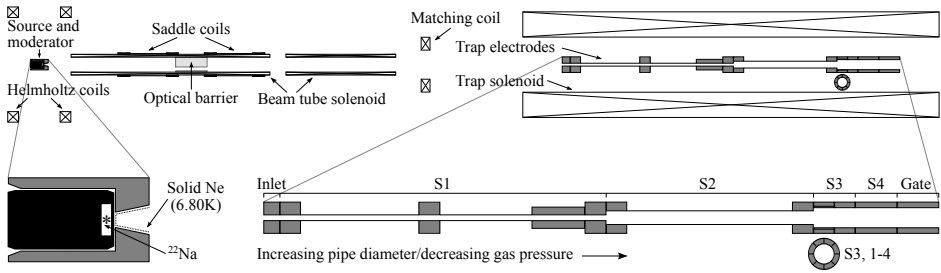
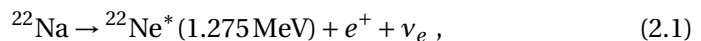


**Figure 2.2:** The electromagnets and the electrodes comprising the Aarhus positron beamline. Enlarged is the moderator geometry to the left showing the solid neon layer evaporated onto the cone shaped gold-plated copper electrode, and to the right the trap electrode configuration with the azimuthally segmented electrode that provided the rotating quadrupole field to one end of the plasma. Modified from original FPSI drawing.

present chapter. The trap-based beamline at UCL used for the energy measurements of the Ps formed in the thin porous silica targets is quite similar to the Aarhus positron beamline. The minor differences between the two beamlines will be described in Chapter 6, where the experiment is also presented.

## 2.1 Trap based positron beams

The source of positrons in the Aarhus positron beam line is a  $^{22}\text{Na}$   $\beta^+$ -emitter (31 mCi by 1. November 2013) acquired from iThemba LABS in South Africa. It is energetically favourable for the unstable  $^{22}\text{Na}$  isotope to decay into an excited state of neon-22,



under the emission of a positron at an energy ranging from 0eV to the Q-value,  $Q = 546\text{keV}$ . The excited state,  $^{22}\text{Ne}^*$ , decays almost immediately into the ground state under the emission of a 1.275MeV photon that can be used to time-tag the decay. To avoid radioactive exposure to any personnel, the source sits internally in a vacuum compatible Elkonite shield that is covered externally with lead shots. The magnetic field from a Helmholtz configuration around the source directs the positrons toward the cone shaped rare gas moderator that serves to transform the broad positron energy distribution into a beam of monoenergetic low energy positrons (see Figure 2.2). The half-life of the decay is  $t_{1/2} = 2.60\text{y}$  with a branching ratio of 0.91 for  $\beta^+$  emission, and sodium-22 is chosen as a compromise between half-life, branching ratio and the commercial availability of a high activity at an affordable cost.

### 2.1.1 Positron moderation

Various moderator materials and geometries have been employed in the past [23] all with the aim of maximising the efficiency of low energy positron emission. When a positron is emitted from the source and impinges upon the moderation material it loses energy by inelastic collisions (the processes responsible for positron energy loss are described in detail in Chapter 4). For metals, semiconductors and insulators the energy is lost primarily via electron-hole pair creation at higher energies. In metals plasmon excitations become evident at a few tens of eV, while phonon scattering takes care of the last few eV such that in a metal the positron thermalises in a few picoseconds. In semiconductors and insulators electron-hole pair creation is inhibited below the band gap energy, and phonon scattering is the only possibility for energy loss, causing a longer thermalisation time.

For a thermalised positron to be able to diffuse to the surface of a solid it must thermalise within the diffusion length of that solid. The moderator efficiency is defined as the rate of positrons emitted into a low energy beam divided by the source activity, and can also be expressed as

$$\epsilon_{\text{mod}} = y_0 L_+ / R, \quad (2.2)$$

where  $y_0$  is the branching ratio for the positrons to be emitted at the surface,  $L_+$  is the diffusion length of positrons in the solid and  $R$  is the mean range of positrons impinging upon the solid [24]. From this expression it is seen that a high efficiency is obtained if the range of positrons is small and all positrons can be deposited near a surface. This is not possible for positrons emitted from a radioactive source and the broad range of implantation depths sets a natural limit to the moderation efficiency. However, if a moderated beam of positrons enter a second remoderation stage, a much higher moderation efficiency can be reached due to the increased control of implantation depth (a remoderation stage is used in the electrostatic beamline at UCL that I worked at for 5 month during my Phd-studies).

The most efficient moderators known to date are the rare gas moderators with  $\epsilon_{\text{mod}}$  approaching 1% [25]. In Figure 2.3 the re-emission of positrons from solid neon kept at 5K is shown as a function of the positron impact energy. The re-emission probability is seen to decrease at energies just above zero due to trapping at the surface. At the energy  $E_{\text{th}} = 16\text{eV}$  the positron energy becomes large enough that Ps can form, which is possible up to the band gap energy,  $E_g = 21.5\text{eV}$ , as described in more detail in Chapter 4. Above  $E_x = 17.5\text{eV}$  exciton bound states may form, and above  $E_g$  electron-hole pairs can be excited. More relevant to the discussion here is the fact that the only energy loss mechanism available below  $E_{\text{th}}$  is inelastic phonon scattering, which in solid neon is even limited to acoustical phonons, and the energy

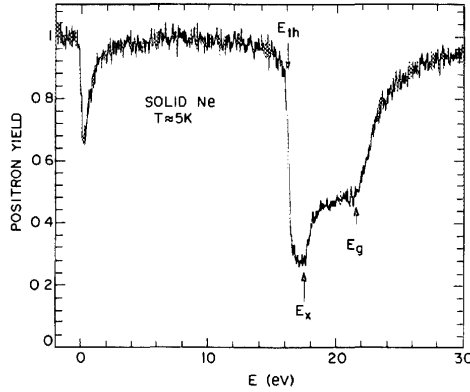


**Figure 2.3:** The positron reemission probability for positrons impinging upon solid neon at 5K for a given positron impact energy. The dip just above zero and the characteristic energies pointed out by arrows are explained in the text. From [25].

loss rate is very low since only  $\sim 6\text{meV}$  is lost in each collision [26]. Thus the effective diffusion length in solid neon becomes very long compared with metallic moderators, and the probability for the positrons to reach a surface (reflection or transmission) is high although the positrons have not fully thermalised when they get there. Also shown in Ref. [25] is the fact the energy distribution becomes narrower for higher energy implantation. This is a consequence also of the long diffusion length and the fact that at higher implantation energies the moderator thickness has to be larger for the positrons to stop in the material compared to lower energies. This results in the onset of phonon scattering at larger depths allowing more collisions and a larger degree of energy loss on average before the positrons reach the surface.

Whether the positrons are able to be emitted from the solid once they reach the surface can be determined by the value of the positron work function defined as the energy required to move a positron from a point inside the solid to a point just outside the solid. It is given by

$$\phi_+ = -D + \mu_+ , \quad (2.3)$$

where  $D$  is the surface dipole potential and  $\mu_+$  is the positron chemical potential. The value of  $\phi_+$  plays an important role in determining the branching ratio for positron emission at the surface, which for thermal positrons is only possible if the work function is negative,  $\phi_+ < 0$ . The more negative the work function gets, the higher the probability of positron emission (which is essentially why a single crystal tungsten foil is found to be an efficient positron moderator). In the case of a positive work function, the positron energy is typically too low to penetrate the positron surface barrier. An exception to this is solid rare gas moderators, which are characterised as hot (epithermal)

positron emitters, *i.e.* even though  $\phi_+ > 0$  for these materials, the positrons will be emitted from the surface with large probability. The reason for this is again the long effective diffusion length causing a high degree of incomplete thermalisation in the bulk and a large probability of overcoming  $\phi_+$ . The cost of high moderator efficiency in rare gas solids is a higher positron emission energy with a larger angular divergence compared to the metallic moderators. To keep the moderator efficiency high in all kinds of moderators, it is essential to avoid defects, and the introduction of potential trapping sites at the surface. This means having a very pure source of gas for solid neon moderators, and it means annealing the tungsten single crystal moderators at temperatures  $> 2000\text{K}$ . However, whilst important to avoid contamination in the bulk to avoid trapping, it has been shown that introducing water to the solid rare gas surface leads to an increase in moderation efficiency [27] and thus the surface dipole potential may be tailored by small contaminants that decrease  $\phi_+$ .

The use of a conical geometry has been shown to significantly improve the moderation efficiency of a solid neon moderator [28], and it is used in the present setup where neon is admitted onto the cold (6.8K) moderator electrode via a thin needle at a typical rate of 2.00 standard cubic centimeter (sccm). The source and moderator is isolated electrically from the cold head by a sapphire disk that on the other hand provides a good thermal conduction, and are raised to a potential of typically 6.8V (see table 2.2 for values of the source potential while the trap is running). The moderator diameter is 8mm which defines the beam size in the magnetic field at the source position, and the expected emission energy is  $\sim 1\text{eV}$  plus the source bias with a typical energy spread of 1.7eV [21].

During the past four years we have experienced several problems with the coldhead used to achieve the low temperature required for the solid neon moderator. From time to time it has been impossible to reach the required temperature, or even to cool down the moderator stage at all. The use of one of the other rare gasses, Argon, Krypton or Xenon instead of Neon has been considered, but the low energy positron yields are smaller for these rare gasses and the energy spread is larger [26]. Therefore it is not necessarily an advantage to use another moderator compared to operating the beamline with a reduced moderator efficiency for neon.

A promising possibility to increase the positron moderation efficiency and to avoid the cryogenics issues mentioned above is to introduce an external potential to cause a drift of positrons toward the surface, thus effectively increasing the diffusion length. This is the principle behind field-assisted moderators. A field-assisted moderator could be made from a diamond with suitable electrodes to apply an external field to the insulator, and it is here proposed to sandwich the diamond between two monolayers of graphene form-

ing a capacitor-like structure. The large negative work function of diamond [29] might become larger once graphene has been introduced, and with the large electron mobility in graphene, charge can easily be added or removed from the surface causing a uniform electric field in the diamond that adds drift to the positrons. If the diamond is thick enough that the positrons will stop on average inside the bulk, then the drift to the surface is enhanced by the electric field present there.

### 2.1.2 Magnetically guided positrons

As shown in figure 2.2 the source and moderator are located inside a Helmholtz configuration that provides a homogeneous magnetic field directed along the beam axis. The positrons emitted from the moderator are immediately guided towards the beam tube solenoid that confines the positrons to the beam axis where they are transported in a cyclotron motion along the field lines due to the Lorentz force. Shortly after the positrons have left the lead shielded area, a set of saddle coils add a small perturbation to the longitudinal magnetic field in the  $-y$  direction to bend the positrons around an optical barrier. This barrier serves to stop unmoderated positrons, 511 keV annihilation  $\gamma$ -rays and 1.275 MeV photons from the decay of  $^{22}\text{Ne}^*$ , while moderated positrons of the right energy are guided smoothly through a hole in the barrier, which is positioned off-axis. Next, the positrons pass a pumping restriction<sup>1</sup> positioned between the ion pump and the cryo pump and inserted to maintain a low pressure in the source and moderator area while the trapping gasses are let into the trap (a pressure difference of two to three orders of magnitude can be maintained in this setup). The magnetic field lines from a long solenoid diverge quite quickly outside the solenoid and to avoid a large beam divergence with mirroring effects to follow when the positrons enter the large field in the trap, a matching coil has been inserted right before the cryo pump. Inside the trap the (relatively) large magnetic field from the trap solenoid ensures a confinement transverse to the beam axis while the trap electrodes provide a longitudinal trapping as described below. The typical magnetic fields of all the magnets in the primary beamline are listed in table 2.1 and can be set in the labVIEW program that controls the system.

### 2.1.3 The positron trap

The moderated positrons are guided into a modified Penning-Malmberg trap [30] consisting of a solenoid magnet providing a uniform longitudinal mag-

---

<sup>1</sup>For some time there was a significant loss of positrons at the pumping restriction which was found to be caused by an unexpected misalignment of the saddle coils, possibly introduced during a laboratory refurbishment.

Magnet	Magnetic field [G]
Helmholtz coils	120
Beam tube solenoid	250
Saddle coils	21
Matching coil	150
Trap solenoid	500

**Table 2.1:** Summary of the default values of the magnetic positron transporting system in the main part of the beamline (source, moderator and trap).

netic field to confine the positrons transversally and a set of cylindrical electrodes arranged to trap the positrons in the longitudinal direction. The trap electrodes form a potential well in which the positrons can be trapped if non-conservative forces act on the positrons while inside the potential well. In the present setup (see Fig. 2.2), the buffer-gas technique is employed to act non-conservatively on the positrons that will lose energy by inelastic collisions with a gas. The trap is divided into three stages with an increasing electrode diameter. The buffer gas ( $N_2$ ) is let into the first stage at a constant rate (0.20 sccm), and the increasing diameter provides a differential pumping that ensures a pressure gradient along the beam axis. As illustrated in Fig. 2.4a from [22], the drop in pressure is accompanied by a potential drop, and a low pressure at the bottom of the trap can be maintained to ensure long storage

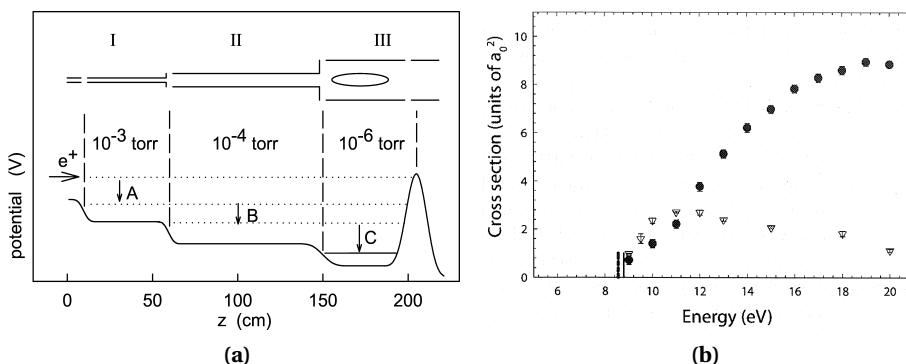


**Figure 2.4:** In (a) the structure of the potential well in the three stages of decreasing buffer gas pressure is shown. The positrons undergo the transition "A", "B" and "C" and become trapped in the third, low pressure stage (from [22]). (b) shows the cross-sections for Ps formation (filled circles) and electronic excitation of the  $a^1\Pi$  state (open triangles) in  $N_2$  by positron impact at a given energy. The dashed- and full line mark the threshold for electronic excitation and Ps formation, respectively (from [31] who summarises results from [32]).

times by avoiding losses via Ps formation or direct annihilation. Yet a large efficiency of trapping due to the high pressure in the first stage can be obtained.

The positron energy and the gas pressure should be adjusted to yield an average of one inelastic collision pr. passage of the first stage to optimise the trapping efficiency [33]. The positrons will thus undergo the transition "A" (see Fig. 2.4a) in the first encounter with the trap electrodes and become trapped between the inlet electrode and the gate electrode. Within the first  $\sim 100\mu\text{s}$ , bouncing back and forth a few times, they will lose energy in the transition "B", and after a few ms undergo the transition "C" to be trapped in the low pressure region of the third stage (S3).

Different buffer gasses have been tested for the buffer gas positron accumulation with varying success [34], but with  $\text{N}_2$  as a superior choice. This is due to the positron impact cross sections for nitrogen as shown in Fig. 2.4b from [31] that summarises results from [32]. At positron energies of  $\sim 10\text{eV}$  the probability of positron impact excitation to the electronic  $a^1\Pi$  state of  $\text{N}_2$  is larger than the cross section for Ps formation. The threshold energies for excitation and Ps formation in molecular nitrogen are 8.59 eV and 8.78 eV, respectively [32], a property which is somewhat unique for this gas [31]. This means that the positron energy in the first stage should be adjusted as close as possible to the threshold energy of the electronic excitation, yet it is essential to avoid cutting of the low energy tail of the (Gaussian profiled) positrons arriving from the moderator. When optimising the positron energy one should also have in mind that the parallel energy spread is increased due to a larger magnetic field in the trap than in the source. In the case of a solid Ne moderator, the maximum trapping efficiency obtained with  $\text{N}_2$  is about 30%. However, this requires careful optimisation of the alignment of the trap electrodes with the magnetic field and the incoming continuous supply of positrons. It is also essential to avoid contamination of the system by oil based vacuum pumps, since only a small amount of hydrocarbons in the system can degrade the trapping efficiency because of the large annihilation cross section for positrons with these molecules [31].

To make a useful beam of low energy positrons additional cooling must be provided once the positrons have been trapped in stage 3. Since the cross sections for vibrational- and rotational excitation of  $\text{N}_2$  by positron impact is low, the cooling time would be quite long if only molecular nitrogen was used ( $\sim 1\text{s}$  for a pressure  $\sim 10^{-6}\text{mbar}$  in the third stage [34]). If on the other hand the magnetic field in the trap was very high ( $\gtrsim 1\text{T}$ ) the positron plasma would cool quickly from cyclotron radiation, but in the present setup, the magnetic field is only 500 G, and the cyclotron cooling is too slow. Therefore a small amount of  $\text{SF}_6$  (used here) or  $\text{CF}_4$  is added to the third stage (at a constant rate of 0.05 sccm) to provide an efficient cooling of the positrons.

These gasses are very effective in cooling the positron plasma even if only a small amount is present in the trap ( $\sim 10^{-7}$  mbar) because of a very large cross-section of vibrational excitation for the asymmetric stretch [35]. Thus a fast cooling time ( $\sim 83$  ms at  $1.2 \cdot 10^{-7}$  mbar for  $\text{SF}_6$  [34]) can be achieved with a limited loss of positrons due to annihilation and it is possible to extract a beam of positrons with a small spread in energy if a mixture of  $\text{N}_2$  and  $\text{SF}_6$  is used.

If a large number of positrons are accumulated in the trap, the positron cloud can be described as a non-neutral plasma *i.e.* if the criteria  $\lambda_D \ll R_p, L_p$  is met, where  $R_p$  is the radial extent of the plasma,  $L_p$  is the length of the plasma and the Debye length is given by  $\lambda_D = \sqrt{\epsilon_0 kT / n_p e^2}$ . In this expression,  $kT$  is the thermal energy of the plasma and the central density of positrons is given by

$$n_p = \frac{N_{e^+}}{2\pi\sigma^2 L_p}, \quad (2.4)$$

for the Gaussian standard deviation of the beam profile,  $\sigma$ , and the number of positrons,  $N_{e^+}$ . The dynamics of a positron plasma in a Surko trap is described by collective phenomena. For instance, the radial electric field in the plasma combined with the magnetic field from the trap solenoid,  $B$ , causes a collective  $E \times B$  drift motion around the beam axis at a frequency

$$f_E = \frac{n_p e}{4\pi\epsilon_0 B}, \quad (2.5)$$

where  $e$  is the individual positron charge and  $\epsilon_0$  is the vacuum permittivity. Another important property of a plasma is the conservation of the canonical angular momentum given by:

$$P_\theta \approx -\frac{m_e \omega_c}{2} \sum_i r_i^2, \quad (2.6)$$

where  $\omega_c$  is the cyclotron frequency and  $r_i$  are the radial positions of the positrons. An outward transport of positrons in the trap is only possible if a torque is exerted on the plasma *e.g.* by positrons scattering with the buffer- or cooling gas or imperfections in the electromagnetic fields. Otherwise the positrons will stay trapped in a steady state. On the other hand it is also possible to inject angular momentum into the plasma to counteract the outward transport and even cause an inward transport and compression by exerting a controlled torque to drive the rotation frequency of the plasma [36, 37].

Positron compression can be achieved by the rotating wall technique in which a phase-shifted sine wave is applied to an azimuthally segmented electrode covering half of the electrode that constitutes the bottom of the potential well of the trap. In the present setup half of S3 in Fig. 2.2 is divided into

Phase	t [ms]	$f_{RW}$ [MHz]	Source	Inlet	S1	S2	S3	S4	Gate
Fill	900	4.6	6.8	2	-2.5	-11	-16.5	-11	20
Store	50	5.1	6.5	2	20	30	12	30	0
Dump	1	5.1	6.5	2	20	50	12	30	0

**Table 2.2:** Default trap parameters after optimisation of the timing output. All the potentials are listed in volts, and the values are as set by the LabVIEW control program. It should be noted that some mismatch between the set voltages and the actual voltages applied to the trap electrodes have been observed.

eight pieces and the same potential of equal phase is applied to opposite segments resulting in a rotating electric quadrupole field of frequency,  $f_{RW}$ . This field drives the rotation of the plasma and ensures compression compared to the initial state. However, since the rotating wall does work on the plasma, the plasma is effectively heating up as the compression is applied. Fortunately, the presence of the cooling gas provides an effective counteract of the energy increase. Angular momentum is either coupled directly to the trapped particles [38] or it is coupled to Trivelpiece-Gould states of the plasma [36] as the rotating electric field is applied. The compression ability has been shown to depend critically on the amplitude and frequency of the rotating wall, but it also depends on the central density of the positron cloud. Thus the rotating wall compression has been shown to work both in the single particle regime [39, 40] and in the strong drive regime [41, 42], where the latter is preferred because of the "no-slip" condition ( $f_{RW} = f_E$ ) being almost fulfilled. This implies that any central density can be set by the rotating wall frequency in the strong drive regime by using Eq. 2.5 up to the Brillouin density limit,  $n_B = \epsilon_0 B^2 / 2m_e$ , and in this way a density of  $0.1 n_B$  has been reached in a 450 G magnetic field [42]. The present setup operates in between the two extremes, where the plasma radius,  $R_p$ , is actually of the order of the Debye screening length, and corresponds to the setup in the original work by Greaves and Surko [34, 37, 38, 43]. Thus a similar behaviour of the positron trap is expected in the present work.

The positron trap is operated in a cycle that consists of three phases; fill, store and dump. The potential values of the trap electrodes in these three phases are shown in table 2.2 along with the duration of the phase,  $t$ , the rotating wall frequency and the source potential. All the potentials are given in volts, and the values were optimised at an earlier stage by M. D. Lund [44] and H. D. Thomsen [45] to achieve the maximum number of positrons in the plasma. The optimisation and characterisation was conducted with an older source, and some of the measurements were performed again after the new source was installed and the system was realigned following the laboratory refurbishment. The results of the more recent characterisation of the

continuous and bunched positron beam are discussed in the next section, where some attention has been paid to the temporal width of the extracted positron bunch. The potential values shown in the table 2.2 are those used most recently in the attempt to measure the multi photon ionisation, and a 1 Hz bunched beam is extracted from the trap.

The extraction of the beam from the trap furthermore requires an extraction beam tube solenoid to prevent the plasma from expanding rapidly. This beam tube can be set linearly by varying the field up to approximately 140G at a current of 3.0A and the beam of positrons can be used for a large variety of experiments. The extraction field may eventually also influence the trap performance since it could introduce inhomogeneities to the trap field that would decrease the trapping efficiency. On the other hand this might also work the other way around such that inhomogeneities are smoothed out and increase the trapping efficiency. This has however not been tested in our system. The beamline is operated automatically by software written in LabVIEW and provided by First Point Scientific, which has to some extent been modified to operate the beamline along with a laser. A full control of moderator growth, trap operation and timing of various hardware components is feasible using this program, and the parameters such as the laser delay are easily accessed for use in measurement sequences. The bunching and timing of the positrons will be further discussed in Subsecs. 2.2.3 and 2.2.4 of the present chapter.

## 2.2 Characterisation of the Aarhus positron beam line

The beamline parameters are measured destructively by inserting a phosphor screen (at  $-6\text{kV}$  and with a grounded grid in front) after the gate electrode. The optical photons emitted by the phosphor screen are subsequently accumulated on a CCD, and the number of counts in a given pixel is related to the positron intensity. Another possibility is to measure the annihilation  $\gamma$ -rays deposited in a scintillator (NaI(Tl), PbW<sub>4</sub> or a fast plastic scintillator) optically coupled to a photo-multiplier tube (PMT) to infer positron characteristics.

### 2.2.1 Continuous beam parameters

Several moderator growth schemes have been tested in an attempt to optimise the output of moderated positrons from the neon moderator. The cold head has a heater incorporated and (if things are working as intended) the moderator temperature can be adjusted with a precision of about 1% to any absolute value of down to 6K. The moderator efficiency is measured constantly by a  $\text{Ø}3'' \times 3''$  NaI(Tl) detector pointed at a right angle towards the beam axis and the annihilation  $\gamma$ -rays emitted from a closed valve between

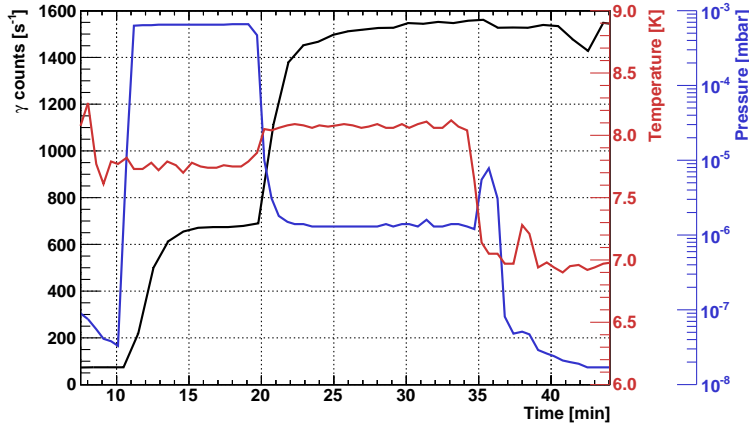


**Figure 2.5:** When a new moderator is grown, the old moderator is first evaporated (at  $t = 0$ ) by heating the cold head to  $\sim 25$  K. After cooling down again the  $\gamma$ -ray count rate (black) change as the temperature (red) and the neon pressure (blue) is set by the LabVIEW controlled moderator growth process described in the text.

the beam tube solenoid and the matching coil. A typical moderator growth is shown in Fig. 2.5 where the count rate at the NaI(Tl) detector is monitored as the high purity neon pressure is increased with the moderator held at a given temperature. The neon pressure is set by a mass flow controlled admission rate of 2.00 sccm to be  $6 \cdot 10^{-4}$  mbar for 9 min at 7.80 K with no pumping. As a consequence a layer of solid neon is established at the moderator cone and the  $\gamma$  count-rate starts to increase up to a stable value of about  $670 \text{ s}^{-1}$ . Neon admission is then stopped and the temperature is increased to 8.10 K for annealing in 15 min. The pressure falls to  $\sim 1 \cdot 10^{-6}$  mbar during the annealing phase and the ion pump is switched on again once the annealing has finished. The temperature is then set to the operation value of 6.80 K.

The low moderator pressure, stabilising at about  $5 \cdot 10^{-9}$  mbar at the operation temperature is a result of very little degassing from the moderator, and thus a very stable beam of positrons, decaying only by 3 – 4% pr. day can be achieved (with no gas load from the trap). This value is in agreement with the specifications given by FPSI [21]. The moderator is typically re-grown after about two weeks to maintain a high beam quality.

The rate of positrons in the continuous beam can be found from the  $\gamma$ -ray count rate measured by the large NaI(Tl) detector. The detector is positioned at a distance,  $d = 63$  cm from the beam axis to avoid the saturation present at smaller distances. Taking into account the absolute detection efficiency of 511 keV  $\gamma$ -rays,  $\epsilon = (0.487d^2 + 2.07d + 3.89)^{-1}$ , at the distance,  $d$  (in cm), the absorption of 511 keV photons in the vacuum chamber material and the fact that two photons are emitted pr. impinging positron, a positron count rate of

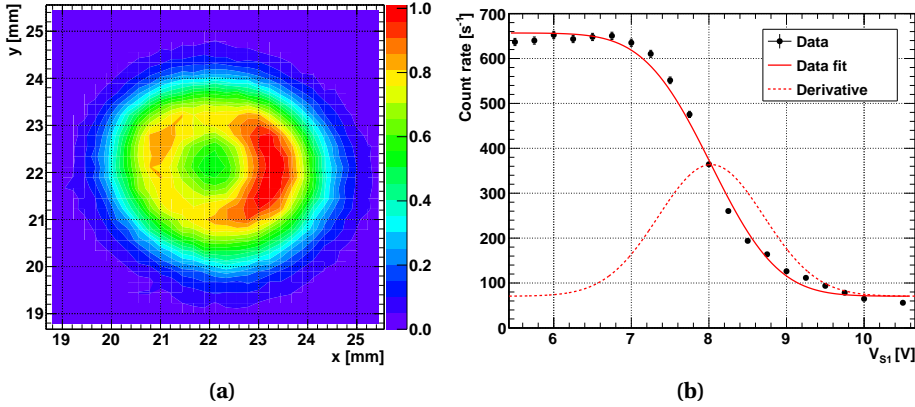


**Figure 2.6:** The transverse profile of the continuous beam is shown in (a), while (b) shows the data of a retarding field analysis of the continuous beam. The latter constitutes a measurement of the parallel energy and energy spread of the positron beam.

$4 \cdot 10^6 \text{ s}^{-1}$  is found. This rate was measured when the  $^{22}\text{Na}$  source had decayed to 24 mCi, and an efficiency of about 0.5% is achieved in good agreement with the expected value as stated by FPSI [21].

If a continuous beam of positrons is required as for instance in a Ps formation experiment utilising the  $3\gamma$  method to measure the Ps formation fraction (see Chapter 5 and [15]), the trap electrodes can be switched off or set to fall gradually and the trap solenoid field will guide the positrons to an interaction chamber placed in extension to the beamline. This was done while the phosphor screen was inserted after the trap and the hollow beam profile in Fig. 2.6a was measured (inside the trap solenoid field of 500G). From this measurement it is clear that the continuous beam is not completely symmetric and transverse beam diameters of  $D_{\text{cont},x} = 3.9 \text{ mm}$  and  $D_{\text{cont},y} = 3.3 \text{ mm}$  are found from a simple estimate of the FWHM based on the profile in Fig. 2.6a. The asymmetry is believed to originate from a small misalignment of the moderator electrode in the magnetic field from the Helmholtz configuration, since it cannot be removed by better alignment downstream in the beamline. Also, the coldhead is mounted onto a rotatable flange, which was aligned by eye to the beamline axis.

To measure the continuous beam parallel energy,  $E_{e^+,||}$ , the first stage of the trap was used for a retarding field analysis. The magnetic field of the trap was set to 120G to have the same field in the source and trap regions and avoid the conversion of transversal energy spread into parallel energy spread in the otherwise higher field in the trap. A smaller NaI(Tl) scintillator was then set up at the end of the trap, 23 cm from the beam axis, and the  $\gamma$ -ray count rate measured as a function of the potential of the (S1) electrode. The

source potential was held at a fixed value of 6.80V while the scan was performed and the result is shown in figure 2.6b. The number of positrons passing over the potential barrier set by S1 can be found from the integral of the Gaussian energy distribution from the value of the potential to infinity and a fit to the function

$$S_{\text{NaI}} = \frac{A}{2} \cdot \frac{2}{\sqrt{\pi}} \int_{\frac{V_{S1} - E_{e^+,||}}{\sqrt{2}\sigma_{||}}}^{\infty} \exp(-x^2) dx + N_{\text{bgd}} = \frac{A}{2} \cdot \text{Erfc}\left(\frac{V_{S1} - E_{e^+,||}}{\sqrt{2}\sigma_{||}}\right) + N_{\text{bgd}}, \quad (2.7)$$

give a mean parallel energy of  $E_{e^+} = 8.029(10)$  eV and a standard deviation of  $\sigma_{||} = 0.680(14)$  eV.  $N_{\text{bgd}}$  corresponds well with the usual background measured. The derivative of the fit gives the parallel energy distribution of the positrons and has also been drawn on Fig. 2.6b with a FWHM of the parallel positron energy that is  $\Delta E_{e^+,||} = 1.60(3)$  eV in good agreement with [21].

### 2.2.2 Trap performance

The continuous beam of positrons characterised in the previous subsection is now transported into the Surko trap at a rate of about  $4 \cdot 10^6 \text{ s}^{-1}$ . Inelastic collisions inside the confining potential ensures positron trapping and a bunched, brightness enhanced beam of positrons can be extracted from the trap. The trap performance is considered in the following.

The default duration of the phases in the most recent experiment is shown in table 2.2. The trap is open at the inlet electrode in the fill phase for positrons to accumulate in the trap, the rotating wall is applied in the store phase and the gate electrode is opened in the dump phase to extract the positrons into a low energy beam. The measurements conducted to characterise the trap performance generally used a 2.2Hz beam with a total cycle time,  $t_{\text{cycle}} = 0.451 \text{ s}^{-1}$  distributed between the phases such that the fill time is  $t_{\text{fill}} = 0.350 \text{ s}$ , the store time is  $t_{\text{store}} = 0.100 \text{ s}$ , while the duration of the dump phase is set to  $t_{\text{dump}} = 0.001 \text{ s}$ . After extraction, the positrons were impinging on a phosphor screen from which the emitted photons were accumulated onto a CCD and the transverse beam profile was measured (see Fig. 2.7a). The trapping efficiency can be found by comparing the total number of counts on the CCD for the continuous- and bunched beam (Figs. 2.6a and 2.7a, respectively) and a 5s exposure time, while taking into account the time in which the trap is open for positrons to be accumulated. The trapping efficiency is thus given by

$$\epsilon_{\text{trap}} \equiv \frac{N_{\text{bunch,CCD}} \cdot t_{\text{cycle}}}{N_{\text{cont,CCD}} \cdot t_{\text{fill}}} = 35\% . \quad (2.8)$$

where  $N_{\text{bunch,CCD}}$  and  $N_{\text{cont,CCD}}$  are the number of counts on the CCD during the 5s exposure time for the bunch- and continuous beam, respectively.

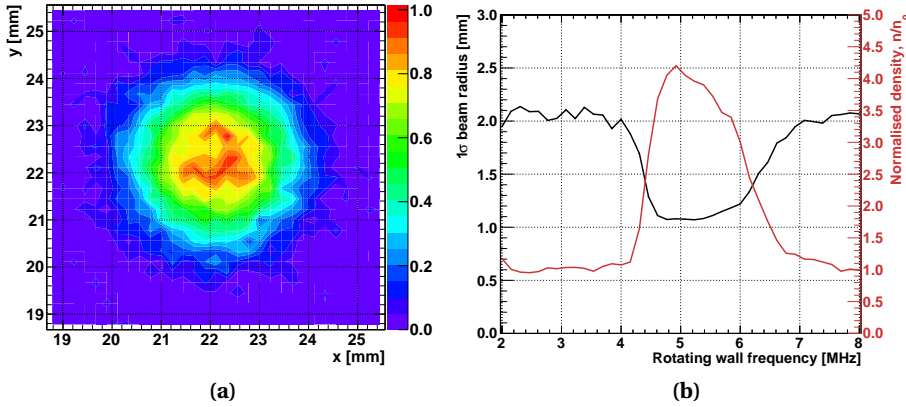


**Figure 2.7:** The bunched beam profile after the rotating wall compression is shown in (a). In (b) the frequency of the rotating wall has been optimised in terms of the transverse  $1\sigma$  radius of the beam and the central density normalised to the density when the rotating wall is off-resonance.

From the trapping efficiency it is easy to infer the typical number of positrons trapped within the fill time used in these measurement and we get  $N_{e^+} = 5 \cdot 10^5$  positrons pr. bunch. Having found the number of positrons in the plasma, the central density is found from Eq. 2.4 where the uncompressed positron radius,  $R_p = 2.07$  mm, (see Fig. 2.7b) is used along with the trap electrode length,  $L_p = 5$  cm, for the length of the positron plasma. The central density of the trapped positron plasma is,  $n_p = 4 \cdot 10^5 \text{ cm}^{-3}$ . Finally the Debye length of the plasma is found to be  $\lambda_D = 2 \text{ mm} \ll L_p$ . The plasma condition is easily fulfilled for the length of the plasma, but for the radius it is of the order of the Debye screening length, and the positron cloud can just barely be characterised as a plasma. This is different if the fill time is increased to accumulate more positrons. If the radius is not increased too much by the increased time for scattering and outward transport during the accumulation of positrons, then the plasma condition is better fulfilled, and our trap is operated in the same regime as in [34, 37, 38].

In Fig. 2.7b the rotating wall frequency is scanned to optimise the bunch compression in the store phase with the amplitude set to 1 V. It is seen that the radius of the beam is decreased down to 1.1 mm while the normalised central density can be increased by a factor of 4, thus enhancing the brightness of the beam. The optimal rotating wall frequency is  $f_{RW} = 5.1$  MHz as found from the centre of the dip in the radial scan, so this is the frequency at which the rotating wall is operated. When looking at the central density, however, it is more peaked, and a frequency of  $f_{RW} = 4.9$  MHz would be preferred from this scan. As mentioned earlier we have experienced some problems with the cold head and the moderator efficiency, which was from time to time

a factor of  $\sim 5$  below the expected value. This implies a smaller central density of positrons in the plasma since fewer positrons enter the trap per time and it was found that the rotating wall should be operated at a higher frequency to compress or even withstand the outward transport of positrons under these conditions. The rotating wall frequency was set to  $f_{\text{RW}} \sim 7$  MHz, but a quick optimisation is needed to confirm this number at future occasions<sup>2</sup>. It should be noted that the higher frequency is consistent with the higher frequency found for compression in the single particle regime [39, 40], which would also be expected because a smaller central density implies a transition to the single particle regime.

As shown the trap is operated in the plasma regime with a relatively broad range of rotating wall frequencies coupling to the plasma (compared to the sharp peaks in [36] or for the single particle regime [40]). Another essential parameter to investigate is the lifetime of the positrons in the trap, *i.e.* for how long time can the positrons be stored and what is the optimal fill time. A solution to the differential equation

$$\frac{dN_{e^+}}{dt_{\text{store}}} = -\frac{N_{e^+}}{\tau_{\text{trap}}} \quad (2.9)$$

yields the number of positrons in the trap,  $N_{e^+}(t_{\text{store}}) = \exp(-t_{\text{store}}/\tau_{\text{trap}})$ , after a given storage time,  $t_{\text{store}}$ , and is used to fit the data shown in Fig. 2.8a where the store time has been varied and the number of positrons in the trap is measured in terms of the peak-to-peak signal from  $\gamma$ -rays hitting the NaI(Tl) detector. The measured lifetime of positrons in the trap at these specific electrode settings and with a constant fill time,  $t_{\text{fill}} = 0.350$  s, is found to be  $\tau_{\text{trap}} = 1.5(3)$  s in good agreement with the value found by FPSI (1.8 s). Recently a lower  $N_2$  pressure has been used in the trap, which should yield a longer lifetime, however, this has not yet been measured.

For the continuous beam the positron parallel energy and energy spread was measured to characterise the moderator. Similarly, the parallel energy and energy spread of the positron plasma can be measured by varying the gate potential in a retarding field analysis, however, a slightly different approach has been used here. The S4 potential is held fixed at a given value (28.75 V, which was the previous default value) and the positrons are gradually pushed out of the trap by raising the S3 potential in the dump phase, keeping the rest of the potential constant. As the potential is raised close to the value of the S4 potential, the faster positrons start to exit the potential well and hit the phosphor screen to subsequent photon detection at the

---

<sup>2</sup>An operational detail is that the rotating wall phase shifter needs to be reset and initialised manually whenever the system has been shut down. This should work automatically in the LabVIEW program, but for some unknown reason it doesn't anymore.

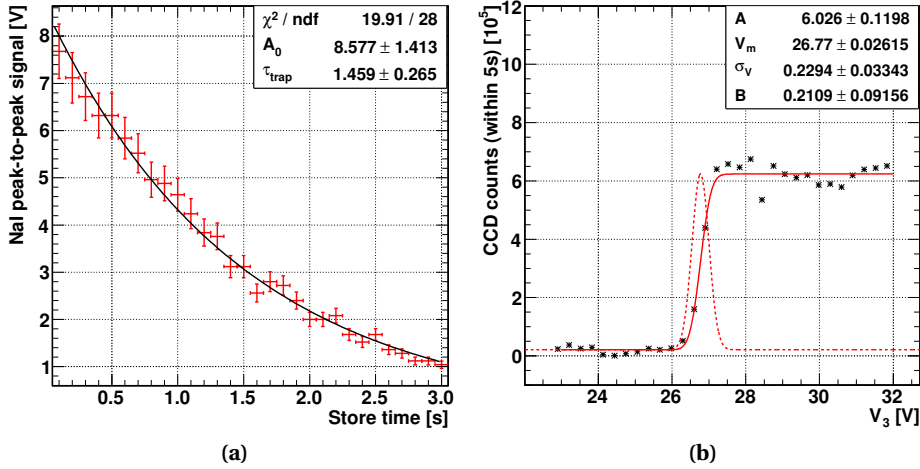


**Figure 2.8:** (a) The lifetime of the positrons in the trap is measured by varying the store time and measure the peak height in the NaI detector. In (b) the energy of the positron plasma is found from a retarding field analysis.

CCD. Assuming again a Gaussian energy profile the data in Fig. 2.8b can be fitted to a function similar to that of Eq. 2.7, but with the sign in the error function flipped, since it is the mean value that is now essentially being varied by raising the potential of S3. It is seen from the measurement that the positrons start to escape the trap earlier than expected, which could indicate the positrons have a larger mean energy in the trap than expected. This may be a consequence of insufficient counteract of the plasma heating by the rotating wall, but it may also be a result of a disagreement between the potential set by the LabVIEW program and the actual potential reaching the S4 electrode. The latter has in fact been observed although the effect has not been quantified. The measured parallel energy spread is found to be  $\sigma_{\parallel} = 0.23(3)$  eV giving a FWHM of  $\Delta E_{e^+, \parallel} = 0.54(8)$  eV for the bunched beam. Regarding the mean energy, H. D. Thomsen [45] and M. D. Lund [44] measured the mean energy to correspond quite well to the potential value of S3 in the dump phase when the positrons were extracted in the usual way, although the spread that they found was quite a lot larger than found for the measurement shown here in Fig. 2.8b. This increase in the energy spread can be explained by the effective debunching of the beam that occurred in the old default settings of the trap because the S3 potential was lowered during the dump phase. In the experiments conducted on this beam line the energy is set by biasing the target to a given potential typically up to 8 keV.

All the previous measurements discussed in this subsection were conducted using a slightly different trap potential than what is shown in table 2.2 and with a different buffer- and cooling gas load (0.3 sccm for  $N_2$  and 0.1 sccm

for SF<sub>6</sub>) because they were taken before the most recent optimisation of the trap to give a narrow temporal width of the extracted positrons. Before optimising the trap potentials the S3 electrode was lowered when dumping the positrons from 22V to 18V and the trapping potential was slightly asymmetric in the store phase. These settings were found in a coarse optimisation before my time in the laboratory and the maximum output of positrons was required. It is clear now that the lowered S3 potential during the dump phase has caused a debunching, and the temporal width of the initial time profile of the positrons was  $\Delta t_{\text{initial}} = 45(5)$  ns with the profile being measured by a fast plastic scintillator (with an intrinsic width of 4 ns) and shown in 2.11b. If the confining electrode, S3, was levelled in the store and dump phase, the temporal width was significantly improved to routinely reach  $\Delta t_{\text{optimised}} = 20$  ns, which is now the typical width of the positron pulse (the optimised profile shown in Fig. 2.11b is actually 25 ns wide and thus the temporal width was decreased even more after this measurement). This is however still a quite wide temporal width since the laser pulse to be used for multi photon ionisation of Ps has a FWHM of  $\lesssim 15$  ns and a further compression is required to increase the time overlap between the laser and the Ps cloud.

In addition to optimising the trapping potential in the three phases, the gas load was also optimised, and it was found that by decreasing the N<sub>2</sub> rate to 0.20 sccm, the peak height was increased slightly while the temporal width stayed constant. Also the SF<sub>6</sub> rate was decreased slightly to 0.05 sccm. The decrease in the gas load while maintaining the trapping efficiency is expected to increase the lifetime of the positrons in the trap, since the probability of annihilation in the third stage is decreased. The trap is expected to work under the same conditions with the new electrode settings and the lower gas load with the exception (apart from the temporal width) being a smaller energy spread because the debunching is now absent.

### 2.2.3 Positron time compression

In order to obtain a narrower temporal pulse width of the positrons it is necessary to implement a buncher into the beamline system. There are a couple of options for time compression of positrons described in [46]. One way of bunching the positrons in time is to quickly apply a parabolic potential along the beam axis to a set of bunching electrodes [47], while the positrons are traversing the electrodes. This will create a time focus and a gain in the flux of positrons at the focus  $\sim V_m/\Delta E_{e^+}$ , where  $V_m$  is the maximum acceleration voltage applied to the positrons and  $\Delta E_{e^+}$  is the initial energy spread. This method requires a long set of electrodes and simultaneous application of a potential to each of the electrodes and it may be cumbersome to get to work. Some trap based beamlines apply this potential directly to the trap

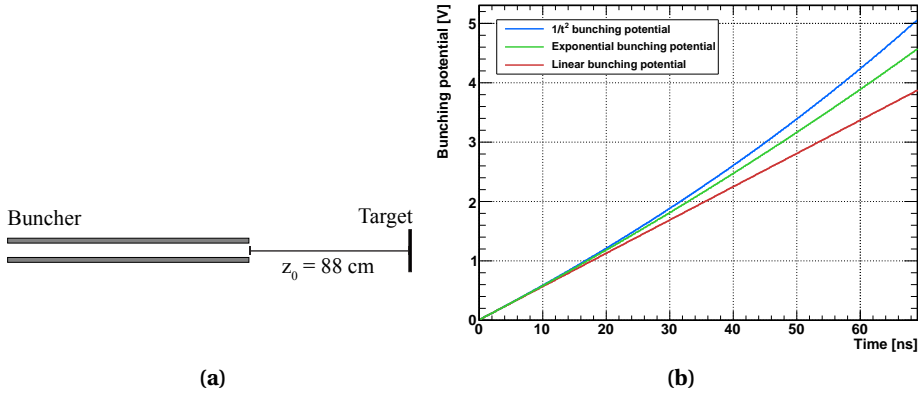


**Figure 2.9:** The buncher sits inside the extraction solenoid and the distance to the time focus at the target is  $z_0 = 88$  cm as shown in (a). In (b) the three bunching potentials are shown for an initial positron energy of 12 eV.

electrodes upon extraction of the positrons, but since the electrode density in the present system is quite low compared to other systems it is not possible to apply a smooth potential along the beam axis when dumping the positrons from the trap. Furthermore this would require a new way of applying the potentials to the trap electrodes since the present method is not fast enough (though the potentials are applied simultaneously to the electrodes).

The solution here is instead to install a simple bunching electrode inside the extraction solenoid (see Fig. 2.1) and apply a timed potential to the electrode such that the positrons will feel an increased acceleration as they pass the potential drop at the exit of the electrode. It is essential to design an electrode that is long enough for all the positrons to fit inside before the potential is applied. The electrode used here is shown in Fig. 2.9a. It is a 25 cm long pipe of aluminium isolated electrically from the vacuum chamber and with a short cable attached to an SHV feed-through. In Fig. 2.9a the distance  $z_0 = 88$  cm is the distance to the target where a time focus is required. The optimal potential to apply to the electrode is parabolic in time

$$V_{\text{Par}}(t) = V_0 \left( \frac{t_0^2}{(t - t_0)^2} - 1 \right), \quad (2.10)$$

where  $V_0$  is the potential at the bottom of the trap assuming the positrons have an initial mean energy of  $eV_0$  and  $t_0 = z_0 / \sqrt{(2e/m_e V_0)}$  is the mean time it takes for the positrons to travel to the target, *i.e.* the time at which the time focus is expected. If the time  $t_0$  is long compared with  $t$  a first order Taylor expansion around  $t = 0$  gives a linear approximation of the potential

$$V_{\text{Lin}}(t) = 2V_0 t / t_0, \quad (2.11)$$

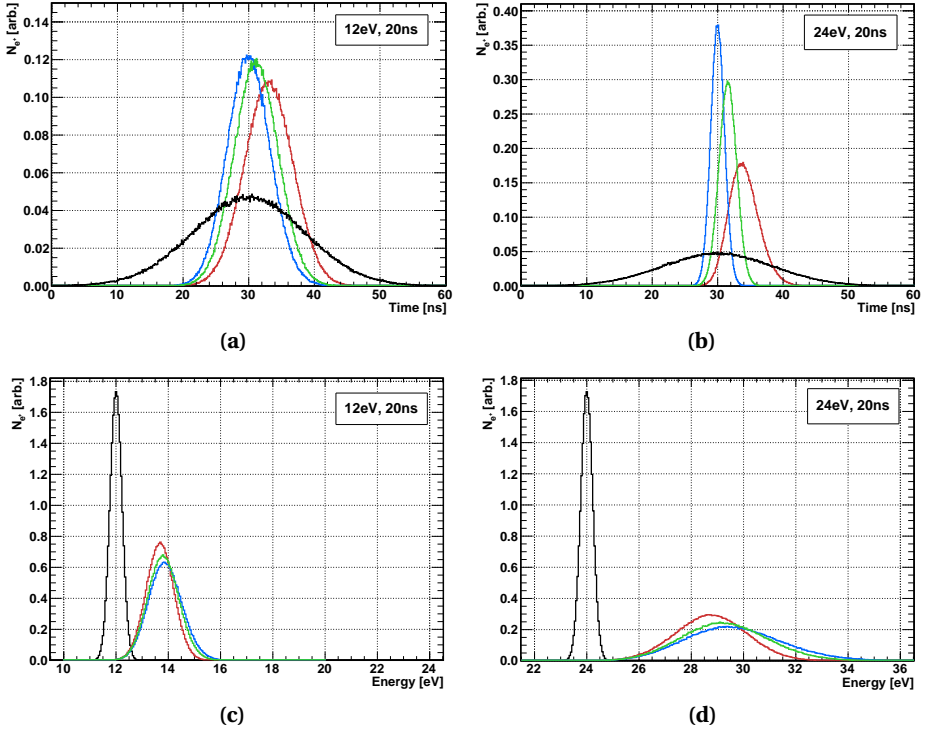


**Figure 2.10:** Positron bunching simulation with two initial positron energies, 12 eV in (a) and (c) and 24 eV in (b) and (d). Both time and energy profiles are simulated. The black curve is the un-bunched profile, and the other colours are as given in Fig. 2.9b.

which is seen in Fig. 2.9b to be in fair agreement with the parabolic potential of Eq. 2.10 for times of the order of the temporal width of the positron pulse [48]. In the figure an exponential approximation,  $V_{\text{Exp}}(t) = V_0 (\exp(2t/t_0) - 1)$ , is also shown. This function is seen to be a better approximation than the linear and applies also for shorter focusing times,  $t_0$ .

Before deciding on the parameters of the bunching potential and distance to the focus a Monte Carlo simulation of the bunching capabilities of the three potentials in Fig. 2.9b were made. The results of the simulation are shown in Fig. 2.10 where both the time and energy profiles are shown for a 12 eV and a 24 eV initial mean energy. For realistic parameters the simulation is based on  $5 \cdot 10^5$  positrons that are randomly assigned an energy and a time based on the initial distributions. Both distributions are assumed to be Gaussians with FWHM's as found from measurements in the previous section, namely 0.54 eV and 20 ns for the energy and time distribution, respectively. The initial time profile is adjusted - as in the real setup - such that the potential begins to increase when the first positrons exit the buncher electrode.

For each of the three bunching potentials the acceleration of each positron is calculated based on the time of arrival at the buncher exit and a new energy is calculated which is used to find the new time of arrival at the target ( $z_0$ ).

The simulations clearly shows that the approximate potentials are indeed useful at low energy, but as the mean positron energy is doubled the time,  $t_0$ , becomes smaller and the parabolic potential does an increasingly better job compared to the approximations. It is also seen that the mean energies for the linear and exponential potentials are slightly smaller and more peaked than for the parabolic potential which is why the positrons will be focused at a slightly later time for the approximate potentials. Even though the approximations are not good at higher positron energies the bunching is still seen to become more efficient as the positron mean energy gets higher for these potentials. The temporal width (FWHM) found from the simulation for a mean energy of 12 eV and using the linear acceleration potential is  $\Delta_{\text{sim}} = 8.7$  ns, which is well below the requirement for the multi photon ionisation experiment.

To make the parabolic potential that is needed for optimal time compression it is necessary to use a very fast arbitrary waveform generator. Since these are quite expensive and the approximate linear potential works almost as well at 12 eV positron energy we decided to use the sine approximation of a linear potential<sup>3</sup> which is also used in [48], but cut off by a diode limiter as the voltage goes up to the maximum voltage set by the power supply. The bunching was experimentally confirmed by measuring the pulse of  $\gamma$ -ray photon from the annihilation of many positrons at a time. Averaging over 16 pulses on the oscilloscope, the FWHM was measured for various buncher delay times (controlled by the setup described in subsection 2.2.4) to optimise the temporal width and the peak height or instantaneous flux of positrons at the target position. The optimisation is shown in Fig. 2.11a and the optimal delay is found to be 1242 ns. The buncher delay value is set with reference to the time at which the trap potentials are set. This delay is controlled by a LabVIEW program, and all hardware components including the trap potentials can be set relative to each other as described in the next subsection. The time profile of the bunched positron beam at the optimal delay is compared to the initial profile from the trap and the profile after the trap has been optimised to yield a bunch of minimum temporal width (see Fig. 2.11b). The temporal width of the time compressed profile is  $\Delta_{\text{meas}} = 8.6(5)$  ns, which has been obtained also by optimising the slope of the linear potential. Thus a similar optimisation is performed for the simulation to give an optimal slope of 1.4 times the slope in Eq. 2.11 and a minimum temporal width of 7.5 ns, which

---

<sup>3</sup>Thanks to Erik Søndergaard for making the electronics to provide the time triggered linear potential.

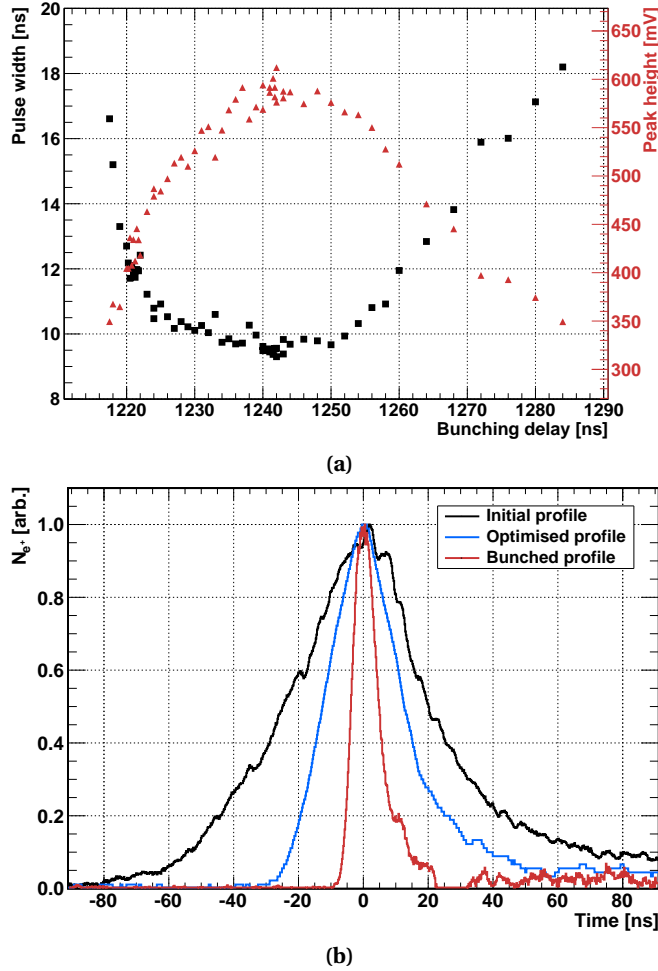


**Figure 2.11:** The delay of the bunching potential has been optimised in a measurement as shown in (a) to give the smallest pulse width and the largest peak value. The time compression is illustrated in (b), where the peak normalised time profiles as measured for the initial trap settings, the optimised trap settings and the bunched beam are shown.

is comparable to the bunched width obtained using the parabolic potential. To compare the simulation with the measurement, the simulated time profile should be convolved with the Gaussian response function of the detector system ( $\sim 4$  ns), which has been measured by triggering on the signal when the continuous beam is on. This gives a final simulated width of 8.5 ns in perfect agreement with the measurement.

It is also noted that the bunched width shown in Fig. 2.11b is slightly smaller than the one found in the buncher optimisation. The reason for this

is simply that the optimisation used a simple average from the scope and the time profile is broadened by time jitter ( $\sim 1$  ns). This is not the case for the profile shown in Fig. 2.11b since a constant fraction discriminator (CFD) trigger has been used in the analysis to adjust for the time jitter.

#### 2.2.4 Timing the positrons

It is crucial for the positron trap to work properly that the potential values can be set simultaneously on all the electrodes. The timing of trap voltages in the original FPSI setup was controlled by the eight digital to analog converters (DAC's) in the Kontron PCI-A0B8/12 (16/12) card implemented in the beam-line control PC. The values set by the LabVIEW control program are sent to a buffer on each DAC and an update signal ensures the simultaneous application of the voltages to the trap electrodes. The positron detection was triggered using the negative slope of S4 in a setup which proved to be relatively stable from shot to shot. However, the time jitter between the trap phases is horrible ( $\sim 1$  ms) since this time is set purely by software, whereas the timing between voltages at the separate stages within a phase is controlled by hardware. The problem when employing a buncher and a laser into the system is the lack of the possibility to externally trigger the positron extraction from the trap. This is important since then the trap could be delayed with respect to either of these components if necessary and not just the other way around. One possible solution is to control all the timing using a field programmable gate array (FPGA), however, this takes a lot of effort in re-programming the trap control which is already working well and one would have to buy a proper FPGA first. Fortunately Per B. Christensen (electrical engineer at the department) came up with an immaculate solution to the problem.

The wire for the update in the Kontron PCI-A0B8/12 (16/12) card was cut and the update signal extracted through a BNC panel at the back of the PC, labelled as TrigOut in Fig. 2.12a. The update signal serves as a pre-trigger, which is sent to a Stanford Research Systems (SRS) digital delay/pulse generator (DG535). In the DG535 the update signal triggers the output of four (TTL) signals, A, B, C and D that are delayed by a predefined time set by a LabVIEW program. These signals can now be used to trigger any hardware, including the trap for a delayed positron extraction. However, there is an update signal every time the phase is changed in the trap and we only require a trigger in the dump phase for the buncher. Likewise, the laser must operate at 10Hz, which is not the case if it receives a trigger every time the phase of the trap is changed. To solve this problem Per B. Christensen designed the print board shown in Fig. 2.12b. It uses the first four bits of the Digital I/O Port A in the Kontron PCI-A0B8/12 (16/12) card as input to four AND gates which are used to decide whether the trigger should pass on to the output

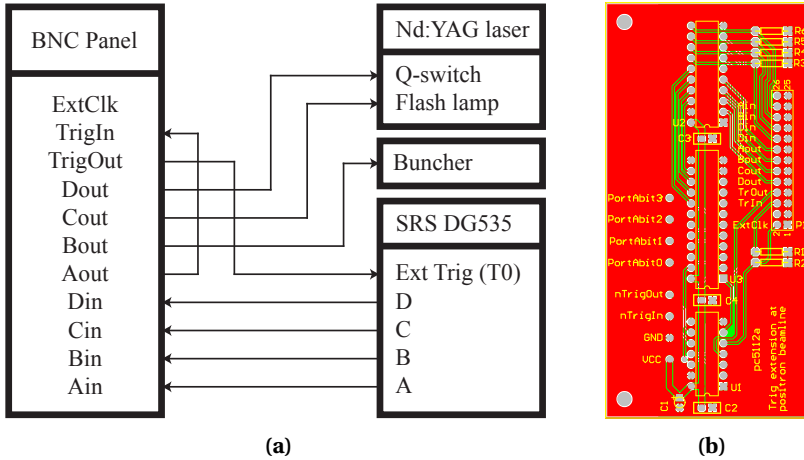


**Figure 2.12:** The timing system is illustrated in (a), where TrigOut serves as a pre-trigger for all the hardware timing. In (b) the print board for the trigger selection is shown.

BNC's at the back of the control PC of not. The bits (Bit 0-3) are set in a LabVIEW program to be 0 or 1 for no trigger or trigger output to a given hardware device in each phase. In Fig. 2.12a it is seen that Aout goes to TrigIn and on to the trap as a delayed update signal. An output of this trigger should always be given for the trap to operate correctly<sup>4</sup>, i.e. the first bit of Port A should be set to 1 in all phases. The signal B, C and D from the DG535 goes to each of the input BNC's, Ain, Bin and Cin, through the AND gate and, if gated, to the output BNC's where the signal is sent to the devices. B triggers the buncher, C triggers the laser flash lamp and D triggers the Q-switch of the laser.

The buncher delay was optimised in the previous subsection to be 1242 ns as given by Fig. 2.11a, but the value changes with the maximum voltage applied to the buncher by the power supply because an increased maximum voltage increases the slope of the potential and it changes the onset of the voltage increase to be slightly earlier. This buncher delay should thus be checked from time to time and more recently 1212 ns were found to be optimal.

It is important when the delay values of the DG535 are set to be careful when choosing the reference points for the delays. The absolute accuracy with which the delay can be decreases with an increasing delay. Thus when a high timing precision is required the reference points should be chosen such that the critical delays are the smallest.

<sup>4</sup>The wiring on the print board is such that the update signal of TrigOut will go directly to TrigIn if all bits of Port A are set to 0 in all phases, thus recovering the original setup.

---

# Meso-structured silica films for positronium production

Positronium is formed in various samples upon positron implantation. In recent years, the research has focused on Ps formation in various types of structured silica (porous, grained, aerogel and variations thereof). Nanostructured materials are interesting since a high yield of low energy Ps can be obtained from these samples due to collisional cooling, which is further investigated in Chapters 4 to 6. In this chapter the targets used in this work to form Ps in both reflection and transmission are presented, as is the innovative development of future targets utilising self-suspended graphene for film support instead of amorphous carbon. The targets were originally developed to facilitate cold transmission-formed Ps for the setup proposed for multi photon ionisation of Ps [49]. However, as stressed in [16], transmission Ps formation can improve the setup in a wide range of experiments and may even be essential for obtaining a more efficient Ps cooling below room temperature.

## 3.1 Glancing angle deposition of $\text{SiO}_2$

The samples used for Ps production throughout the present work are produced using the glancing angle deposition (GLAD) technique [50], which allows for three-dimensional engineering on a nanometer scale. Many different three-dimensional structures can be constructed using this technique and the morphology of thin films is directly controllable by the variation of a limited number of macroscopic parameters [51]. Usually, the films are grown onto a Si(100) wafer or similar to study the structures in detail using a scan-

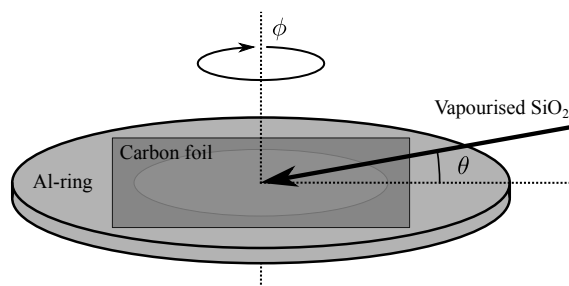


**Figure 3.1:** The meso-structured silica films are grown on a rotating carbon foil at a glancing angle of incidence,  $\theta$ . The carbon foil is held by an Al-ring [15].

ning electron micrograph (SEM)<sup>5</sup> for instance. This is also done in this work to verify the expected nanostructure, but to facilitate the formation of Ps in transmission through the film a 20 nm carbon foil has also been used to support the thin meso-structured silica films. The carbon foil is attached to an aluminium ring with a central hole diameter of  $\text{\O}8\text{mm}$  and an outer diameter of  $\text{\O}12\text{mm}$  prior to deposition (see figure 3.1). Vaporised  $\text{SiO}_2$  (silica) is then continuously deposited onto the surface at a glancing angle of incidence with respect to the carbon surface,  $\theta$  ( $3^\circ$  to  $17^\circ$  in this work). The deposition occurs at a constant rate,  $D_{\text{rate}}$ , for a duration,  $d\tau$ , and the energy of the  $\text{SiO}_2$  is close to zero. Initially, for small duration times,  $d\tau$ , the silica vapour will stick to the surface and diffuse to the potential minima occurring near defects at the substrate surface. As more material is deposited onto the surface, nucleation causes an increasing amount of silica to be collected near defects. Since the angle of incidence of the vapour flux is small, the elevation seen in Fig. 3.2a is shading an area at which no material will be deposited, and an inclined columnar structure starts to grow from the surface as shown in Fig. 3.2b. The inclination angle,  $\beta$  can be found from Tait's rule as the simple expression [52]

$$\beta = \alpha - \text{asin}\left(\frac{1 - \cos(\alpha)}{2}\right), \quad (3.1)$$

where  $\alpha = 90^\circ - \theta$  is the deposition angle given with respect to normal incidence. This equation facilitates a direct control of the inclining angle of the pillars, however, the control so far is only two-dimensional. Furthermore, the porosity increases while the average density decreases for increasing  $\alpha$  (since the shadow becomes longer), and Eq. 3.1 sets a limitation to the control since high porosity for low inclination angles,  $\beta$ , cannot be reached with this setup [51]. Therefore a rotational degree of freedom is introduced, such that the film can also be rotated at a rotation frequency,  $\phi$ , which can be con-

<sup>5</sup>It was Folmer Lyckegaard who made all the technical work with respect to the silica samples, *i.e.* he grew all the films, and he took all the SEM images presented in this chapter.

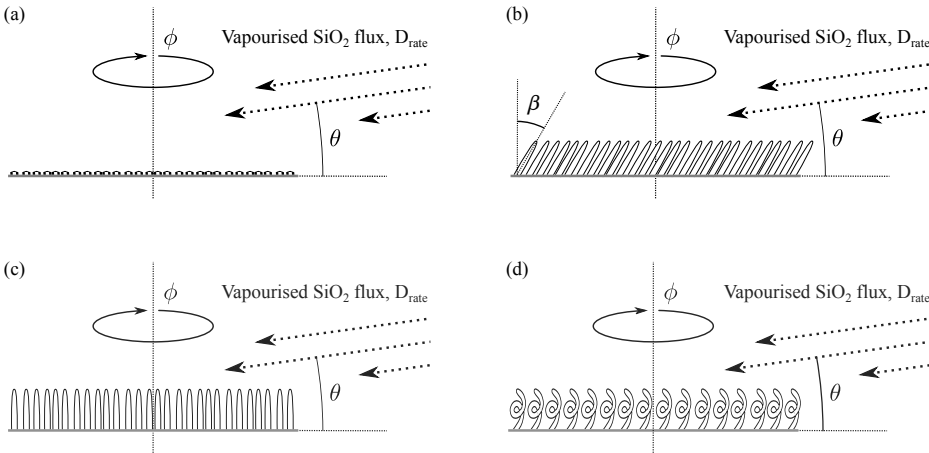


**Figure 3.2:** The meso-structured silica films starts to grow from discrete spots (a). As shadowing effects start to set in, pillars will evolve that are leaning towards the deposition source. If the sample is rotated simultaneously to the deposition, then the pillars become vertical is the rotation is rapid (c). If the rotation is slow, the spirals will occur (d).

trolled with respect to the deposition rate,  $D_{\text{rate}}$  to enhance the sculpturing capabilities and introduce a three-dimensional control of the structure. For the thin films used in these studies, the rotation frequency was typically set to 6rpm, while the deposition rate was  $D_{\text{rate}} = 1 \text{ nm/s}$ , measured at normal incidence (controlled by a Quartz Crystal Monitor positioned normal to the  $\text{SiO}_2$  flux direction). At such a high rotation frequency, the vapour flux averaged over time is the same from all azimuthal angles, and pillars of inclination angle  $\beta = 0$  are formed as shown in Fig. 3.2c. Finally, the rotational frequency can also be set to a low value compared to the incident deposition rate. This results in a significant amount of material being deposited before the angle is changed, and because the columns grow up against the flux direction, a helical structure is implied (which has been shown to be optically active since the plane of polarisation of light can be changed [53]). The latter growth method was first employed for the Ps formation targets, and a few results using these samples are shown in Chapter 5. However, since the thin films consisting of vertical columns were more robust and reproducible when growing thicker samples (where the deposition orientation is otherwise easily lost), these samples were used for the latest work here.

The structured samples used to form Ps are generally characterised by their porosity, density, and morphology, *i.e.* the geometrical shape and size of pores, grains, and pillars. The porosity of a given material is defined as the

ratio between the void volume,  $V_{\text{void}}$ , and the total volume of the film,  $V_{\text{film}}$ ,

$$\mathcal{P} = \frac{V_{\text{void}}}{V_{\text{film}}} = \frac{A_{\text{void}}}{A_{\text{mater}} + A_{\text{void}}}, \quad (3.2)$$

where the  $A_i$ 's are areas of void and material when viewed from the top. The last equality holds only for films where the pillar size is constant throughout the sample, which is not the case in general, but is assumed in the present analysis. The initial pillar separation,  $s$  (edge to edge) can be found from the grain height,  $h$  at which the shadowing effects become significant compared to the surface diffusion,  $s = h \tan(\alpha)$  (this occurs for thicknesses  $\lesssim 1$  nm [54]). The porosity has been shown to take the form

$$\mathcal{P} = \frac{\alpha \tan(\alpha)}{c + \alpha \tan(\alpha)}, \quad c = \frac{\pi V_{\text{mater}}}{2 A_{\text{vert,cs}} h}, \quad (3.3)$$

where  $A_{\text{vert,cs}}$  is the vertical cross sectional area of the grain found when shadowing effects set in, and  $c = 3.17$  has been found empirically for  $\text{SiO}_2$  by fitting data for the porosity as a function of the angle,  $\alpha$  [55]. The density can now be found directly from the porosity or vice versa by implying the relation,  $\rho_f / \rho_{\text{mater}} = 1 - \mathcal{P}$ , where  $\rho_f$  and  $\rho_{\text{mater}}$  are the densities of the film and the non-porous materials.

The porosity varies not only with the angle of deposition, but also with the thickness of the film. This is due to an increase in the column diameter as the height of the columns increases, resulting in a larger shadowing area, and extinction of neighbouring columns. Therefore, the average spacing between columns also increases with the target thickness [56], and so does the porosity while the density of the film decreases. To determine the thickness in the first place, the normal thickness,  $\Delta t_{\perp} = D_{\text{rate}} d\tau$  (thickness deposited at normal incidence) should be correlated with the actual thickness of the film. This was done in [57], and the film thickness-density product is given by

$$\rho_f H_f = \frac{S_{\theta,f}}{S_{\theta,s}} \rho_{\text{mater}} \Delta t_{\perp} \cos(\alpha), \quad (3.4)$$

where  $\rho_f$  is the effective density of the film,  $H_f$  is the film thickness,  $S_{\theta,f}$  and  $S_{\theta=0,s}$  are the sticking coefficients for the film and the sensor, respectively, and  $\rho_{\text{mater}} = 2.65 \text{ g/cm}^3$  is the bulk density of the deposited material. The ratio between the sticking coefficients is 1 since the energy of the deposited material is close to 0 eV in the GLAD setup used here and the molecules easily stick to the substrate surface even at a small glancing angle. If Eq. 3.4 is used, then either the film thickness or density can be determined from a measurement of the opposite quantity for a given normal thickness.

The relation between the density and thickness holds quite well for films with various morphologies [57], and the same average density and porosity

can be obtained for films grown at the same angle using the same material. However, the thickness of the film has to be changed accordingly. Since the films thickness must increase with the normal thickness it is also clear from Eq. 3.4 that the density decreases (porosity increases) if the film thickness increases. The porosity increase can be attributed to an increase in the column diameter,  $D$ , which results in an increase of the shadow length and thus an increase in the spacing between pillars. Both the column width and spacing follow a power law dependency on the thickness of the film  $D \sim (H_f)^p$  [56, 58]. The exponent,  $p$ , changes as the deposition angle changes, and values between 0.3 and 0.6 have been found with  $p$  decreasing for increasing angle,  $\alpha$ . For  $\alpha = 83^\circ$  the exponent  $p = 0.50$  was found, but this may change due to the specific environment in the used setup and misalignments in the angle might occur [58]. The spacing between the pillars is expected to follow a power law with approximately the same exponent [56].

For films with vertical pillars grown using GLAD which are mostly used in the present work, the morphology of the film can be described by randomly distributed vertical pillars that increase in diameter with the distance from the substrate. The packing density decreases with the tilt angle,  $\alpha$ , with respect to normal incidence, and above  $\sim 83^\circ$  column extinction becomes significant as the film thickness is increased. Thus the spacing between columns also increases with the distance from the substrate.

The growth parameters can be varied throughout the total growth time to form multilayered structures where each layer is grown at for instance different glancing angle,  $\theta$ , for a deposition duration,  $d\tau_\theta$ . The density and porosity of each layer can then be inferred from a measurement (*e.g.* using a cross sectional Scanning Electron Micrograph (SEM)) of the thickness of the given layer using Eq. 3.4. This is particularly useful when determining effective densities for the positron implantation profiles as described in Chapter 4. Another advantage of GLAD is applicability to a large variety of materials such as Si, Cu, Ti [57], ITO [55] and Ge, but with  $\text{SiO}_2$  being a particularly good choice due to its low degree of diffusion at the surface, which makes sticking more efficient.

To achieve a low Ps energy by collisional cooling it is desirable to cool down the sample. This can cause difficulties for silica samples because they are in general hydrophilic and thus attract water molecules within the vacuum system. This will either block the pores or make the inner surface inappropriate for collisional cooling since the surface pick-off annihilation is increased. This problem was recently solved in [59] by the use of swollen MCM-41 samples to form positronium, where no temperature dependency on the Ps emission probability was observed. Similar properties are expected to be reachable for the meso-structured silica samples since the inner surface of the structured films has been shown to become superhydrophobic upon sur-

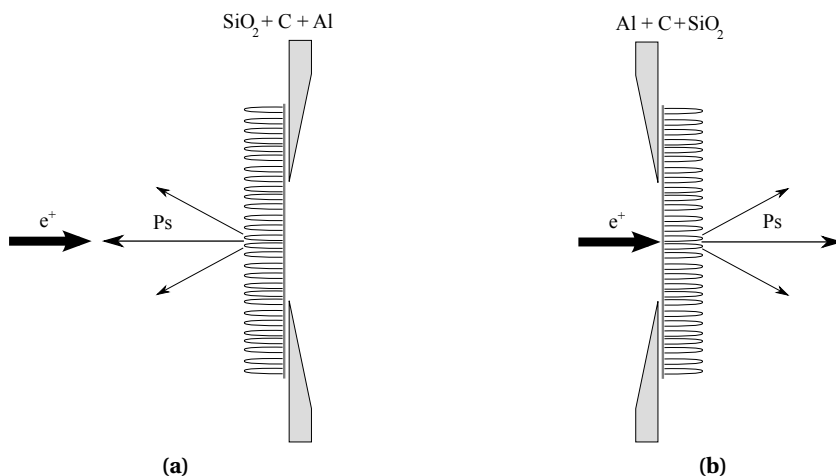


**Figure 3.3:** (a) The reflection geometry in which the positrons hit the silica thin films directly. (b) The transmission geometry in which the positrons hit the carbon foil first and penetrate through to the meso-structured silica from transmission Ps formation.

face treatment by siloxane based chemicals that are commercially available [60].

Because the film thicknesses extend up to about  $1\ \mu\text{m}$  with a typical density of about  $0.4\ \text{g}/\text{cm}^3$ , the films can function effectively as infinite Ps formation targets for low positron implantation energies, *i.e.* up to a certain energy the positron will not register the transmission surface of the film. Thus the samples are used in two geometries throughout this work as shown in Fig. 3.3, namely reflection and transmission geometries. In the reflection geometry, the positrons are impinging upon the silica thin film directly, whereas in the transmission geometry, the positrons have to penetrate the carbon foil first in order to enter the meso-structured silica film for Ps formation in transmission.

### 3.2 Characterisation of the structured films

The thin films grown using the GLAD technique in this work are characterised by SEM and TEM (transmission electron microscopy)<sup>6</sup>. An equivalent film is grown on a Si(100) wafer simultaneously to the film grown on the carbon foil. The silicon wafers are much less fragile than the carbon foils, and they are perfectly suitable for imaging with SEM. The samples are inserted into a DualBeam Versa 3D SEM [61] in which a focused electron beam is scanned across the surface to image the structure by collection of backscattered elec-

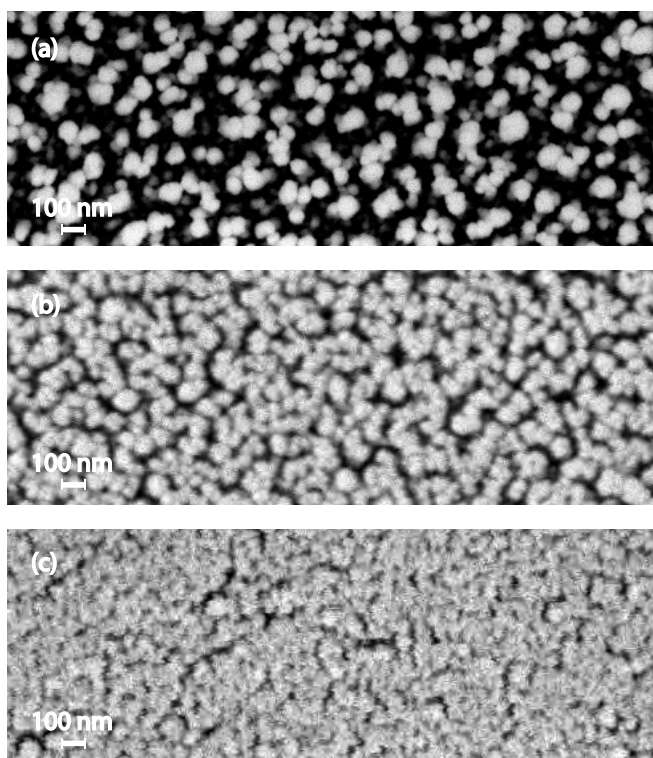


**Figure 3.4:** The meso-structured silica films imaged by SEM from a top view for three different samples. (a) Shows a sample with  $\Delta t_{\perp} = 1000$  nm,  $\theta = 7^{\circ}$  and  $\phi = 6.0$  rpm. For the sample in (b)  $\Delta t_{\perp} = 1150$  nm,  $\theta = 12^{\circ}$  and  $\phi = 6.0$  rpm and for the sample in (c)  $\Delta t_{\perp} = 840$  nm,  $\theta = 17^{\circ}$  and  $\phi = 6.0$  rpm.

trons, secondary electrons and photons emitted from specific positions in the sample. The SEM also incorporates a Focused Ion Beam (FIB) of  $\text{Ga}^{+}$  ions that can be used also to image the surface, but because it is rather destructive it is better suited to cut out a cross sectional piece of the surface, which is then imaged by TEM for a precise thickness determination.

The sample used in [16] has a normal thickness of  $\Delta t_{\perp} = 1000$  nm and is grown at a glancing angle of  $\theta = 7^{\circ}$  with the sample rotating at  $\phi = 6.0$  rpm. A SEM image of this sample is shown in Fig. 3.4a from a top-view. Since this sample has been studied in most detail in terms of Ps production it is used in the following as a reference to other meso-structured silica films.

The SEM image in Fig. 3.4a shows a surface consisting of bright columns standing at right angles with dark spaces between the pillars. A number of faint spots are also seen between the brightest columns. This shows that column extinction because of a larger shadow from an increased column diameter has set in at a normal thickness of 1000 nm. A quantitative analysis of

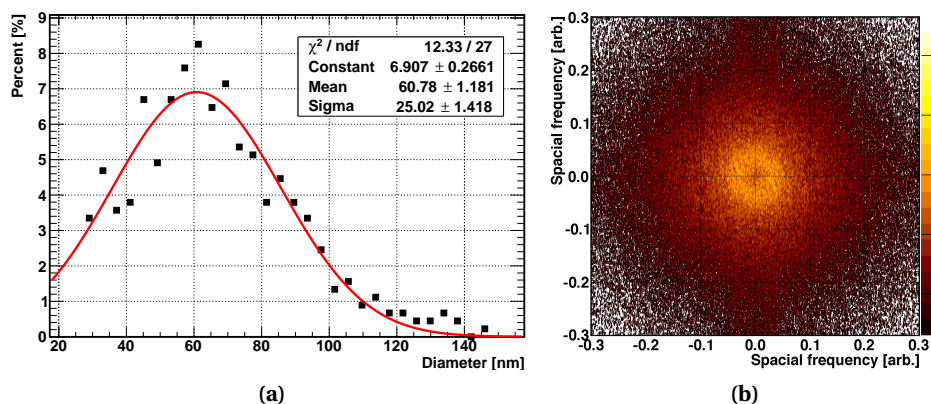
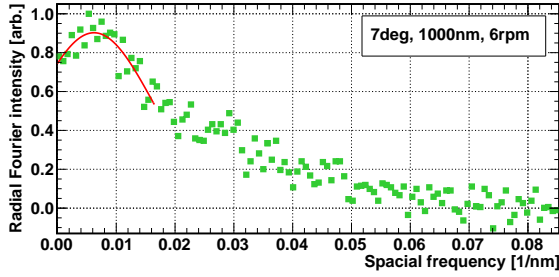


**Figure 3.5:** The column diameter distribution is shown in (a) for the film of normal thickness 1000 nm. (b) Shows a FFT of the SEM image in Fig. 3.4a, which is used to estimate the columns spacing. See the text.

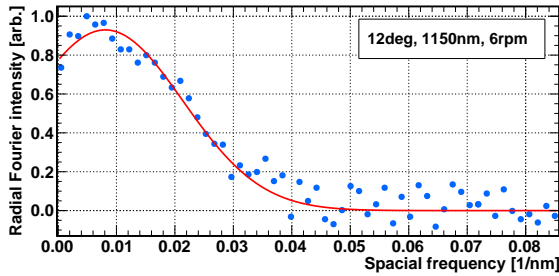
the SEM images can be conducted using specialised image processing software such as SPIP (Scanning Probe Image Processor) [62] or ImageJ [63]. The mean porosity is estimated at a depth of half the thickness from an estimate of dark and bright areas of the SEM image and the application of Eq. 3.2 to be  $\mathcal{P} \sim 85\%$  in good agreement with Ref. [57]. The average density can now be found from  $\rho_f = (1 - \mathcal{P})\rho_{\text{mater}} \sim 0.4 \text{ g/cm}^3$ .

The columns and pores can be identified by a particle and pore analysis using SPIP in order to determine the areas of material and voids. This determination was done for the  $\Delta t_{\perp} = 1000 \text{ nm}$  sample only, and the distribution of column diameters was also obtained as shown in Fig. 3.5a. The diameter distribution has been fitted to a Gaussian function, and a mean column diameter of  $\sim 60 \text{ nm}$  is found with a standard deviation of the distribution of  $\sim 25 \text{ nm}$ . A similar analysis was performed in [56, 58] with results being approximately half of the value obtained here. Eventually, this discrepancy is expected, since the thickness is a factor of four larger in this case (as will be argued below the real film thickness of the film with a normal thickness of 1000 nm is about 800 nm), and the column diameter was predicted in [58] to increase as the square root of the film thickness for films deposited at a glancing angle of  $\theta = 7^\circ$ . However, compared to the  $D \sim (H_f)^P$  dependency mentioned above there must be a factor of two, which has not been mentioned in [56] or [58], but is needed to obtain the results in the references as well as in the measurement presented here.

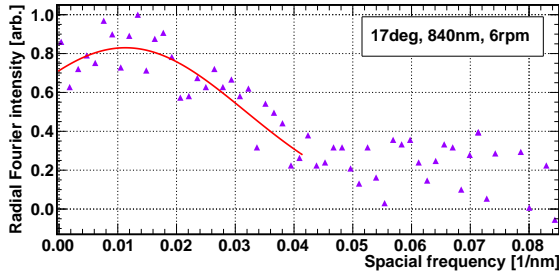
The column spacing can also be obtained from a careful analysis of the SEM images in Fig. 3.4, by performing a 2D Fast Fourier Transform (FFT) of each image. The results of such a FFT is shown in 3.5b for the target with a normal thickness of 1000 nm. The diffuse ring is evidence of a random distri-



(a)



(b)



(c)

**Figure 3.6:** Radial profiles of the FFT's of the SEM images in Fig. 3.4. The Gaussian fits are used to extract the typical spacing between the pillars in the meso-structured samples.

bution of pillars and no ordering is seen. The characteristic column spacing can be found from the typical radius of the ring. To determine the typical radius a radial profile of the FFT is plotted in Fig. 3.6a for the  $\Delta t_{\perp} = 1000$  nm sample. The radial distribution of spacial frequencies has been fitted to a Gaussian function to obtain the typical spacial frequency, which is then converted into a typical column spacing by inversion. A similar analysis was performed for the other two SEM images in Fig. 3.4, which represents the structure of samples with different glancing angles ( $12^{\circ}$  and  $17^{\circ}$ ), comparable normal thicknesses (1150 nm and 840 nm) and the same rotational frequency (6.0rpm). The results of the Gaussian fits give typical column spacings of

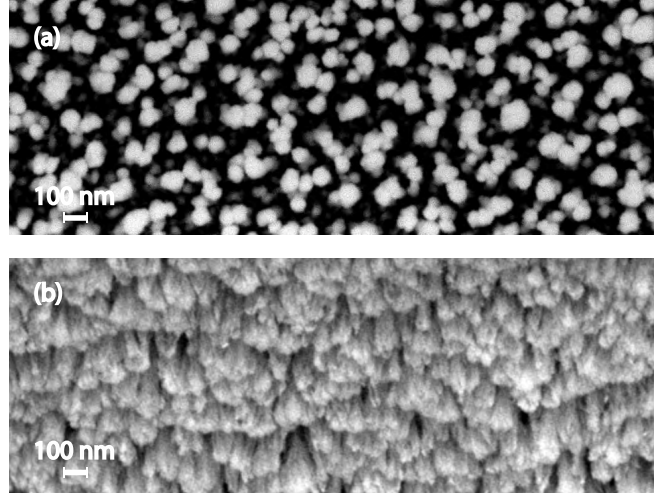


**Figure 3.7:** The meso-structured silica films imaged by SEM from a top view for two different samples. (a) Shows a sample with  $\Delta t_{\perp} = 1000$  nm,  $\theta = 7^{\circ}$  and  $\phi = 6.0$  rpm. For the sample in (b)  $\Delta t_{\perp} = 1324$  nm,  $\theta = 7^{\circ}$  and the film was grown without sample rotation.

$S_{\text{col}} = 160$  nm for the sample with a glancing angle of  $\theta = 7^{\circ}$ ,  $S_{\text{col}} = 125$  nm for the sample with a glancing angle of  $\theta = 12^{\circ}$  and  $S_{\text{col}} = 90$  nm for the sample with a glancing angle of  $\theta = 17^{\circ}$ .

The typical spacing between the pillars in the meso-structured silica samples thus decreases with increasing glancing angle of deposition. The decrease seems linear from these three points, which was not quite the case in [58], however, the films grown for the present studies are consistent with what has been achieved by others [56, 58] when the difference in sample thickness is incorporated.

It is essential in order to achieve a large Ps formation fraction from the meso-structured silica samples that the distance from the formation site inside the bulk material to an internal surface is short throughout the structured sample. Therefore it is expected that thinner pillars will maximise the Ps formation fraction both in reflection and transmission. The pillars become thinner with an increased glancing angle of deposition, but the column diameter is on the other hand also larger when the rotational frequency of the sample is large. A comparison between the standard sample and a sample grown with no sample rotation is shown in Fig. 3.7, where the SEM images from a top-view looking at a right angle to the surface are shown for the  $\Delta t_{\perp} = 1000$  nm,  $\theta = 7^{\circ}$  and  $\phi = 6.0$  rpm sample and a sample with the parameters  $\Delta t_{\perp} = 1324$  nm,  $\theta = 7^{\circ}$  and no rotation. The latter film is seen to be composed of pillars pointing downwards at an angle different from normal to

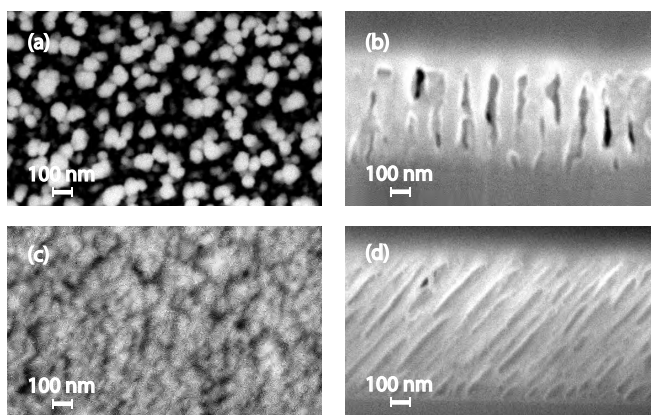


**Figure 3.8:** SEM images of two different meso-structured silica films from a top view (a) and (c) and in cross section (b) and (d). In (a) and (b) the  $\Delta t_{\perp} = 1000\text{ nm}$ ,  $\theta = 7^{\circ}$  and  $6.0\text{ rpm}$  sample is seen, whereas a sample with  $\Delta t_{\perp} = 1025\text{ nm}$ ,  $\theta = 12^{\circ}$ ,  $\phi = 0$  is seen in (b) and (d).

the surface.

This change in the directional preference of the pillars becomes very clear in Fig. 3.8, where a film grown at a glancing angle of  $\theta = 12^{\circ}$  and with no sample rotation is compared to the  $1000\text{ nm}$  normal thickness reference. These SEM images include the usual top-view image, but an image of the silica film in cross section was also recorded. A layer of amorphous carbon was deposited on top of the structured silica film for surface protection before the  $\text{Ga}^+$  FIB was used to cut a thin ( $70 - 100\text{ nm}$ ) cross sectional slice of the film. This slice was then imaged by the electrons in the SEM and mounted onto a small sample holder, which can be inserted into a TEM for an even more detailed imaging.

The inclination angle,  $\beta$  of the columns in Fig. 3.8d can be found from Eq. 3.1, which yield a value  $\beta_{\text{theory}} = 55^{\circ}$ . From the SEM image an angle,  $\beta_{\text{SEM}} = 45^{\circ}$  is found, which is off from the theory by  $10^{\circ}$ . This discrepancy can partly be explained by a misalignment of the cross sectional cut made by the FIB. This would be supported by the appearance in the SEM image of pillars that has been cut through by the FIB at an angle, and closed void may also appear. It is difficult to conclude whether this is the case, and the error from such an effect is probably no more than  $5^{\circ}$ .

In terms of Ps formation the sample grown in Fig. 3.8d is very promising, since the pillar diameter is seen to have decreased significantly compared to that in the  $1000\text{ nm}$  normal thickness reference. Furthermore, the spaces between the pillars have also decreased, thus facilitating more Ps-pillar collisions when the Ps diffuses to the surface, and the Ps would be expected to

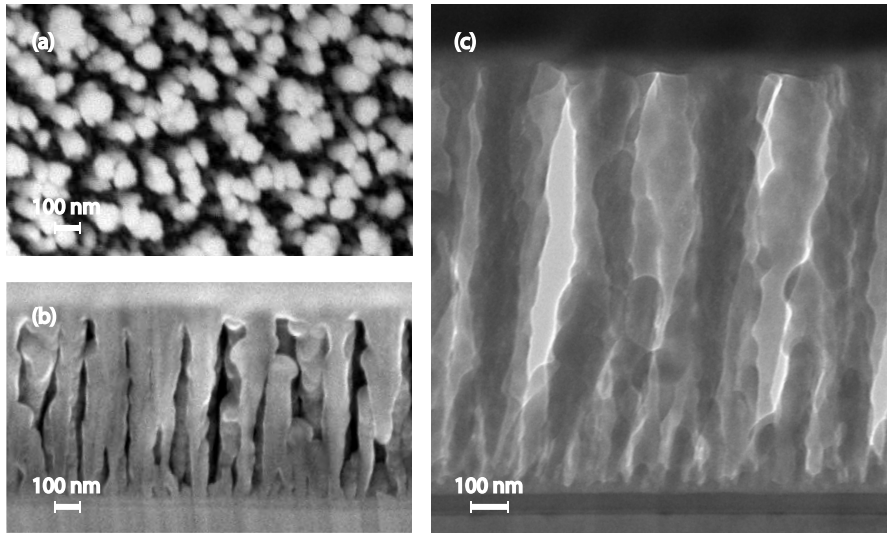


**Figure 3.9:** SEM images (a) and (b) and a TEM image (c) of a sample which has a non-porous layer (30nm) of silica between the carbon and the porous silica ( $\Delta t_{\perp} = 1370\text{nm}$ ,  $\theta = 7^{\circ}$  and  $\phi = 6.0\text{rpm}$ ).

cool more. The Ps formation from this sample still needs to be measured, and no conclusions are made at this point to if it actually works.

The further development of samples includes the evaporation of a non-structured layer of silica on top of the carbon foil before the meso-structured film is deposited. This layer is expected to reflect the formed Ps that moves towards the carbon foil, and SEM images of the sample are shown in Figs. 3.9a and 3.9b. The thin layer (30nm) of non-structured silica is seen on the cross sectional SEM image in Fig. 3.9. A thick ( $\Delta t_{\perp} = 1370\text{nm}$ ) layer of meso-structured silica is grown at a glancing angle of  $\theta = 7^{\circ}$  with rapid sample rotation,  $\phi = 6.0\text{rpm}$ , on top of the non-structured layer. This sample was successfully prepared for cross sectional TEM, and an image was recorded as shown in Fig. 3.9c. The purpose of the rather complicated processes where a cross sectional slice of the surface film is first cut out using a FIB, then mounted on a tiny sample holder and imaged using TEM is to determine the actual thickness of the film. A film thickness of  $H_{\text{film}} = 1100\text{nm}$  was found, which can then be inserted into Eq. 3.4 for a consistency check or conversely to calculate the density of the film. If Eq. 3.4 is assumed to be valid, then the film thickness is found to be  $\rho_{\text{film}} = 0.41\text{g/cm}^3$ , which is in very good agreement with the value estimated from the top-view SEM image of the 1000 nm normal thickness reference sample shown in Fig. 3.4. Therefore the film density is found (for these two thicknesses at least) to be fairly constant, which is employed in the following chapters to estimate the Ps formation and cooling

in the meso-structured silica samples.

### 3.3 Structured silica films supported by graphene

As will be discussed further in Chapters 4 - 6 it is essential to have a thin supporting film for the meso-structured silica film in order to optimise the formation and cooling of Ps in transmission. The carbon foils used for support in the work up to this point has a nominal thickness of 20 nm, but foils of thickness down to 5 nm can be acquired from the supplier. The problem in using thinner foils made of amorphous carbon is the strength and stability of such foils. The 20 nm foils are already quite fragile and must be handled with great care. Because of its vast strength, the use of graphene to support the silica structures has been proposed, and the development of a graphene-supported film was initiated.

In the first attempt to use graphene to support the silica films, a few sheets of commercial graphene monolayers grown on a copper substrate was ordered from the Graphene Supermarket [64]. The graphene was then supposed to be transferred to a high transmission copper grid, which should support the graphene on the Al ring also used earlier (see Fig. 3.1). This transfer was facilitated by chemical etching of the copper in a nitric acid of 68% concentration and subsequent rinsing in demineralised/deionised water. However, the graphene simply cracked when the water was evaporated off the film after the graphene was transferred to the copper grid. The problem was presumably that small cracks were already present in the graphene sheet when delivered in Aarhus.

Instead a more uniform sheet of graphene was grown locally via graphene synthesis by chemical vapour deposition (CVD) on Ni [65–67]<sup>7</sup>. A NaCl(111) crystal annealed at 500 °C for 30 min was installed into a vacuum system, which was pumped down to a base pressure of  $2 \cdot 10^{-7}$  torr. The 400 nm Ni film was grown onto the NaCl(111) crystal at 390 °C, after which the temperature was increased to 600 °C and stabilised for 5 min. Ethylene was then admitted into the system at a pressure of  $3 \cdot 10^{-6}$  torr for 5 min and graphene will synthesise on the Ni(111) surface. The Ni was then etched away by the nitric acid, rinsed in demineralised/deionised water and transferred now to a small stainless steel sample holder, which was earlier developed to fit into the original Ps multi photon ionisation setup.

The sample holder has a 1 mm diameter hole and was machined to have a sharp edge towards the hole as was also seen for the sample in Fig. 3.1 for the water to float off the graphene easily. The hole is seen in Fig. 3.10a, where the plain stainless steel surface that has been smoothly polished should also

---

<sup>7</sup>The following technical work on graphene was conducted by technician Bine Hansen

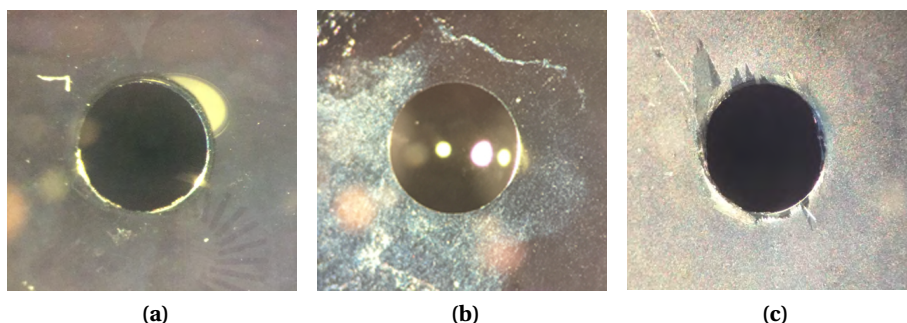


**Figure 3.10:** (a) Shows the hole over which the graphene is to be placed. (b) Shows an attempt to transfer the graphene from the Ni to the stainless steel holder and is supported by water. (c) Shows a graphene film with a meso-structured silica film on top.

be noticed. A graphene film, which is assumed to be composed of only a few atomic layers is transferred to the hole as shown in Fig. 3.10b, where the graphene film is supported by a drop of water. The film could be suspended across the hole for about 20 min, but cracked presumably when all the water had evaporated.

Macroscopic suspension of graphene has been demonstrated over a range of  $100\ \mu\text{m}$  using specially developed procedures [68], but the most commonly used suspended graphene membranes span much smaller distances [69, 70]. Thus, it is a large challenge to make a graphene membrane that is suspended over 1 mm with a rather simple approach compared to the scheme used in [68]. However, the graphene produced via CVD on Ni is expected to be more uniform and with fewer cracks than what has been used earlier. On the other hand, it has not been possible for us to achieve a stable membrane over these large distances so far. It may be useful to implement some variation of the scheme used in [68], but polymethyl-methacrylate (PMMA) is also known to provide a good support for the graphene in the transfer process (to other substrates) [71] and may be employed in the process here.

Another approach is to use the meso-structured silica film to support the graphene. This was attempted recently and the first result is shown in Fig. 3.10c, which illustrates another cracked film. The silica film is however seen to significantly change the optical appearance of the graphene, and more work should be done on this. For instance the stainless steel ring shown in Fig. 3.10 was polished and re-used in another attempt. The polishing of the holder decreases the sharpness of the edge, which causes the presence of water on the edge. When the water evaporates it may introduce a stress to the film at the edge that the graphene-silica sample cannot withstand, and it is ripped over as seen in Fig. 3.10c.

Graphene is useful in many aspects of the physical sciences and there are possible applications in many future technologies. If a surface is coated with graphene its properties change significantly, and thus it would also be interesting to use graphene in experiments with positrons. A first experiment would be to measure the Ps formation fraction for Ni(111) with and without a monolayer of graphene at the surface. The large mobility of electrons in graphene results in a change of the surface dipole term of the positron work function, and the Ps emission probability would be changed. Next, the graphene could be transferred to other materials for similar measurements.

For instance, graphene could be transferred onto both the reflection and transmission sides of a defect-free diamond (thickness  $\sim 100\ \mu\text{m}$ ) to make a graphene-diamond-graphene capacitor which would form a field assisted moderator if an external electric field is applied over the diamond, similar to the approach used in [72]. Positrons stopped in the diamond will drift along the electric field lines, and a high mobility should ensure large moderator efficiency.

Bilayered graphene would also be interesting to study with positrons, since it has a tunable band gap [73], which would make the Ore gap tunable, and a direct control of the Ps emission might be possible.



---

# Positronium formation in solids

In the present chapter, the formation of Ps in solids upon positron impact [74] and the subsequent emission into vacuum is discussed with a theoretical approach, and a preparation for an in-depth understanding of the measurements presented in Chapters 5 and 6 is given. If a dense concentration of Ps atoms in vacuum is required then formation in solids is the only option. First the traditional Ps formation in the reflection geometry is considered. Then the case of the transmission geometry is discussed with emphasis on the implications as well as simplifications that this geometry can provide to experimental setups and the cooling of Ps in general.

## 4.1 Positronium formation in metals and semiconductors

The formation of Ps in the bulk of metals is inhibited by electron screening that occurs due to the high density of free electrons in these materials. Thus the only possibility for Ps formation in metals is for the positron to capture an electron at the surface, where the electron density is somewhat lower (Ps could also be formed in defects in the bulk, but emission into vacuum is not possible in this case). There are several processes by which Ps can be emitted from a metal, reviewed in [23] or more recently in [75]. In order of decreasing final positron energy prior to Ps formation: (a) positronium can be formed upon surface electron pick-up from the conduction band in a quasi-elastic positron backscattering process where the positron loses a small amount of energy in a single or a few multiple scatterings. The yield of backscattered Ps is higher for low energy positron impact, and the Ps emission energy goes

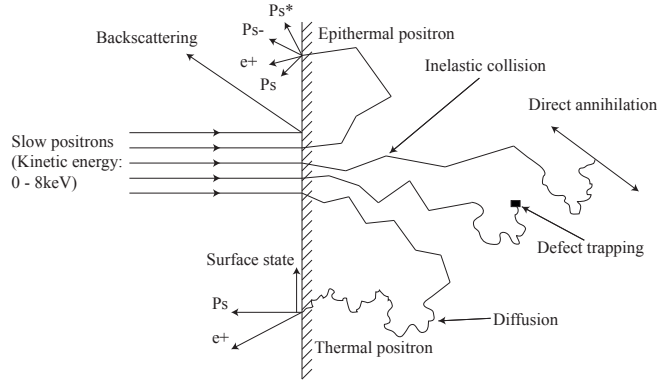


**Figure 4.1:** Positron implantation into a solid (metal). The processes involved are described in the text. Adapted from [80].

up to  $\sim 40$  eV or more for 50 eV positrons impinging Al, Cu, Ni and Au [76]. (b) The positron can penetrate the material slightly more and lose a significant amount of energy, but without thermalising completely. The epithermal positron may then pick up an electron at the surface with subsequent emission as epithermal Ps in the intermediate energy range (from thermal up to a few tens of eV) [77]. In contrast to backscattered Ps emission, the positrons undergo a larger number of scatterings and lose track of their incident angle in epithermal Ps emission. (c) If the positron implantation energy is large the implantation depth is large, and the positrons are very likely to thermalise before reaching the surface, causing the emission of thermalised Ps [78]. (d) Finally, the positron may lose energy at the surface by electron-hole pair creation or plasmon excitation and fall into a trapped surface state from which Ps can be emitted upon electron pick-up and thermal activation by sample heating [79].

The possible fate of the positron and the Ps emission processes (a) - (d) are summarised in Fig. 4.1. The emission of ground- or excited-state Ps ( $n_{Ps} = 1$  or  $n_{Ps} \geq 2$ , respectively) from the surface of a metal is governed by the positron reaching the surface at an energy larger than the Ps formation potential,

$$\epsilon_{Ps} = \phi_- + \phi_+ - E_{B,\text{vacuum}}/n_{Ps}^2. \quad (4.1)$$

Here  $\phi_-$  and  $\phi_+$  is the electron and positron work function respectively (defined in Eq. 2.3 for the positron and by  $\phi_- = D + \mu_-$  for the electron), and  $E_{B,\text{vacuum}} = 6.8$  eV is the ground state Ps binding energy in vacuum. Emission of ground state Ps formed from backscattering and epithermal positrons is possible because the positron energy easily exceeds  $\epsilon_{Ps}$ , and it has been shown that epithermal positrons form a significant fraction of excited state  $n_{Ps} = 2$  Ps [77]. However, to facilitate thermal Ps emission,  $\epsilon_{Ps}$  must be nega-

tive, and the positrons must be implanted deep enough into the material that they thermalise before diffusing back to the surface. The former requirement makes thermal Ps emission with a kinetic energy  $\leq -\epsilon_{\text{Ps}}$  in the ground state likely in a range of metals [23]. The Ps energy distribution resembles that of the conduction electron density of states, and the upper limit corresponds to the Fermi level of the solid, which is typically of the order of a couple of eV. The Ps formed by thermal positrons is thus not necessarily cold, and the distribution of energies may be wide.

Two processes competing with that of emission of Ps formed by thermal positrons is low energy positron emission and capture of low energy positrons in a surface state. The fraction of positron to Ps emission is approximately proportional to  $\sqrt{-\phi_+}$  [80], and the most negative positron work function would be preferred for positron moderators. To get as much Ps as possible, a positive positron work function, yet a negative Ps formation potential, is preferred. If the positron work function is positive or the positron loses energy near the surface, the positron is also very likely to be trapped in a surface state, and the trapped positron can be thermally activated to desorb Ps from the surface. For a positron surface binding energy,  $E_{b,\text{surface}}$ , the thermal desorption of Ps becomes energetically favourable if the activation energy,

$$E_a = E_{b,\text{surface}} + \phi_- - E_{B,\text{vacuum}}/n_{\text{Ps}}^2, \quad (4.2)$$

is exceeded by sample heating.

At room temperature, the Ps yield is due to formation by backscattered, epithermal or thermal positrons depending on the surface and with some fraction of positrons being trapped in a surface state. As the temperature is increased beyond the activation energy, the trapped positrons will form Ps that is emitted with a thermal energy distribution and with an increase in the Ps yield following an Arrhenius function:

$$f_{\text{thermal}} = f_0 + \frac{f_1}{1 + (\gamma_s/r_A)e^{E_a/kT}}, \quad (4.3)$$

where  $\gamma_s$  is the  $2\gamma$  Ps annihilation rate at the surface,  $r_A$  is the effective attempt rate for escape from the surface potential,  $f_0$  is the minimum Ps formation fraction and  $f_0 + f_1$  is the maximum fraction achieved at high sample temperature. Even though the energy of the thermally emitted component of Ps is increased by heating, the thermal emission of Ps serves as an effective cooling since the total mean of the Ps energy is decreased when taking into account all energy components of the Ps energy spectrum.

Thermal desorption of Ps has been observed for several metals (e.g. [81] or [82]), but also in germanium, which is a semiconductor [83]. In fact, the Ps emission mechanisms in Ge resemble those in a metal with no bulk Ps formation, and a large degree of thermal desorption. The band gap makes positron

thermalisation in Ge somewhat slower than in metals because the energy loss is restricted to phonon scattering at low energies. A primary mechanism for Ps formation at room temperature and at low positron energy is thus expected to stem from epithermal positrons.

Many experiments concerned with Ps formation (including the one described in Chapter 5 of the present thesis) use Ge(111) as a reference for 100% positronium formation, which is assumed at low positron energy and at high temperature (1000K). The calibration of the formation fraction using Ge at low positron impact energy and high temperature at a reference is discussed in Chapter 5 along with the use of mica as a reference for 0% Ps formation.

#### 4.1.1 Positron implantation in solids

To determine the amount of Ps emitted from the surface it is also necessary to determine the probability for the positrons to diffuse to the surface prior to emission. The positron diffusion can be found from the Ps yield as described in the next subsection. To determine the diffusion of the positron it is essential to know the initial state of the diffusion process, *i.e.* the penetration depth at which the positron thermalises. The mean implantation depth in any solid (metal, semiconductor, insulator) can be determined from the Makhovian implantation profile parameterised as

$$P(z, K) = \frac{mz^{m-1}}{z_0^m} e^{-(z/z_0)^m}, \quad (4.4)$$

where  $z$  is the variable implantation depth and  $z_0 = \bar{z}/\Gamma[(1+m)/m]$  for the mean implantation depth determined by the initial positron energy,  $K$ , in keV:

$$\bar{z} = \frac{A}{\rho} K^\nu. \quad (4.5)$$

The most recent determination of the parameters in the Makhovian, [84], find  $A = 2.81 \mu\text{g}/\text{cm}^2$  and  $\nu = 1.7$ , whereas  $m$  varies between 1.7 and 2.3 in the direct measurements of the implantation in different amorphous polymers. The measurements in [84] indicate that the mean penetration depth is independent of the structure for low- to medium  $Z$  materials and is only dependent on the density,  $\rho$ .

The values stated above are usually used when determining the positron diffusion in solids. The Makhovian profile is plotted for three different initial positron energies and for the densities of amorphous  $\text{SiO}_2$  and C in Figure 4.2a, using the values mentioned above and with  $m = 2$  for a Gaussian implantation profile. Also shown is the mean penetration depth at energies up to about 10keV for  $\text{SiO}_2$ , C and Ge. It is clear from these graphs that the positrons are stopped at a very localised position at low implantation

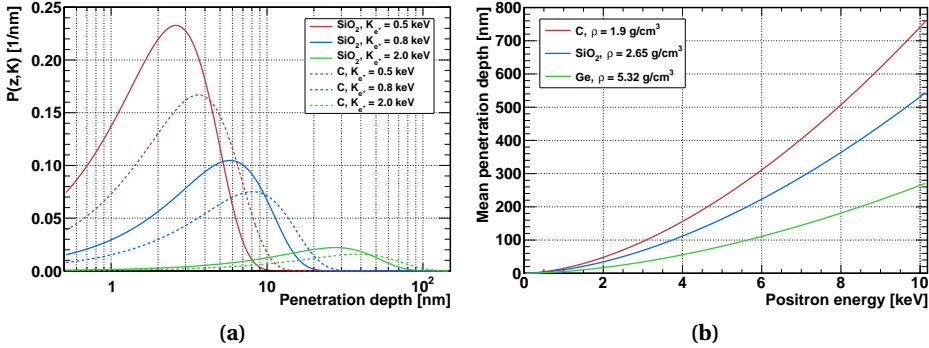


**Figure 4.2:** (a) Makhovian profiles for positron impact on amorphous carbon and silica at three positron implantation energies. (b) Mean positron implantation depth for carbon, silica and germanium. The mean depth only depends on the density of the material by Eq. 4.5.

depth, but the position of stopping is smeared out over a wide range of depths at higher implantation energy, as are the initial positions of the individual positrons for the diffusion motion that follows.

#### 4.1.2 Positron diffusion and thermal emission of positronium

It is possible to achieve knowledge about the diffusion and thermalisation of positrons in metals and semiconductors by measuring the fraction of Ps formed in the solid. This is because the fraction of positronium escaping to the vacuum indicates how large the diffusion to the surface from a given implantation depth is. The Ps formation fraction,  $f$ , is simply defined as the fraction of the impinging positrons that is emitted back into vacuum as Ps. This quantity can be measured as described in sec. 4.4. If the positrons are implanted deep into the solid, there is less probability for them to diffuse back to the surface and thus  $f$  goes down with increasing positron implantation energy.

Since the mean free path between positron scatterings in most solids is much smaller than the typical penetration depths the diffusion equation is assumed adequate in describing the positron motion to the surface. The three dimensional time dependent diffusion equation can be derived from the continuity equation [80]. The change in positron density,  $n_{e^+}(\mathbf{r}, t)$ , is given by

$$\frac{\partial n_{e^+}(\mathbf{r}, t)}{\partial t} = D_{e^+} \nabla^2 n_{e^+}(\mathbf{r}, t) - \lambda_{\text{eff}} n_{e^+}(\mathbf{r}, t) - \frac{\partial}{\partial \mathbf{r}} [v_d n_{e^+}(\mathbf{r}, t)], \quad (4.6)$$

where  $D_{e^+}$  is the positron diffusion coefficient,  $\lambda_{\text{eff}} = \lambda_b + \kappa_t C(z)$  is the effective annihilation rate, which includes bulk annihilations ( $\lambda_b$ ) and defect

trapping at depth,  $z$ , ( $\kappa_t C(z)$ ). The last term in the diffusion equation describes the drift of positrons in the material, and is only relevant when an electric field is present in the solid. This field may either be internally produced or applied externally, and can occur either in semiconductors or insulators, but is irrelevant for metals where no electric fields are present. The diffusion equation can be solved numerically. However, when applying appropriate boundary conditions, analytical solutions can also be found, even in the presence of electric fields [46]. The diffusion back to the surface can be viewed as a one dimensional process, and the initial positron density along the axis normal to the surface,  $z$ , is  $n_{e^+}(z, t = 0) = P(z, K)$ . In the case of no electric fields in the solid ( $v_d = 0$ ), a set of Eigen solutions can be found in one dimension, when the boundary condition of no positron density outside of the surface is implied [23]. This set forms a basis from which a general solution to the diffusion equation can be written, and the flux of positrons through the surface at  $z = 0$  is given by

$$L(a) = \frac{\exp(-a/(D_+ \tau_{\text{eff}})^{1/2})}{1 + \beta/(D_+ \tau_{\text{eff}})^{1/2}}, \quad (4.7)$$

where  $a$  is the  $\delta$ -function initial depth and  $\tau_{\text{eff}} = \lambda_{\text{eff}}^{-1}$  is the effective lifetime of positrons in the diffusing state. To find the yield through the surface from a general implantation depth distribution, which is here assumed to be the Makhovian profile,  $P(z, K)$ , the average  $L(a)$  over the implantation profile is taken for a given implantation energy,  $K$ :

$$\bar{L} = \int_0^\infty P(z) L(z) dz, \quad (4.8)$$

corresponding to the fraction of positrons reaching the surface. A first approximation for the implantation would be to assume that  $m = 1$  and an exponential penetration profile is attained. If this is the case, the integral in Eq. 4.8 can be solved to give the fraction of positrons diffusing back to the surface. Multiplying the result by the branching ratio for Ps emission,  $f_0$ , we get for the Ps formation fraction as a function of positron impact energy:

$$f_{m=1} = \frac{f_0}{1 + (K/K_0)^v}. \quad (4.9)$$

This function has been employed mainly in the early literature [83], but still sees some use as a first approximation, if not for anything else, then to provide an estimate of the half energy,  $K_0$  (the energy at which half of the positrons diffuse back to the surface of the sample) [85].

As indicated in [84], the shape parameter,  $m$ , is more likely to be around  $m = 2$ , which gives a Gaussian implantation profile as plotted in Figure 4.2a.

Using this parameter, the average over the implantation profile times the Ps branching ratio gives a Ps formation fraction of:

$$f_{m=2} = f_0(1 - A_1 K^v \exp(\pi^{-1} A_1^2 K^{2v}) \operatorname{erfc}(\pi^{-1/2} A_1 K^v)) , \quad (4.10)$$

where  $\operatorname{erfc}(x)$  is the complementary error function and  $A_1 = A/(\rho L_+)$  with the material dependent positron diffusion length,  $L_+$ , the density,  $\rho$ , and the mean penetration depth parameter,  $A$  as introduced earlier. A comparison of the two cases (exponential and Gaussian implantation profiles) is given in [23], and it is seen that the difference is quite small when positron energies up to about 6 keV are considered (in the experiments presented in this thesis, the maximum energy is about 8 keV or less), and either of the two can be used. If a comparison of diffusion parameters extracted from the two cases is required, the expression  $L_+ = (D_+ \tau_{\text{eff}})^{1/2} = (A/A') K_0^v$ , where  $A' = 1.0$  for the exponential expression and  $A' = 1.26$  for the Gaussian profile, can be used to extract the diffusion length,  $L_+$ , from the half energy,  $K_0$ , defined as the energy at which  $f = 1/2$ .

It is important to note that several complications exist that may cause a deviation from the expressions above, such as the presence of electric fields, trapping in defects, or incomplete thermalisation prior to diffusion, where the solution of the diffusion equation or the diffusion equation itself is inadequate. In addition, the amount of Ps may be underestimated in the experimental setup, since the Ps energy changes with impact energy, and the fast Ps could escape the detection region with the annihilation photons being detected at lower probability. The epithermal Ps component is usually largest at lower implantation energies, and thus the underestimation of  $f$  is presumably more significant at low implantation energies.

## 4.2 Positronium formation in insulators

In the previous section, the situation of Ps formation in metals and semiconductors was considered. The formation in these materials can only occur at the surface via conduction electron capture in the region where the electron density has somewhat decreased compared to the bulk density. The situation is fundamentally different when considering ionic solids and insulators. The density of electron states in the conduction band is non-existing in the ground state, and no screening of the positron is present in the bulk. However, in the absence of defects and for a material in the ground state, there is no electron available for the Ps formation, in contradiction with the sometimes rather large formation fraction observed.

There is solid evidence for the formation of Ps inside the bulk of insulators, which can be understood via two distinct processes. The slowing down

of positrons in insulators at larger energies happen via the creation of electron-hole pairs, and shortly after implantation, the insulator will be in an excited state with electrons available in the conduction band for Ps formation in the radiation spur [86]. Another possibility is direct positronium formation with a valence electron. This may happen if the positron energy is larger than the band gap energy,  $E_{\text{gap}}$  minus the Ps binding energy in the bulk,  $E_{b,\text{bulk}}$ , *i.e.* if  $K_{e^+} > K_{\text{min}} = E_{\text{gap}} - E_{b,\text{bulk}}$ , when it encounters a valence electron. The positron must not have thermalised completely for this to happen. On the other hand, the kinetic energy of the formed Ps must not exceed that of the binding energy of Ps in the bulk,  $E_{b,\text{bulk}}$ , or it will dissociate by collisions and end up in an unbound state. This type of Ps formation is referred to as formation within the Ore gap:

$$E_{\text{gap}} - E_{b,\text{bulk}} < K_{e^+} < E_{b,\text{bulk}} + K_{\text{min}} = E_{\text{gap}} , \quad (4.11)$$

and can in principle occur at all depths, with a probability for the Ps to diffuse back to the surface for emission into vacuum that decreases with the depth of the formation site. There is a change also that an epithermal positron will reach the surface and form Ps here via the Ore gap mechanism near the surface, but the probability for epithermal positrons to reach the vicinity of the surface decreases with implantation energy, and therefore formation of Ps via this mechanism is usually seen in the low energy region of impinging positrons.

Formation of Ps in the radiation spur of the positron occurs for positrons of energy larger than the ionisation threshold, however at both thermal and epithermal energies, but with an enhanced probability for positrons that have lost enough energy that electron-hole pair creation is inhibited. The Ps formed deep inside the bulk of an insulator will thermalise and diffuse to the surface where it may be emitted as free Ps. The difference from positron diffusion in solids is the larger probability for the Ps to get trapped in a defect before emission. If the Ps reaches the surface, thermal or not, the emission is governed by the Ps work function:

$$\phi_{Ps} = -\mu_{Ps} + E_{b,\text{bulk}} - 6.8 \text{ eV} / n^2 , \quad (4.12)$$

where  $\mu_{Ps} = \mu_+ + \mu_-$  is material specific Ps chemical potential obtained by adding the chemical potentials of the electron and the positron. A definition of the Ps work function makes sense only in dielectrics where Ps can form inside the solid, since by definition the Ps work function is the energy required to move a Ps atom from the bulk of a given material to a point just outside the surface.

As for positrons, the emission of thermal Ps into the vacuum is possible if the work function is less than zero,  $\phi_{Ps} < 0$ . The kinetic energy of the emitted

Ps when formed in the bulk by thermalised positrons is given by

$$T_{\text{Ps,bulk}} = -\phi_{\text{Ps}} = -\phi_+ - \phi_- + E_{\text{gap}} - E_{b,\text{bulk}} + E_B . \quad (4.13)$$

Capture of a valence electron at the surface is also a possibility, but if the band gap of the dielectric is large, the bulk emission of Ps is favoured over electron capture. The energy of the Ps formed in the radiation spur near the surface is given by

$$T_{\text{Ps,surf,cond}} = -\epsilon_{\text{Ps}} = -\phi_+ - \phi_- + E_{\text{gap}} + E_B , \quad (4.14)$$

which is larger than the energy of Ps formed and thermalised in the bulk. The difference in energy of the two components is seen for instance in the Ps formation in quartz [87].

### 4.2.1 Positronium formation in bulk silica

Bulk and surface Ps emission has been demonstrated from both single crystal quartz and amorphous silica. The bulk formation is documented by angular correlation of annihilation radiation (ACAR), where the annihilation of para-Ps from a delocalised state yields a narrow central peak [88]. In [87] the authors attribute the two energy components found from time of flight measurements in quartz and amorphous silica to the formation of Ps in the bulk and at the surface with energies at about 1 eV and 3 eV. The highest energy of these were also seen in [89], where it was found to be consistent with the excitonlike Ps formation in the bulk. However, the attribution by [87] is in agreement with the formation of Ps by electron capture in the radiation spur at the surface occurring at a higher energy (eq. 4.14) than Ps formed in the bulk (eq. 4.13).

The diffusion of positrons, para- and ortho-Ps to the surface of amorphous silica has been measured in a longitudinal setup, where the Doppler shifted component of the 511 keV peak in the annihilation spectrum stemming from para-Ps was extracted to find the formation of para-Ps [90]. The diffusion lengths found in these studies were  $L_{+, \text{SiO}_2} = (8 \pm 2)$  nm,  $L_{\text{p-Ps, SiO}_2} = (14.5 \pm 2)$  nm and  $L_{\text{o-Ps, SiO}_2} = (11 \pm 2)$  nm for positron, para-Ps and ortho-Ps respectively. It is thus important to keep the implantation into the bulk of amorphous silica within about 10 nm from the surface to maintain a high yield of Ps from silica.

### 4.2.2 Positronium formation in porous silica

As indicated above one can maintain a high yield of Ps into the pores of a porous silica, aerogel, grained silica powder, or the meso-structured silica samples discussed in Chapter 3 by making sure that there is always a short

distance to a surface and that the interconnectivity between pores and to the vacuum is high [91]. Thus if Ps can be formed within a diffusion length from an internal surface it has a high probability of being emitted into the pore network before it annihilates. If the porosity is large throughout the sample, the effective density is low and the positrons can easily reach the pores deep inside the structured- or porous silica, and the diffusion from deep inside the sample will cause a collisional cooling of the Ps before it is emitted into vacuum. In the meso-structured silica samples, the interconnectivity is indeed very large, however, the downside is that the pillars are in some cases too thick for Ps to be emitted into the pores or spaces between the pillars. This is the reason why we see a relatively fast decrease of the Ps yield in the measurements in Chapter 5, *e.g.* in Fig. 5.4. As seen in Chapter 3 some targets have already been produced that have a higher density of thinner columns than the targets used in Chapters 5 and 6.

Once Ps is formed in the meso-structured silica samples the Ps will diffuse to the surface. Since the spaces between the columns are much larger than the de Broglie wavelength of Ps,  $\lambda_{\text{Ps}} = h/\sqrt{2m_{\text{Ps}}E_{\text{Ps}}}$ , the classical diffusion picture holds in which the Ps bounces off the walls, and it is not necessary to consider confinement in the pores and quantum diffusion via tunnelling between pores. In Ref. [17] a diffusion model for the Ps diffusion has been developed, which is an extension of the positron diffusion model described in subsection 4.1.2. However, in the present model the Ps diffusion coefficient is allowed to vary with the energy of the Ps to incorporate the non-thermal diffusion. A variation with Ps energy is necessary since the initial emission energy is typically  $\sim 1$  eV and a significant loss of energy or cooling occurs during the diffusion. This stands in contrast to the positron diffusion in metals and semiconductors and the solution (Eq. 4.9) to the diffusion equation which describes thermal diffusion *i.e.* the positron energy is constant and so is the positron diffusion coefficient. In the present model, the Ps diffusion coefficient is assumed to be a function of energy,  $E_{\text{Ps}}$ :

$$D_{\text{Ps}}(E_{\text{Ps}}) \propto \sqrt{2E_{\text{Ps}}/m_{\text{Ps}}}, \quad (4.15)$$

where the proportionality constant depends on the spacing between pores and mean number of collisions in the pores. Assuming now the Makhovian initial condition with  $m = 1$ , *i.e.* an exponential positron implantation profile, then the fraction of Ps diffusing to the surface is given by

$$f = \frac{f_0}{1 + \bar{z}/\sqrt{D_{\text{Ps}}\tau}}, \quad (4.16)$$

where  $\tau$  is the mean lifetime in the pores. This gives the well known Eq. 4.9 when the Ps has thermalised (at large positron energy and implantation

depth). The diffusion equation is valid in small intervals of positron implantation energy, since for a small change in  $K$ , the Ps energy can be assumed constant. This gives a positron energy dependency of the formation fraction which is then given by

$$f = \frac{f_0}{1 + K^v A_1^{-1} (E_{\text{Ps}})^{-1/4}} . \quad (4.17)$$

where the Ps energy is found from the cooling model also applied in [17] and discussed in Chapter 6. As we shall see in Chapter 5, the diffusion model does not quite apply for the meso-structured silica targets used here because of incomplete thermalisation and because the energy dependency of the diffusion coefficient does not hold. Instead the simpler model with a constant diffusion coefficient is applied as an effective way of describing the data, as we shall see.

It is also possible to use the Gaussian ( $m = 2$  in the Makhovian profile) initial condition for the diffusion of Ps. This would result in a Ps formation fraction similar to that in Eq. 4.10 but with the Ps diffusion length being dependent on the Ps energy. The Gaussian implantation profile was used to describe data in [59, 92] with great success. The latter of these two references demonstrates a target for which the Ps formation fraction is constant with temperature, which is an essential parameter to control the Ps energy. However, usually the Ps formation fraction goes drastically down with the sample temperature [93], and thus the cost of a lower Ps energy is less Ps emitted from the surface.

When Ps is emitted into the pore network of porous silica or a meso-structured silica film, it will cool down as it diffuses to the vacuum. The cooling of Ps in these materials is considered in Chapter 6, where the experimental results on Ps cooling in reflection and transmission geometries [16] are also presented. The pore morphology has been shown to play a major role in the diffusion of Ps in structured silica and emission into vacuum [94] and the samples presented here possess a significantly different morphology compared to other samples studied so far. This is essentially what makes these targets interesting, along with the option of operating the Ps formation in transmission geometry and the optical accessibility along the beam axis through the target.

### 4.3 Positronium formation in transmission

Compared with Ps formation in the reflection geometry, the case of Ps formation in transmission has been rarely studied. The first experiment to produce transmission Ps in a solid utilised a thin carbon foil to neutralise the

positron beam and Ps was formed with an energy ranging from 10 to 500eV [95]. These energies would be useful in Ps beam experiments for instance when scattering cross sections for the Ps interaction with gasses are studied since the emission is quite forward directed, especially at the highest energies. On the other hand, the efficiency for Ps formation is only about 0.5% of the positron flux times the detector solid angle, and this very high energy is not suitable in the context of Ps cooling and laser experiments.

There are numerous practical and scientific advantages of using a transmission Ps formation target instead of a target for production in reflection geometry. As emphasised in [16], several experiments will benefit from an efficient transmission production of cold Ps, such as the conduction of free-fall Ps experiments [11], acceleration in a traveling laser field [96] and for the loading of an electron-positron stellarator [97]. The only experiment to study Ps formation in transmission at a reasonably low energy - besides the experiments presented in [15, 16] and this thesis - was conducted at Aarhus University more than 20 years ago. This experiment used heated Ag foils and is described below [82].

### 4.3.1 Thermal emission in Ag

The study of the emission of Ps in transmission through metal foils benefits greatly from the studies of positron energy moderation in transmission, since the thermal positron diffusion to the reflection/transmission surface occur for both thermal positron emission and emission of Ps formed at the surface. In [98] a theoretical description of positron diffusion to the reflection and transmission sides of thin single-crystal W(100) films is given. The basic assumptions to the one-dimensional diffusion model used in [98] are similar to that for a semi-infinite target, *i.e.* the Makhovian implantation profile of Eq. 4.4 provides the initial state of the thermal diffusion and the perfect-absorption boundary condition is used. However, in addition to this the finite target thickness is employed by taking into account that the fraction of positrons stopped in the film is given by  $\int_0^d P(z) dz$ , where  $P(z)$  is the Makhovian implantation profile and  $d$  is the sample thickness. The solutions to the one-dimensional diffusion model give a transmission probability of thermal positrons of

$$Y_T(K) = \frac{1}{\sinh(d/L_+)} \int_0^d \sinh(z/L_+) P(z) dz, \quad (4.18)$$

while that in reflection is

$$Y_R(K) = \frac{1}{\sinh(d/L_+)} \int_0^d \sinh\left(\frac{d-z}{L_+}\right) P(z) dz, \quad (4.19)$$

where in both of these equations  $L_+$  is the diffusion length of thermal positrons in the solid. The initial condition of the diffusion,  $P(z)$ , is as mentioned the

implantation profile. In the analysis in [82], both  $m$ ,  $v$ , and  $A$  (from the mean implantation depth of Eq. 4.5) are allowed to vary.

To find the transmission Ps emission probability, the ratio between the yields in transmission and reflection geometries are compared to the diffusion model. One gets

$$R_T(K) = \frac{Y_T(K)}{Y_R(100\text{eV})}, \quad (4.20)$$

which is essentially just the probability for the positron to thermalise and diffuse to the transmission surface, since in a relative measurement,  $Y_R(100\text{eV}) = 1$ . It is seen from Eq. 4.18 that what really matters when determining the probability of producing Ps in transmission is the ratio between the film thickness,  $d$ , and the diffusion length of positrons in that film,  $L_+$ . Indeed the diffusion length found in these studies was seen to be overestimated because of a distortion of the positron implantation profile when the mean implantation depth was approaching the transmission surface of the sample [99].

The estimated absolute Ps formation fraction in transmission through a heated (800 K) Ag(100) film of thickness 1900 Å was  $\sim 12\%$  found after applying several correction factors. These samples were successfully employed in the measurement of hydrogen charge exchange in transmission formed Ps [100], a process equivalent to the effective antihydrogen production scheme of [9].

### 4.3.2 Thin meso-structured silica film

The downside of using thin silver foils for transmission Ps production is that the sample needs to be heated to  $\sim 800\text{ K}$  for an efficient thermal activation. This is impractical in many setups and implies a Ps energy increase to the thermal energy at 800 K (though the mean energy may still decrease if epithermal Ps is emitted prior to the thermal activation). For use in the originally proposed multi photon ionisation experiment [49], heating the positron to Ps conversion target was not an option. Therefore the meso-structured silica thin films described in Chapter 3 were developed. Initially the idea was to use a helically structured silica film, but later the columnar structure used throughout this thesis was found to be more stable when producing films of the thickness required for Ps cooling.

Since the silica films are grown onto a thin carbon foil the positron implantation profile usually used does not apply. For implantation energies where the interface between the carbon foil and the silica film is traversed by some fraction of the implanted positrons, the implantation profile is modified as a result of the change in the effective material density. This was studied in [101], where positron implantation in multilayered structures was considered. The situation in the present setup depends on the orientation of the

thin sample with respect to the positron beam (as defined in Fig. 3.3), and both the Ps emission and the implantation profile changes drastically if the sample is flipped  $180^\circ$  between the reflection and transmission geometries.

Measurements in various materials show that the Makhovian implantation profile is close to being Gaussian, *i.e.*  $m = 2$ . Assuming now the usual mean implantation depth (Eq. 4.5) in a layer,  $i$ , of density  $\rho_i$ , then the implantation profile in the double layered structure can be found by making the substitution  $z \mapsto z - \delta_i$  in Eq. 4.4. Here, the parameter,  $\delta_i$  is implemented to get the normalisation right, since it must necessarily be such that only for positrons with an implantation depth longer than the thickness of the carbon foil will go through to the meso-structured silica film. The transmission probability,

$$T(z) = 1 - \int_0^z P(z') dz', \quad (4.21)$$

is required to be continuous for all  $z$ , where  $z = 0$  at the surface of the first layer is the reference point for all layers. This condition essentially just says that only the fraction of positrons transmitted through the first layer is relevant to the second.

Let us first consider the transmission geometry. Here the positrons are impinging upon the carbon foil of thickness 20 nm and density  $\rho_C = 1.9 \text{ g/cm}^3$ . The positrons are either stopped in the carbon foil or continue to the meso-structured silica of thickness 800 nm, porosity 15% and an effective density of  $\rho_{\text{SiO}_2, \text{struc}} = 0.4 \text{ g/cm}^3$ , where the latter is found from the bulk density and the porosity of the thin film as described in Chapter 3. These are the specifications of the target used for the Doppler spectroscopy measurements presented in Chapter 6 and [16]. SEM images of this target are shown in Figs. 3.8a and 3.8b. The parameter,  $\delta_{\text{SiO}_2, \text{struc}}$  was adjusted to fulfil the requirement of continuity of  $T(z)$  at the interface ( $\delta_{20 \text{ nm}} = -75.5975 \text{ nm}$  and scaling linearly for the other thicknesses). The positron implantation profiles at four impact energies (which were also used for the Ps energy measurements) are shown in Fig. 4.3a. It is seen that at 2.6 keV implantation energy, the profile just extends to the transmission surface of the silica structure. For lower energies a significant fraction of the positrons are stopped in the carbon foil, and thus are 'lost' for Ps formation in transmission. Only the positrons entering the meso-structured silica can form Ps in transmission, and only the positrons stopped close to the carbon foil can form Ps far enough away from the transmission surface that they will cool down by collision. The area of the positron implantation profile is normalised to 1, and thus any backscattering or interference effects at the surface or the interface have been ignored. In this respect, carbon seems like a good choice to support the silica films because of its low positron backscattering probability, and the low density also ensures a high transmission probability compared to other solids. The dis-

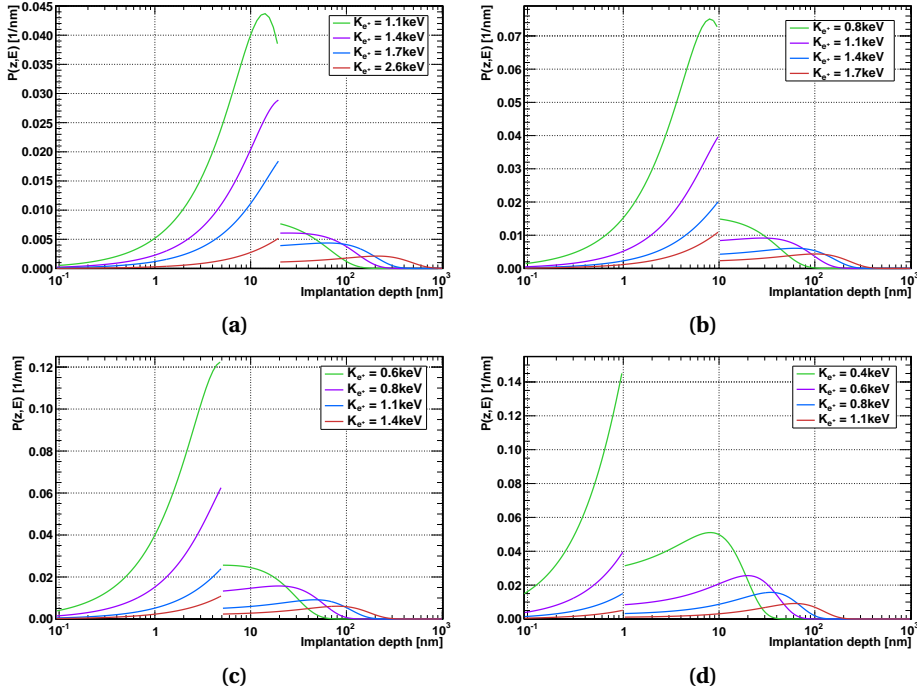


**Figure 4.3:** Modified positron implantation profiles of thin meso-structured silica films grown onto carbon foils of varying thickness. The carbon foil thicknesses are: (a) 20 nm, (b) 10 nm, (c), 5 nm and (d) 1 nm.

continuity in  $P(z, K)$  at an implantation depth corresponding to the carbon thickness arises from the abrupt change in density, and the value of  $P(z, K)$  changes by a factor of  $\rho_{i+1}/\rho_i$  when passing from layer  $i$  to layer  $i + 1$ . In reality however this discontinuity will be smeared out by the broadening of the distribution of positron energies, defects in the solids and variations in the carbon thickness.

In Fig. 4.3b, 4.3c and 4.3d, the thickness of the carbon foil has been decreased to 10, 5, and 1 nm, respectively. It is seen from these figures that the stopping probability in the carbon foil is decreasing as the carbon foil thickness is decreased for a given implantation energy. The transmission probability is increased and less implantation energy is required for the positrons to pass the carbon foil. As seen from these calculations, the ideal target would use a few mono-layers of graphene to support the silica structure. A sample of this kind is currently being developed as described in Chapter 3. The difficulty lies primarily in getting the graphene to support itself without breaking, and then afterwards make it support the silica.

The probability that the positrons will stop in a given layer,  $i$  (which can be either carbon, meso-structured silica or a fractional element in those lay-

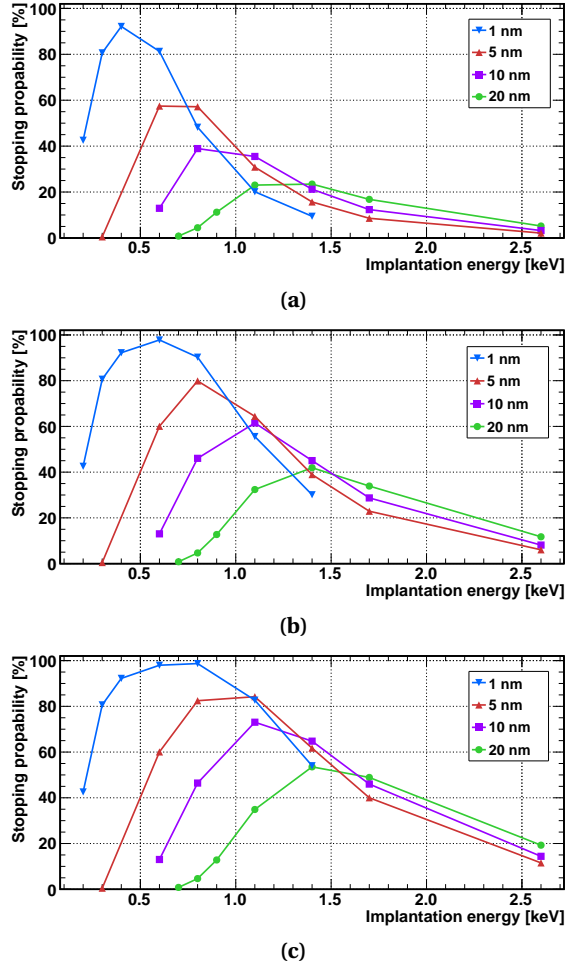


**Figure 4.4:** Stopping probabilities for the transmission geometry within (a) the first 40 nm, (b) the first 80 nm and (c) the first 120 nm of the meso-structured silica, corresponding to 5, 10 and 15% of the layer thickness, respectively. The carbon foil thickness is given in the legend.

ers) is

$$\eta_i(K) = \int_{a_i}^{b_i} P(z, K) dz . \quad (4.22)$$

and so the fraction of positrons that stop in the first 5, 10 or 15% of the silica structure can be found by integrating over the modified implantation profile.

A numerical calculation has been made to estimate the stopping probability deep inside the sample close to the carbon foil. The results are shown in Fig 4.4 for the same carbon foil thicknesses that were used in Fig. 4.3. The stopping probability within the first 40, 80 and 120 nm of the meso-structured

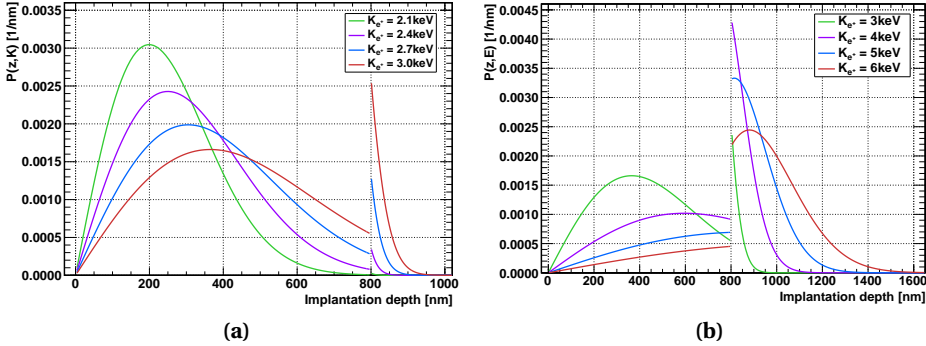


**Figure 4.5:** Positron implantation profiles at a range of positron energies in the reflection geometry. (a) Shows the onset of positron transmission through the sample, while (b) illustrates the implantation profiles at the positron energies that yield the highest stopping in the region close to the carbon foil, where most cooling is expected.

silica is shown for a range of positron implantation energies. The stopping of positrons can become very localised and thus Ps can be formed at a very localised position deep inside the silica structure if the carbon foil thickness is decreased. This results in a high density of Ps and enhanced cooling of Ps due to collisions with the columns compared with the reflection geometry for the same sample.

The same considerations that have been made above for the transmission geometry can be repeated for the reflection geometry in which the meso-structured silica film is hit directly by the positrons without going through the carbon foil first. In this case the low density material is implanted first and the discontinuity at the interface occurs at a depth of the thickness of the structured silica layer, *i.e.* at 800 nm in the sample considered here, and  $P(z, K)$  is increased by a factor equal to the ratio between the densities. This is shown in Fig. 4.5 where the probability of transmitting the positrons through the sample structure is seen to increase drastically with the implantation energy such that 0.5% of the positrons are transmitted through the sample at an energy of 2.4 keV, 8% are transmitted at 3 keV, 39% at 4 keV and 78% at 6 keV. Another interesting thing to consider is the fraction of positrons being stopped close to the carbon foil. This is clearly seen to be much less in the reflection geometry than in the transmission geometry, even with the 20 nm carbon foil used here. In the reflection geometry the maximum stopping probability of the positrons in a silica sub layer within 80 nm (corresponding to 5% of the silica thickness) from the carbon foil is  $\sim 8\%$  achieved at  $\sim 4$  keV. This result shows clearly that a significant enhancement of the fraction of cold Ps emission is expected when the positrons are implanted from the back of a silica

thin film as was also noted by [102].

The initial state of the Ps diffusion and cooling is the implantation profile of the positrons in the sample. As seen above the positron implantation profile is distorted significantly by the dual-layer semi-infinite structure of these samples. The fraction of Ps formed in transmission through a target having the silica structure pointing away from the beam source is due only to formation in the silica layer [15], and thus in principle the formation fraction could be extracted by integrating over the modified implantation profile from the thickness of the carbon foil  $\Delta t_C = 20\text{ nm}$  to the total sample thickness,  $d = 820\text{ nm}$  in Eq. 4.18. In the measurements conducted in these studies, however, there is no unique distinction between reflection- and transmission-formed Ps, and thus the Ps formation is more likely to follow the shape of Eqs. 4.18 and 4.19 added together and weighted by the (unknown) branching ratios for transmission and reflection formation, respectively. It is also noted that the reflection formation is expected to be solely due to Ps formation in the carbon foils, and thus the carbon part of the modified implantation profile,  $P(z, K)$ , integrated up to  $\Delta t_C = 20\text{ nm}$  in Eq. 4.19 should be used to calculate the reflection-formed Ps.

## 4.4 Quantifying positronium formation

There are several ways of detecting Ps formation upon positron implantation into a solid. The first quantitative analysis of the Ps formation in metals [74, 83] used a continuous beam of positrons and detected the energy spectrum of annihilation  $\gamma$ -rays (the 3- $\gamma$  method). This method is employed for some of the Ps-formation measurement presented in Chapter 5, and has the advantage of being absolute once the calibration has been carefully performed. On the other hand it takes a long time to gain significant statistics because of limitations due to a low count rate. The other method utilised here is single-shot positron annihilation lifetime spectroscopy (SSPALS) [103, 104] in which the signal stemming from the simultaneous annihilation of a large number of positrons is measured in an oscilloscope, and the delayed fraction is used to extract the Ps formation fraction. This method is superior in terms of statistical errors, and has the advantage of being able to register transient changes in the presence of Ps or the material used to convert positrons to Ps.

### 4.4.1 The 3- $\gamma$ method

It is possible to obtain the fraction of Ps formed upon positron implantation from a measurement of the positron  $\gamma$ -ray annihilation energy spectrum, since the  $\gamma$ -ray energy reveals the spin state origin of the photon. Two photon annihilation of a positron occurs either as direct annihilation, annihilation of

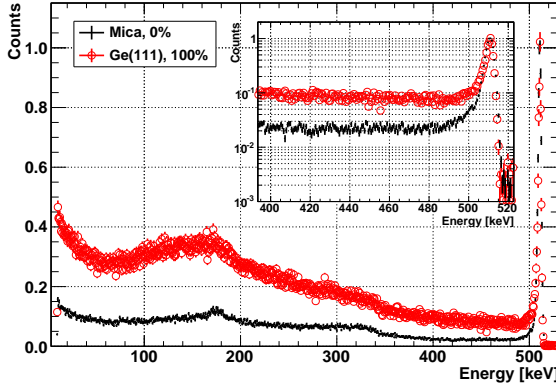


**Figure 4.6:** Comparison of positron annihilation energy spectra with 0% and 100% Ps formation and emission into vacuum. The spectra are normalised to a peak height of one. From [15].

para-Ps, or as pick-off annihilation of ortho-Ps that forms a singlet state with an electron in *e.g.* the target material. Because of energy and momentum conservation the energy of a  $\gamma$ -ray stemming from two photon annihilation is 511 keV. On the other hand, the annihilation of ortho-Ps will result in three photons that all possess an energy less than 511 keV, and the number of photons detected in certain energy ranges can be used to find the fraction of Ps emitted into vacuum.

In an experimental setup, the photon energy can be measured by either a NaI(Tl) detector or a High Purity Ge (HPGe) detector with the latter being superior in terms of energy resolution. An example of a  $\gamma$ -ray energy spectrum is shown in Fig. 4.6. From this spectrum the number of counts in the valley,  $V_f$ , (400 keV – 485 keV) and the peak,  $P_f$ , (506.0 keV – 515.6 keV) can be extracted for a given positron implantation energy,  $K$ , and positronium formation fraction  $f_{e^+ \rightarrow Ps}(K)$ . Defining the ratio between peak and valley counts,

$$R = \frac{V}{P} = \frac{\int_{V_{\text{low}}}^{V_{\text{up}}} \frac{dN(E_\gamma)}{dE_\gamma} dE_\gamma}{\int_{P_{\text{low}}}^{P_{\text{up}}} \frac{dN(E_\gamma)}{dE_\gamma} dE_\gamma}, \quad (4.23)$$

it can be shown that

$$f_{e^+ \rightarrow Ps}(K) = \left( 1 + \frac{(R_1 - R)}{(R - R_0)} \cdot \frac{P_1}{P_0} \right), \quad (4.24)$$

where  $R_1$  ( $R_0$ ) is the ratio between peak and valley counts 100% (0%) Ps emission and  $P_1/P_0$  is the ratio between peak values obtained from spectra of 100% and 0% Ps emission to vacuum. The 0% reference is found by implanting positrons at high energy deeply into mica, which will then emit no Ps and

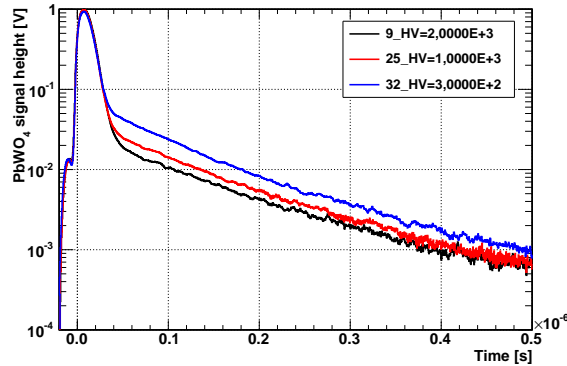


**Figure 4.7:** SSPALS spectra for positrons impinging upon a thin meso-structured silica sample at three different implantation energies. The spectra are normalised to a peak height of one. From [16].

all annihilation will occur into two photons. On the other hand, a heated Ge(111) crystal can be used to form 100% Ps at low positron implantation energy [83], since all the implanted positrons will then diffuse back to the surface and become thermally desorbed<sup>8</sup>. The reference measurements along with Ps formation measurements will be presented in Chapter 5.

#### 4.4.2 Single-shot positron annihilation lifetime spectroscopy (SSPALS)

Just like the  $\gamma$ -ray energy spectrum reveals the total spin Eigen state of the annihilating electron-positron pair, the time of detection of the quanta with respect to a common reference time,  $t_0$  also reveals the spin state. The longer living Ps annihilates after a delayed time, and SSPALS spectra like those in Fig. 4.7 can be obtained. Unlike the 3- $\gamma$  method (and the continuous beam equivalent, PALS [6]), SSPALS requires an intense pulse of positrons to work as intended. In fact, the technique was developed to be able to utilise the intense pulses extracted from a Surko trap [103, 104], and the bunch about  $5 \cdot 10^5$  positrons annihilate within a short time resulting in a signal in the detector, which is a convolution of the detector resolution function and the positron temporal profile. In addition to this, the shape of the signal also provides a signature of the various electron-positron spin state annihilations, being most prominent as a long-living tail from the decay of ortho-Ps.

It is important for the conduction of this experiment that the detector used has little afterglow and a short rise time *i.e.* the detector time resolu-

<sup>8</sup>As shown by [105], Ge(111) is more likely emit  $\sim 97\%$  of the impinging positrons as Ps which will introduce a systematic error, since the measured formation fractions will be slightly overestimated.

tion function has to be very narrow. Therefore a  $\text{PbWO}_4$  scintillating crystal is attached to a fast photomultiplier tube (PMT), and the signal is processed with a fast oscilloscope. The decay time of  $\text{PbWO}_4$  is  $\sim 9\text{ ns}$  for the crystal used in the Ps cooling experiment conducted at UCL [16] and discussed in Chapter 6, and the detector used in the Aarhus setup is similar and was provided by D. B. Cassidy and his group in a collaboration on the multiphoton ionisation experiment. To facilitate an accurate signal processing an oscilloscope with a broad bandwidth, high sampling rate, high resolution and low level of digital noise is required, although the choice of oscilloscope must be a compromise between price and requirement (high resolution, high sampling rate ADC's (Analog to Digital Converters) are very expensive). The oscilloscope used in the experiments conducted here is mentioned in the relevant chapters. To improve the resolution and noise level of the low amplitude tail of the signal in Fig. 4.7, a  $50\ \Omega$  resistive tee is inserted to split the signal into two before it enters the oscilloscope. This way the whole vertical range on the oscilloscope can be used to acquire the tail in one channel, while the signal timing is ensured by measuring the gross signal in another channel. The signals are spliced together in the analysis, which is done online in a LabVIEW program that provides an instant estimate of the Ps formation fraction<sup>9</sup>. A software Constant Fraction Discriminator (CFD) trigger defines the timing of each pulse, and the delayed fraction is defined as the ratio between the integral of the delayed part of the signal (35 ns to 350 ns) to the total integral of the signal ( $-3\text{ ns}$  to 350 ns),

$$f_d = \frac{\int_{-35\text{ ns}}^{350\text{ ns}} V_{\text{osc}}(t) dt}{\int_{-3\text{ ns}}^{350\text{ ns}} V_{\text{osc}}(t) dt}, \quad (4.25)$$

where  $V_{\text{osc}}(t)$  is the signal voltage at a time,  $t$  after the common zero.

The delayed fraction and the Ps formation fraction are not the same quantity, however the formation fraction,  $f$  is proportional to the delayed fraction,  $f_d$ . The proportionality constant depends on the geometrical environment in which the specific measurement is conducted, and varies due to different detection efficiencies for the  $2\gamma$  and  $3\gamma$  annihilation photons. An approximate expression that resembles the signal in the detector is provided by [85], where this relative detection efficiency is assessed, but here we just mention that the intensity of  $3\gamma$  annihilations is given by  $f_{3\gamma} \approx f_d e^{t/\tau}$ , where  $\tau$  is the lifetime of the decay of the tail in the SSPALS spectra and  $t = 35\text{ ns}$  is the start time of the delayed integral of the signal. The quantity  $f_{3\gamma}$  is only about 3/4 of the amount of Ps formed, but it gives an approximate estimate of the amount

---

<sup>9</sup>The LabVIEW program used for signal processing in Aarhus was written by Adam Deller, but has been extended for a few specific purposes as mentioned later.

of ortho-Ps formed, which is also the amount of Ps available for laser excitation and ionisation described later in this thesis. The SSPALS method is in fact perfectly suitable for use with lasers, since laser induced changes in the delayed fraction can be measured in coincidence with the pulsed laser overlapping Ps cloud.

---

# Positronium formation: experiment

The formation of positronium in the meso-structured samples described in Chapter 3 has been extensively studied experimentally as a major part of the present work. The results of these studies are presented in this chapter, and experimental details that were initially avoided for brevity in [15] are discussed in more detail here. The Ps formation fraction is measured in the reflection and transmission geometries, and results obtained using two distinct techniques are presented. Data obtained from energy measurements of the annihilation  $\gamma$ -rays in the  $3\gamma$  method using the continuous positron beam are first analysed and presented. The data is then compared with data obtained using the SSPALS techniques and a bunched beam of many positrons. The latter method is also employed in Chapter 6 for laser spectroscopy.

## 5.1 Experimental setup

To measure the fraction of formed Ps using the  $3\gamma$  method and a continuous beam of slow positrons, a suitable vacuum chamber was constructed in extension to the existing setup. Reasonable high vacuum conditions ( $\sim 1 \cdot 10^{-8}$  mbar base pressure) was obtained in the interaction region that consisted of a DN100CF 6-way cross by attaching a 360 L/s turbo molecular pump with an oil free backing pump to avoid hydrocarbonate contaminants. The positrons were guided to the interaction chamber by a longitudinal magnetic field provided by the extraction solenoid (140 G) and the interaction Helmholtz configuration (130 G) shown in Fig. 5.1 ensured a small beam diameter at the silica sample. A stainless steel target holder was mounted on a one-dimensional manipulator from the top of the vacuum chamber, and was capable of hold-

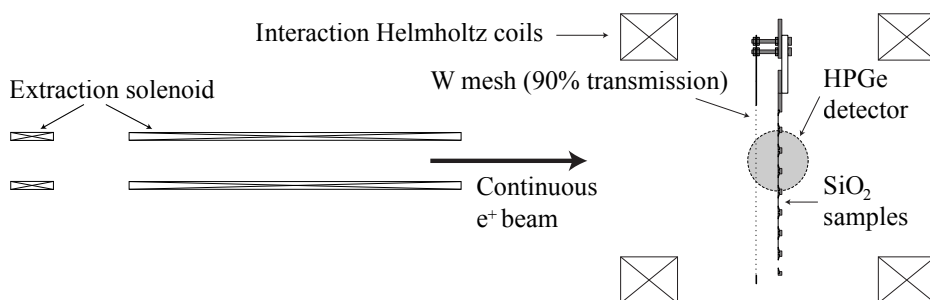


**Figure 5.1:** The extraction solenoid provides a longitudinal magnetic field that transports the positrons to the interaction chamber, where alignment is done using the empty target position at the bottom of the target holder. The positron energy is controlled by applying a potential difference between the grounded tungsten mesh and the negatively biased target holder.

ing 7 samples at a time, leaving one open slot for alignment, which was made easy by inserting an MCP with a phosphor screen behind the target holder (typical MCP bias:  $V_{\text{front}} = -1.85\text{ kV}$ ,  $V_{\text{back}} = 0\text{ kV}$  and  $V_{\text{screen}} = 4\text{ kV}$ ). The target holder was isolated from ground by a piece of aluminium oxide ( $\text{Al}_2\text{O}_3$ ), and a negative bias was applied to the samples to achieve positron implantation energies in the range from 0 – 8 keV. A grounded (90% transmission) tungsten (W) mesh was installed  $\sim 25\text{ mm}$  in front of the target holder to ensure a constant field gradient in front of the target.

To measure the Ge(111) reference for 100% Ps formation, a second manipulator was introduced from the side, and the Ge(111) crystal was mounted onto a tantalum (Ta) target holder to reduce the outgassing into the system when the sample was heated, and to preclude damage of the silica samples from unnecessary heating. The germanium sample was also isolated from ground by an aluminium oxide block, which was also holding a tungsten filament cut out of a 250 W halogen bulb which was connected to a high current feed through. The temperature of the sample was manually controlled by a K-type thermocouple mounted onto the tantalum holder close to the Ge(111) crystal. The positron energy was again controlled by applying a negative bias to the target holder - this time the maximum achievable positron energy was  $\sim 3.5\text{ keV}$  or less, since above this energy electrical break down would occur. The base pressure was about  $1 \cdot 10^{-6}\text{ mbar}$  when the temperature of the sample was highest, which is not impressive compared to the  $1 \cdot 10^{-8}\text{ mbar}$  when no heat was applied to the Ge(111) crystal. The mica used for the 0% reference was positioned in one of the 7 sample positions on the target holder used for the structured silica samples.

During the initial adjustments of the setup, the MCP was left on while the Ps formation fraction was measured. On the MCP a small variation of the

beam position of  $\sim 2$  mm in  $\sim 1$  min was seen to occur due to an unidentified charging of some component in the beamline. At the default continuous beam settings, the positron spot diameter was about 8 mm in the 130 G interaction field, and such large variations would cause a significant fraction of the positrons to hit the Al ring instead of the silica sample. A systematic error arises from this effect, which is very difficult to take into account, and furthermore would cause non-statistical fluctuations in the Ps formation fraction. These fluctuations can only be smeared out if the duration of one measurement at a specific energy is very long compared to the period of the position variations of the positron spot, or alternatively the data acquisition can be randomised for the variations in  $f$  to appear at random energies.

The solution to the problem was in fact none of the above (although the order of the energies were also randomised). Instead the beam was collimated in the moderator area by reducing the Helmholtz field at the moderator to only 30 G, while the beam tube solenoid field was reduced to 125 G. This way, the continuous rate of positrons was significantly reduced following a reduction in spot diameter by about a factor of two, and the artefacts in the data disappeared. It should be mentioned that the MCP was used only for alignment with the target holder grounded, and was switched off and grounded for the actual measurements.

As illustrated in Fig. 5.1, a high purity germanium (HPGe) detector was setup externally to measure the energy spectrum of the  $\gamma$ -rays stemming from the positron and positronium annihilations in the interaction region. The detector was positioned on the opposite side of the manipulator with the Ge(111) crystal at a distance of approximately 20 cm away from the centre of the vacuum chamber where the target is located. Since the distance to the detector is fairly long, the solid angle of the detector is about the same for the  $\gamma$ -rays stemming from two-photon annihilation inside the sample or at the surface, and for Ps atoms flying away from the surface. Furthermore, because the detector is positioned at a right angle to the beam direction and centred at the target position there is symmetry between the reflection and transmission sides of the target as defined in Fig. 3.3, and no difference in the detection efficiency is expected.

All the  $3\gamma$  measurements have been conducted in Aarhus using the setup described above. The SSPALS measurements presented in section 5.5 were conducted both at University College London and at Aarhus University using the setup described in the Chapters 4 and 6.

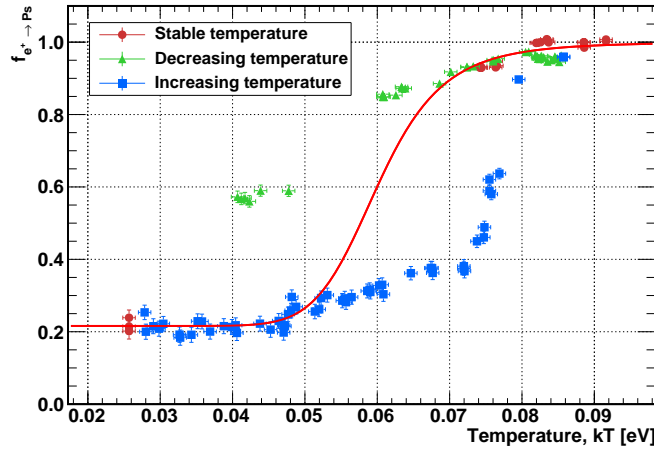


**Figure 5.2:** The temperature dependency of the Ps formation fraction,  $f$ , for the Ge(111) surface. The three data sets were taken under different temperature conditions as described in the text, and the solid red line is an attempt to estimate the data based on Eq. 4.3. The target bias was set to 10V for the reemitted positrons to impinge the surface again.

## 5.2 Calibrating the $3\gamma$ method

When positrons are implanted shallowly into the Ge(111) crystal held at room temperature both thermal and epithermal Ps is expected to be emitted from the surface [75]. However, a fraction of the positrons lose more energy than  $-\phi_+ > 0$  in the vicinity of the surface and get trapped either in the image potential or in localised defects at the surface in the near surface region [105]. As described in Chapter 4, it is energetically favourable for the positron to bind to an electron and be emitted as Ps upon thermal activation when the sample is heated. The Ps formation fraction<sup>10</sup>, was measured as a function of the sample temperature as measured by the thermocouple mounted on the tantalum holder as shown in Fig. 5.2. Initially, the temperature was increased rather fast by increasing the current through the tungsten filament, and the Ps formation fraction was measured by recording a  $\gamma$ -ray energy spectrum at each temperature (blue squares in Fig. 5.2). In fact, the temperature was still rising while the measurement was taken, and a thermal equilibrium did not occur before the next temperature was set. This procedure continued in a second dataset in which the temperature was decreasing and changed before a thermal equilibrium had been reached (green triangles in Fig. 5.2). A hysteresis in the data is seen as the temperature is first increased then decreased straight ahead. Therefore these initial data are not reliable in terms

<sup>10</sup>Actually the ratio between the peak and valley counts was measured and used for the calibration. Afterwards the fraction  $f$  was calculated based on the references found.

of extracting the 100% Ps formation reference,  $R_1$ , or for that matter the activation energy of the thermal desorption process. Another measurement was conducted to make sure that the temperature had stabilised before the measurement of the photon energy spectrum was initiated (red circles in Fig. 5.2). This latter measurement could be used to determine the 100% reference since the Ps formation fraction,  $f$ , stabilised at high temperatures, and  $R_1 = 1.763(12)$  was found by averaging the measured values of the Ps formation fraction for temperatures,  $kT > 0.08\text{ eV}$ , *i.e.* for  $T > 930\text{ K}$ .

The solid red line in Fig. 5.2 is an attempt to estimate the actual shape of the thermal activation data based on Eq. 4.3. It is based on a  $\chi^2$  minimisation to the stable temperature (red circles) data, but with some constraints applied. First, the parameter  $f_0$  from Eq. 4.3 should be approximately given by the average of the three points taken at room temperature, and  $f_0 = 0.216$  can be fixed in the fit. Secondly, the Ps formation fraction does not exceed 100%, and therefore  $f_0 + f_1 = 1$  if the data is assumed to be properly calibrated, and  $f_1 = 0.784$  is fixed in the fit. Thirdly, because of the shape of the hysteresis, the temperature at the Ge(111) surface must be overestimated in the ‘blue squares’ data, and underestimated in the ‘green triangles’ data. Thus an upper limit of the activation energy is estimated by manually adjusting the activation energy to  $E_a = 0.8\text{ eV}$ . If  $E_a$  is fixed at this adjusted value and the minimisation of the ‘red circles’ data is done only by varying  $\gamma_s/r_A$  in Eq. 4.3. This results in the red solid line in Fig. 5.2, which starts to increase just as the ‘blue squares’ data starts to increase. This estimate corresponds roughly to what would be obtained by including the blue data up to about  $kT = 0.05\text{ eV}$  in an ordinary fit, however, it builds in physical principles rather than a pure statistical analysis. An upper limit of  $E_a \sim 0.8\text{ eV}$  is consistent with the value of found by [105] when taking into account the trapping into localised defects near the surface, although the authors in [105] use a Ge(100) surface rather than the Ge(111) surface used here.

Once the temperature has been increased to above 1000K it is important to ensure a shallow penetration of the positrons into the Ge crystal. This was done above by setting the target holder bias to 10V, such that the implantation energy is about 18eV, when the initial energy of the positrons from the moderator is taken into account. The positron implantation energy has also been varied for various constant Ge(111) surface temperatures in addition to the temperature dependency discussed above. In fact, this was done before the measurements discussed above, with the Ps formation fraction following Eq. 4.9 nicely as a function of the positron implantation energy. Surprisingly, no change in the shape and size of  $f$  as a function of the positron energy was observed below 800K, and in contradiction with the later measurements of Fig. 5.2, the value of  $f$  at 18eV implantation energy was about 0.35. As the temperature was further increased to 886K, the formation fraction suddenly

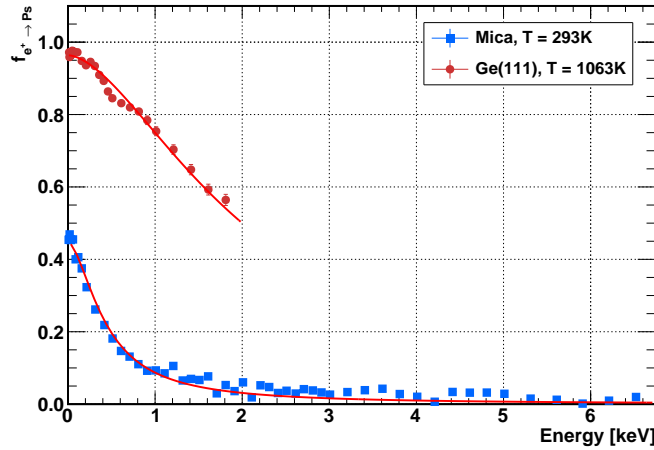


**Figure 5.3:** The Ps formation fraction as a function of the positron implantation energy for Ge(111) at 1063K and for mica at room temperature. The data has been fitted to Eq. 4.9

started to increase drastically with the implantation energy. This is certainly not the usual behaviour of such a measurement, and can only be explained by a rapid change in the temperature that counteracts the increase in positron implantation (these data were taken with a continuous increase of the energy, and the data points were not randomised), or a change in the surface conditions. Assuming a relatively reliable temperature measurement the first possibility is excluded, and what is indirectly observed is rapid evaporation of some contaminant (presumably oxides) from the surface. Since the Ge(111) surface was exposed to air before the measurements of Fig. 5.2 were conducted, this may also explain the hysteresis observed in those measurements. However, the ‘stable temperature’ measurements of Fig. 5.2 were taken without breaking the vacuum after ‘increasing/decreasing temperature’ measurements were conducted, and thus the germanium sample were effectively annealed *in situ* prior to ‘stable temperature’ measurements resulting in a clean Ge(111) surface.

The positron energy could then be increased with the sample being held at 1063K and the expected decrease in  $f$  with the implantation energy was observed as shown in Fig. 5.3. The data has been fitted to Eq. 4.9 to yield a half energy,  $K_0 = 2.09(4)$  keV and a formation fraction at zero implantation energy,  $f_0 = 0.964(3)$ . The formation fraction is not quite 100% at low implantation energy, which is explained by the fact that the temperature of the sample was decreased to room temperature and increased again to high temperature but thermal equilibrium may not have been established before the positron implantation energy was increased. The measured value of  $K_0$  is

about a factor of two lower what has been measured earlier [106], which has not yet been explained.

Let us now return to the reference measurements for the calibration of the  $3\gamma$  method. The 0% Ps formation reference was found from positrons implanted deeply into a piece of mica installed in the target holder for the silica samples. This measurement is also shown in Fig. 5.3. The reference value was found (obviously) before  $f$  was calculated by extrapolating  $R$  to infinite energy as  $1/K$ , which was also done originally in [83]. The value found for the 0% reference was  $R_0 = 0.4009(18)$ . The peak values for the low energy and high temperature Ge(111) measurement ( $P_1$ ) and the ‘infinite energy’ mica measurement ( $P_0$ ) could then finally be combined to give the last reference value,  $P_1/P_0 = 0.2692(10)$ . Using the reference values found in this section, the Ps formation fraction is found in the following sections for the meso-structured silica samples.

The last thing to mention in the present section is that the mica data has also been fitted to Eq. 4.9, and  $K_0 = 0.433(7)$  and  $f_0 = 0.448(3)$  was found. The important thing to notice is not the actual values found here, but rather the fit, which has a high value of  $\chi^2$  pr. number of degrees of freedom. The estimate by the fit is lower than the data points at higher energies, which indicate that the reference value  $R_0$  has been slightly underestimated. This is presumably due to the  $1/K$  extrapolation used by tradition, and a systematic error arising from this deviation is discussed later.

### 5.3 Ps emission from meso-structured silica in reflection

When Ps is formed in reflection from the thin meso-structured silica samples described in Chapter 3 the formation is expected to occur inside the solid pillars from where the Ps diffuses to an internal surface. The Ps atom is then emitted into the open spaces between the pillars where a diffusion-like process takes it to the surface of the sample for emission into vacuum. During the diffusion to the surface a number of collisions with the pillars cause the Ps atoms to lose energy and cool down before it is emitted into vacuum.

As already discussed, the amount of Ps formed in the silica sample and emitted into vacuum depends upon the morphology of the sample. With the calibration of the  $3\gamma$  method presented above the Ps formation fraction can now be found as a function of the positron impact energy for various target parameters, *i.e.* for different normal thicknesses, glancing angles of silica deposition and values of the rotation frequency. The meso-structured samples can be employed to form Ps both in the reflection and transmission geometries as defined in Fig. 3.3. Experimental results of the Ps emission in

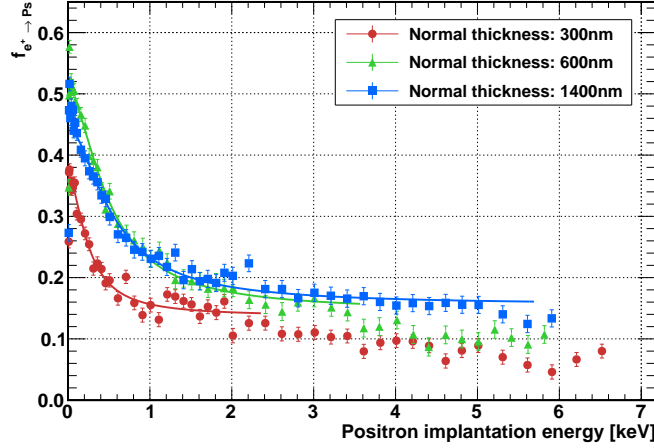


**Figure 5.4:** The Ps formation fraction in reflection as a function of the positron implantation energy for three meso-structured  $\text{SiO}_2$  films produced with different normal thicknesses and the same glancing angle of deposition ( $\theta = 7^\circ$ ) and rotational frequency ( $\phi = 6.0\text{rpm}$ ). The data has been fitted to Eq. 4.9 but with a constant parameter added to it as described in the text.

the traditional reflection geometry from the meso-structured silica samples, measured using the  $3\gamma$  method, are presented in this section.

The normal thickness of the samples,  $\Delta t_\perp$ , is the quantity which is directly variable in the target production procedure. The normal thickness is proportional to the density-thickness product,  $\rho_{\text{film}}H_{\text{film}}$ , according to Eq. 3.4, if the glancing angle of incidence is kept constant. The Ps formation fraction,  $f$ , has been measured as a function of the positron implantation energy for three different normal thicknesses ( $\Delta t_\perp = 300\text{nm}$ ,  $\Delta t_\perp = 600\text{nm}$  and  $\Delta t_\perp = 1400\text{nm}$ ) and with the same glancing angle and rotation frequency of the samples ( $\theta = 7^\circ$  and  $\phi = 6.0\text{rpm}$ ) as shown in Fig. 5.4. These sample growth parameters result in three samples consisting of vertical pillars, which are equally distributed when the growth is initiated. As the thickness is increased, however, the chance of pillar extinction is increased because the pillar diameter is increased resulting in a larger shadow (this effect is further enhanced by the very small angle,  $\theta = 7^\circ$ ), and the average distance between the pillars becomes larger. Thus for the thicker samples, the positrons will experience a larger column spacing and a larger column diameter when implanted shallowly into the sample.

Also shown in Fig. 5.4 is a fit of each data set (same colour) to Eq. 4.9 but with a constant parameter,  $f_\infty$ , added to it. Since the films are thin, the implantation profile is distorted by the interface between the layers, and the transmission surface of the carbon foil, and Eq. 4.9 is only valid as long as the sample can be considered as infinite in the direction perpendicular to

Morphology	$\Delta t_{\perp}$ [nm]	$\theta$ [°]	$\phi$ [rpm]	$f_0$	$K_0$ [keV]	$f_{\infty}$
Pillars	300	7	6.0	0.234(11)	0.25(2)	0.137(4)
Pillars	600	7	6.0	0.364(7)	0.50(3)	0.145(5)
Pillars	1400	7	6.0	0.293(7)	0.55(3)	0.155(4)
Spirals	100	7	0.6	0.356(16)	0.24(2)	0.077(7)
Spirals	100	11	0.6	0.35(2)	0.27(4)	0.051(12)

**Table 5.1:** Parameters for the fits to Eq. 4.9 of the data shown in Figs. 5.4 and 5.5. The value of  $\chi^2/\text{ndf}$  is close to one for all the fits.

the sample surface. This may be assumed if the implantation energy is low enough that the positrons stay inside the silica structured and does not reach the carbon foil. As a simple estimate, the implantation energy should be lower than the energy at which the positrons reach the carbon foil on average. The film density found for the  $\Delta t_{\perp} = 1000$  nm film that was analysed in Chapter 3 is used,  $\rho_{\text{film}} = 0.4 \text{ g/cm}^3$ , as an estimate for all the films in Fig. 5.4, while the normal thickness is used as the thickness. The implantation energy at which the carbon foil is reached on average is then  $\sim 2.3$  keV for the  $\Delta t_{\perp} = 300$  nm film, it is  $\sim 3.5$  keV for the  $\Delta t_{\perp} = 600$  nm film and it is  $\sim 5.7$  keV for the  $\Delta t_{\perp} = 1400$  nm film. These energies are used as upper limits for the fits in Fig. 5.4. For the lower limits of the fits it is noted that there are a few outliers in the data at low implantation energy, which are consistently present in all data sets. These are to be discussed below, but for now the fit should steer clear of these points.

The fits of the data in Fig. 5.4 are seen to describe the data quite well with  $\chi^2/\text{ndf} \sim 1$  and the parameters are summarised in table 5.1. At energies above the cut-off energy for the fits, however, there is a tendency that the data decreases below the constant value,  $f_{\infty}$  provided by the fit to values at lower energy. This decrease occurs presumably because the initial condition (in this case an exponential Makhovian implantation profile) for the diffusion process to the reflection surface becomes invalid when the positrons start to reach the carbon foil. The data also show that the thicker the silica film the larger the Ps formation fraction at high energy, whereas at low energy the optimum normal thickness would be around  $\Delta t_{\perp} = 600$  nm according to these measurements.

Another sample morphology can be obtained by changing the angle of deposition or the rotation frequency, and a three dimensional sculpturing of the samples are possible as described in Chapter 3. In Fig. 5.5 two measurements are shown for samples with different glancing angles of deposition ( $7^\circ$  and  $11^\circ$ ), but the same rotational frequency ( $\phi = 0.6$  rpm) and normal thickness ( $\Delta t_{\perp} = 100$  nm). The small rotation frequency ensures a thin film consist-

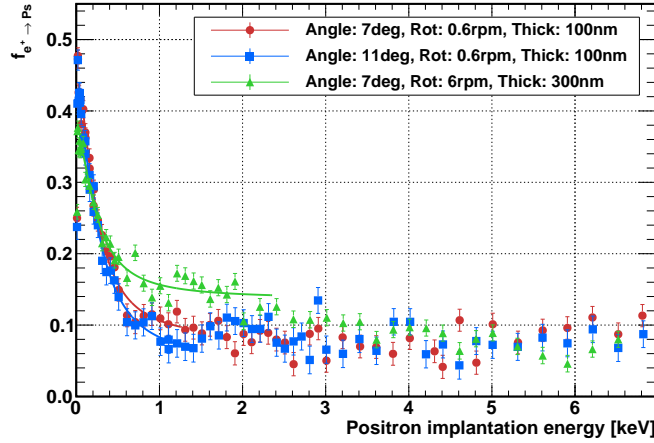


**Figure 5.5:** The Ps formation fraction in reflection as a function of the positron implantation energy for three meso-structured  $\text{SiO}_2$  films. The film with  $\Delta t_{\perp} = 300\text{nm}$  is shown again for comparison, the other two samples have the same normal thickness and rotation frequency, but different glancing angles. The data has been fitted to Eq. 4.9 but with a constant parameter added to it as described in the text.

ing of spirals instead of vertical pillars, which were used for the three samples characterised in Fig. 5.4. The  $\Delta t_{\perp} = 300\text{nm}$  sample consisting of pillars is also shown in Fig. 5.5 for comparison, since this target has a thickness which is relatively close to that of the samples with slow rotational frequency, and provides the most direct comparison of the two morphologies in the absence of samples with equal thickness. The data for the films of normal thickness,  $\Delta t_{\perp} = 100\text{nm}$  has been fitted up to an energy of  $\sim 1.2\text{keV}$ , and the fitted parameters for these data have also been summarised in table 5.1.

Only a small change in the Ps formation fraction is seen for the two samples of different glancing angle. In fact the only significant difference is in the fitted parameter,  $f_{\infty}$ , which is slightly larger for the sample with a glancing angle of  $11^{\circ}$ . Both the Ps formation extrapolated to zero energy and the half energy are found to be the same within error. This can be seen as an indication that a smaller spacing between spirals does not make a big difference. However, the change in angle is quite small and no SEM images have been taken of these particular samples to quantify the resulting change in the spiral spacing, and therefore no conclusions can be drawn on this matter.

The Ps formation fraction for the third sample in Fig. 5.5, which is composed of pillars instead of spirals, is seen to be smaller at low positron implantation energy, larger at intermediate energies and the same as for the two other samples at large energy. The larger fraction of Ps emission between implantation energies of  $0.5\text{keV}$ - $3.5\text{keV}$  is expected to be due to the larger thickness of this sample compared to the other two samples for which data is pre-

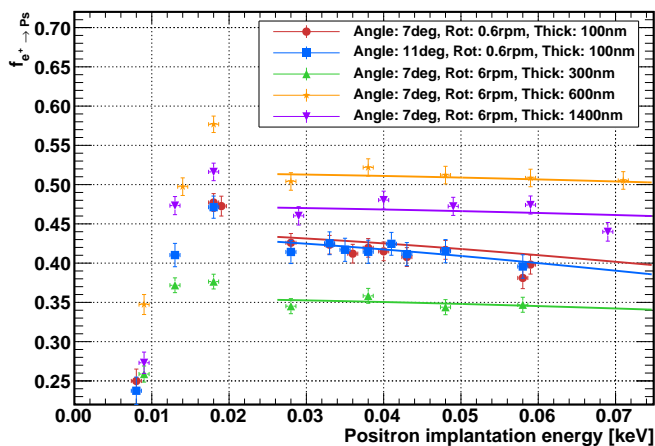


**Figure 5.6:** The Ps formation fraction as a function of the positron implantation energy for all the five samples studied in reflection.

sented in Fig. 5.5. The positrons reach the carbon foil at lower implantation energy if the film is thinner, resulting in less Ps emitted. It would be interesting to try to make thicker samples with spirals to study the morphological dependency of the Ps formation fraction and diffusion of Ps to the sample surface systematically, but for now these measurements indicate that more Ps can be formed in thin films consisting of spirals than in films composed of pillars.

As mentioned there are some outliers at low positron implantation energy, which are common to all the data presented in Figs. 5.4 and 5.5 for Ps formation in reflection. These outliers are also seen in Fig. 5.6, where all the five sets of data are shown for implantation energies from 0 – 75 eV. Unfortunately the energy steps in these measurements were not small enough that the underlying structure can be revealed. However, for all the measurements besides the measurements for the  $\Delta t_{\perp} = 300$  nm samples, there is a clear peak in the Ps formation fraction in the vicinity of 18 eV positron impact energy. This peak is interpreted as Ps formation within the Ore gap of silica, which was also seen for crystalline ice in [107]. It is noted that the position of the peak may also change due to sample charging by the positrons. If a fine scan was done with high statistics it should be possible to characterise the structure of the Ps formation fraction and possibly reveal other peaks arising from some other band gap in the solid.

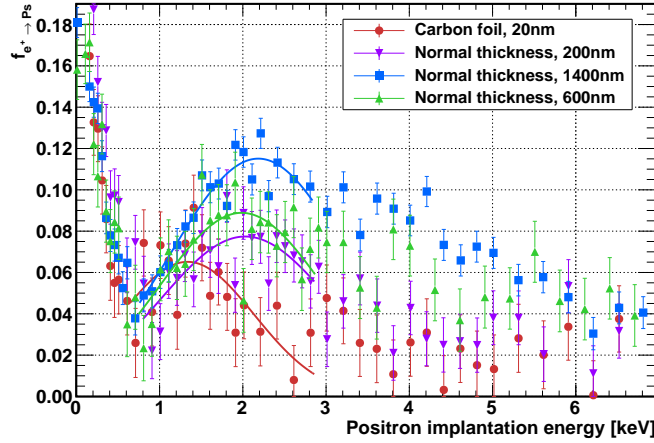


**Figure 5.7:** The Ps formation fraction as a function of the positron implantation energy for three different meso-structured silica samples positioned in the transmission geometry and for a plain carbon foil. Gaussian fits are performed to estimate the peak values of the Ps formation fraction for Ps formed in transmission.

## 5.4 Ps emission from meso-structured silica in transmission

Besides the directly controllable morphology of these samples, another very interesting and promising feature of the thin meso-structured silica samples is the emission of Ps in the transmission geometry defined in Fig. 3.3. The positrons impinge upon the carbon foil, are transmitted to the meso-structured silica if the energy is large enough and form Ps, which diffuses to the transmission surface. Three measurements of the Ps formation fraction as a function of the positron implantation energy are shown in Fig. 5.7 for three different samples with different normal thicknesses,  $\Delta t_{\perp} = 200$  nm,  $\Delta t_{\perp} = 600$  nm and  $\Delta t_{\perp} = 1400$  nm. Also shown is a measurement of the Ps formation fraction for a plain carbon foil with no silica grown onto it.

As emphasised in Fig. 5.8 the Ps formation fraction for the three samples with the structured silica on the transmission side follow that of carbon at low positron implantation energy. This is expected because at low energy the positron implants only the carbon foil, and up to a certain implantation energy the carbon seems infinitely thick to the positrons. From the carbon foil data it is seen that around 0.7 keV the Ps formation fraction starts to increase, which is actually the case for the other samples as well. This is in contradiction with an infinitely thick sample, and positron/Ps diffusion to the transmission side becomes a possibility. The fits to Eq. 4.9 of the data in Fig. 5.8 at low positron implantation energy all have  $\chi^2/\text{ndf} \sim 1$ , and the

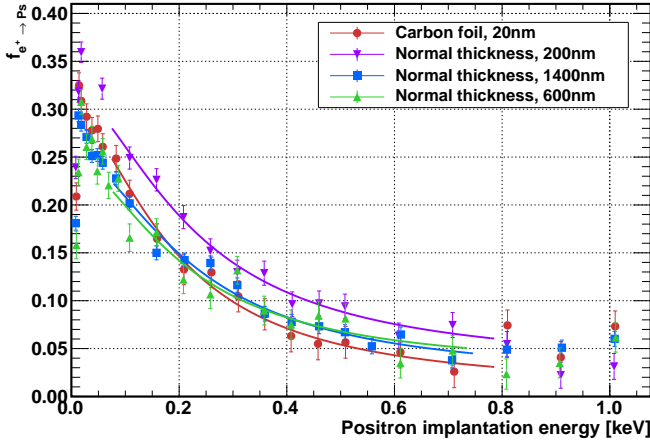


**Figure 5.8:** The Ps formation fraction as a function of the positron implantation energy for three structured silica films in the transmission geometry, and for a plain carbon foil. The formation occurs in reflection from the carbon foil at low energy in all cases, and the data has been fitted to Eq. 4.9.

Morphology	$\Delta t_{\perp}$ [nm]	$\theta$ [°]	$\phi$ [rpm]	$K_{\text{mean}}$ [keV]	$f_{\text{Gauss}}$
Carbon foil	20	-	-	1.34(12)	0.065(6)
Pillars	200	7	6.0	2.03(10)	0.077(4)
Pillars	600	7	6.0	1.99(9)	0.089(5)
Pillars	1400	7	6.0	2.19(6)	0.115(3)

**Table 5.2:** Parameters for the Gaussian fits used to estimate the Ps formation fraction in transmission as shown in Fig. 5.7. The carbon foil does not have a layer of silica grown onto it and  $\Delta t_{\perp}$  in this table represents the real thickness for the carbon foil.

half energy  $K_0$  found from the fits agree within error with an average value of  $K_0 = 0.21(5)$  keV. However, the  $\Delta t_{\perp} = 200$  nm data is shifted slightly upwards, which may indicate that there is a small offset in the calibration for this sample (the detector could have been placed slightly different for this measurement).

Simple Gaussian fits (with no background added) have been used to estimate the Ps formation fractions as shown in 5.7. The fitting parameters are summarised in table 5.2 for a convenient overview. Only the mean positron energy values  $K_{\text{mean}}$  at which the Ps formation fraction is highest, and the Gaussian amplitudes  $f_{\text{Gauss}}$  used to estimate the maximum Ps formation fraction in transmission are relevant, since a Gaussian is not necessarily expected to describe the data. The Gaussian fits are thus only used as simple estimates, which was also done in [15]. The silica structure grown with a normal thick-

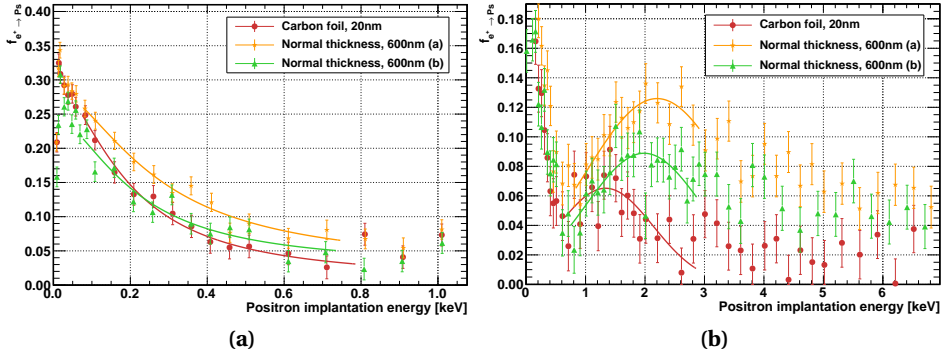


**Figure 5.9:** Two independent measurements of the Ps formation fraction in transmission as a function of the positron implantation energy for the same sample. Also shown is a measurement of the Ps formation in a plain carbon foil. (a) Shows the Ps formation at low energy with fits to Eq. 4.9. (b) Shows the total range of the measurements, and Gaussian fits are used to estimate the maximum Ps formation fraction.

ness of 1400 nm is seen to have the highest yield of Ps formed in transmission. This is in contrast to what was found in [15], where the maximum yield was obtained for the film with a normal thickness of 600 nm, and a small decrease in the output was seen as the normal thickness was increased. The reason for this discrepancy is that the measurement presented here is different from that presented in [15], although the same sample was used.

The two measurements are shown in Fig. 5.9 for comparison, where the low energy part (a) and the total range (b) has been plotted separately. Also shown in the figures is data obtained with a plain carbon foil. The first measurement (a) shows a clear shift upwards in the Ps formation fraction at low positron energy in comparison with the Ps formation fraction for the plain carbon foil and the other measurement for the silica sample (b). It is not known exactly what causes this deviation, which is seen to result in an over-estimation of the Ps formation fraction in the meso-structured silica film with  $\Delta t_{\perp} = 600$  nm with respect to the other samples. However, the geometry does not have to change by much to introduce systematic variations in the Ps formation fraction arising from a change in the relative efficiency for the detection of  $2\gamma$  and  $3\gamma$  annihilation quanta. It is believed though that the most reliable measurement is the one that reproduces the carbon data most precisely, and therefore measurement (b) has been used in the present analysis and is the measurement shown also in Figs. 5.7 and 5.8.

A first attempt to model the Ps formation fraction in transmission uses the approach of Subsec. 4.3.2 to find the initial condition of the diffusion of Ps to the transmission surface. In the same way that Eq. 4.21 is used to find

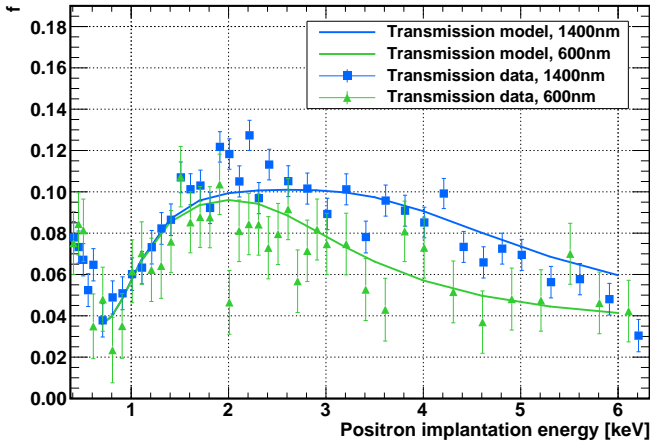


**Figure 5.10:** A simple model is developed to describe the Ps formation fraction in transmission. The model is here compared to the data for two different samples.

the fraction of positrons stopped within a distance of 5, 10, and 15% of the sample thickness from the carbon foil in Fig. 4.4, it can be used to find the fraction of positrons stopped within a sample of a given thickness,  $H_{\text{film}}$ . Recall from Chapter 3 that the actual film thickness of the sample with a normal thickness,  $\Delta t_{\perp} = 1400\text{nm}$  is around  $H_{\text{film},1400} = 1100\text{nm}$ . If a simple linear scaling is used then a normal thickness of  $\Delta t_{\perp} = 600\text{nm}$  corresponds to an actual film thickness of  $H_{\text{film},600} = 470\text{nm}$ . Assuming a linear scaling of the film thicknesses is equivalent to assuming that the mean density is the same throughout the sample since the product  $H_{\text{film}}\rho_{\text{film}}$  is proportional to the normal thickness (Eq. 3.4).

The stopping probability within the sample starts to increase when the positron implantation energy becomes large enough that the positrons enter the silica. This happens at an implantation energy of  $0.7\text{keV}$ , which is equal to the minimum in the measured Ps formation fraction within errors. The  $1400\text{nm}$  sample is thick enough that about 95% of the positrons can be stopped inside the structured silica film if the implantation energy is about  $3\text{keV}$ . However, the data peaks at around  $2\text{keV}$ . This is accounted for (or at least attempted to be accounted for) by multiplying the probability for the positron to stop inside the silica sample by the probability of Ps emission in reflection at the same positron implantation energy. The result is then scaled (divided by 2.5) and an offset (0.035) is added to get the model curves shown in Fig. 5.10 for the 600 and 1400nm normal thickness samples. The data for the two samples are also shown in the Fig. 5.10, and a fairly good agreement is found between the model and the data, although some discrepancies are still present.

One discrepancy is that the 600 nm data is slightly lower than the model in the region of the peak, which could be accounted for by introducing a different and smaller offset for these data compared to the other set of data. However, to keep things as simple as possible the same offset was used for both sets of data. Another thing to notice is that the 1400 nm data is higher and more peak-like at the maximum value around an implantation energy of 2 keV compared to the model. A sharper peak could possibly be modelled if the positrons were allowed to lose energy in their passage through the carbon foil before they implant the structured silica. This would allow a shallower implantation into the pillars, and thus a larger probability of emission into the open spaces. In fact, the silica samples used here are different from the usual porous silica used elsewhere [17], since the pillars are relatively thick and positrons that are stopped inside the pillars may not be able to diffuse to an internal surface before annihilation. In addition, if Ps is emitted at a high energy in the open spaces between the pillars it may re-enter the material and annihilate there because of the large column diameter. In many types of porous silica the Ps atom would continue to lose energy and after a short distance reach another surface to be reemitted into the pores.

On the other hand the Ps atom will easily diffuse to the surface of the film once it is emitted into the open spaces with low enough energy that re-entry into the bulk is forbidden. This is evidenced by the model above, which shows that the Ps formation fraction as a function of the positron implantation energy resembles the probability for the positrons to stop within the sample of a given thickness. This indicates that the formed Ps easily diffuses to the transmission surface, and the Ps formation fraction is maximised when a large amount of Ps diffusion to an internal surface is achieved by shallow implantation into the pillars.

To investigate the processes involved in Ps formation in the meso-structured silica films in more detail it is first of all necessary to measure the Ps formation fraction more precisely, *i.e.* to reduce the statistical errors. A comparison of films with different thicknesses can then be made with reduced systematic errors on the Ps formation fraction if one makes sure to use the exact same geometrical condition for all the measurements.

## 5.5 Comparison of SSPALS and the $3\gamma$ method

One way of reducing the statistical errors in a measurement of the Ps formation fraction is to use SSPALS, which was described in Sec. 4.4. This is clear from the measurements in Fig. 5.11, which show the delayed fraction  $f_d$  as a function of the positron implantation energy. Recall here that  $f_d$  cannot be directly compared with the Ps formation fraction  $f$ , but  $f_3 \approx f_d e^{35\text{ns}/\tau}$ , where

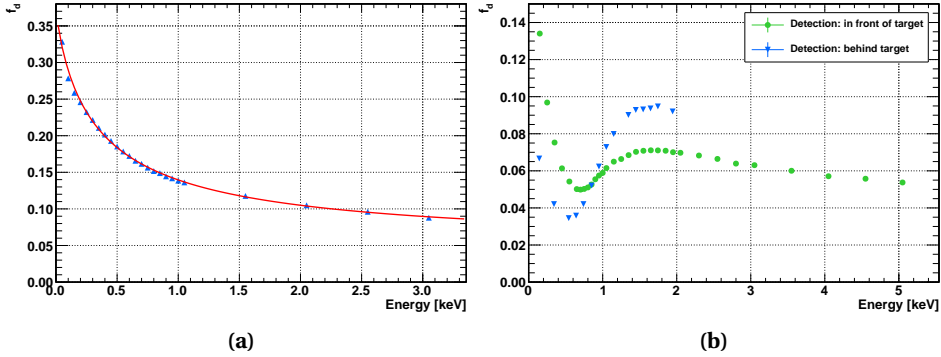


**Figure 5.11:** The delayed fraction  $f_d$  as a function of the positron implantation energy in (a) the reflection geometry and (b) the transmission geometry for a sample consisting of vertical pillars, *i.e.* with  $\theta = 7^\circ$ ,  $\phi = 6.0$  rpm, and  $\Delta t_\perp = 1000$  nm. These measurements were conducted at UCL and are presented in [16].

$\tau \approx 140$  ns is the mean lifetime of the ortho-Ps decay in the measured lifetime spectra and  $f_3$  is the fraction of ortho-Ps formed upon positron impact. This value should be multiplied by  $4/3$  to also take into account the formed para-Ps, which is included in  $f$ . The 35 ns is the lower limit of the delayed integral of the lifetime spectrum.

The measurements of  $f_d$  shown in Fig. 5.11 were conducted during a visit in David Cassidy's laboratory, where the cooling of Ps in the meso-structured silica samples was measured as discussed in Chapter 6 and [16]. The delayed fraction was measured both in reflection and transmission geometries. In the reflection geometry, the detector was positioned in front of the target to maximise the efficiency of detecting  $\gamma$ -rays from annihilation of ortho-Ps emitted in reflection. In the transmission geometry the detector was positioned behind the sample by default, and Fig. 5.11b shows the consequence of moving the detector from the front of the sample to behind the sample when measuring the delayed fraction. The difference in the two measurements occurs simply because of a change in the efficiency of detecting the  $3\gamma$  annihilation quanta. The formed Ps atoms are moving away from the PWO detector in the transmission geometry if the detector is in the front of the sample and towards the detector if the detector is positioned behind the sample. This changes the detector solid angle, and a smaller signal is seen if the annihilation occurs far away from the detector. This effect is further complicated by changes in the Ps energy with the positron implantation energy, since fast Ps annihilated at a longer distance away from the detector, which causes a smaller detector efficiency for these annihilations.

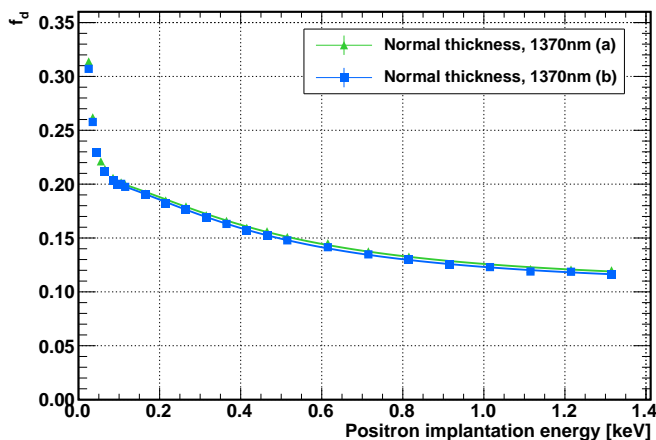
The geometrical effects on the experimental results are very clear from

Fig. 5.11b. In the SSPALS setup the PWO detector has to be positioned close to the sample to achieve a reasonable signal. This is not necessary with the  $3\gamma$  method since the HPGe detector is much more efficient than the PWO, and in fact one should be careful not to saturate the signal. Because the detector is positioned further away from the sample in the  $3\gamma$  method the effect of Ps traveling away from the sample is less distinct for this method.

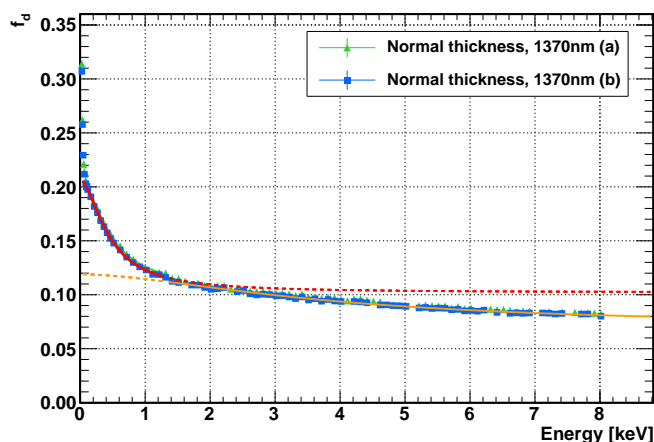
A fit of the SSPALS data in Fig. 5.11a has been performed to estimate the shape of the data. It was not possible to get a good fit using the parameter  $\nu = 1.7$  in Eq. 4.9. A fit to Eq. 4.17 was also attempted, since Ps is cooling down via collisions in the meso-structured silica [16], but the fit to this equation was not better than the first one. The fit seen in Fig. 5.11a employs  $\nu$  as a free parameter, and the best fit value is  $\nu = 0.844(17)$  in Eq. 4.9, with a constant  $f_\infty$  added to it for an effective description of the data. This value of  $\nu$  is also employed in a fit to describe the cooling data *e.g.* in Fig. 6.4 as will be shown in Chapter 6. The other parameters were fitted with  $\nu = 0.85$  fixed, and the parameters  $f_0 = 0.333(7)$ ,  $K_0 = 0.346(11)$  keV and  $f_\infty = 0.0444(16)$  was found give the best description of the data. For the transmission data in Fig. 5.11b it is noted that the minimum value of  $f_d$  occurs at approximately the same energy as the data measured using the  $3\gamma$  method.

With the purpose to measure the multi photon ionisation of Ps, a setup to measure  $f_d$  was recently installed in Aarhus with a PWO detector and a LabVIEW program to control the data acquisition provided by David Cassidy's group at UCL. The setup is very similar to that described above, but another oscilloscope is used and a couple of shared variables over the local network was set up to be able to control the laser delay from the data acquisition PC. The first measurement taken in Aarhus using SSPALS measures the delayed fraction  $f_d$  as a function of the positron implantation energy (see Fig. 5.12). The target used in this measurement has a non-structured bulk layer with a thickness of 30 nm on top of the carbon foil the reflect the Ps which is formed inside the meso-structured silica and diffuses towards the carbon foil. There is no indication in these data that this approach enhances the Ps formation fraction by facilitating a larger emission of the formed Ps, but a comparison between a film with and without this layer introduced is required to say anything definite.

The fits shown in Fig. 5.12 use Eq. 4.9 to give estimates of the diffusion of Ps to the film surface. Fig. 5.12a shows the delayed fraction at low positron implantation energy and as seen the fits are remarkably identical compared to what is seen in Fig. 5.9b for instance, where the  $3\gamma$  method was used. The fits in the range between 0.1 keV and 1.35 keV yield the fitting parameters  $f_0 = 0.1052(6)$ ,  $K_0 = 0.443(7)$  keV and  $f_\infty = 0.1020(5)$  for the (b) measurement and similar for the (a). The SSPALS method is in fact very stable, and the statistical errors in the measurements are very small. Since changes of the order of 1%



(a)



(b)

**Figure 5.12:** The delayed fraction  $f_d$  as a function of the positron implantation energy measured for a meso-structured silica sample with  $\theta = 7^\circ$ ,  $\phi = 6.0\text{rpm}$ , and  $\Delta t_\perp = 1370\text{nm}$  and a  $30\text{nm}$  layer of bulk silica on top of the carbon foil. Two independent measurements of the same target conducted at Aarhus University.

of the delayed fraction can be measured, it is a very useful tool for measuring laser induced changes in the Ps formation fraction.

In Fig. 5.12b, the total range (0 – 8 keV) of the measurements are shown, and another fit is performed to the (b) data from 1.35 keV up to 8 keV (orange). The fitted parameters to this fit are  $f_0 = 0.0488(3)$ ,  $K_0 = 3.82(9)\text{keV}$  and  $f_\infty = 0.0702(4)$ , which imply a long diffusion length in comparison to the other result. Thus the data seem to be composed of two (maybe even three, since  $f_d$  increases rapidly at low energies) components, which have different diffusion lengths, however, more investigations are needed before this can be

concludes definitively.

---

# Ps cooling in meso-structured silica

The cooling of Ps in the meso-structured silica samples is an important property of these samples. In the present chapter a Ps cooling experiment conducted at UCL in September 2014 is presented. The experiment uses Doppler spectroscopy and SSPALS to measure the mean energy of the Ps atoms emitted from the meso-structured silica sample by probing the Doppler broadened or shifted 1S-2P transition. The energy is measured in the longitudinal and transverse directions for both a reflection and transmission geometry. Furthermore, the optical access through the film is demonstrated, since the Ps longitudinal energy is probed by pointing a UV laser through the meso-structured silica sample.

## 6.1 Collisional cooling of Ps

The production of Ps emitted into vacuum at low energy is essential to a range of experiments and can be accomplished mainly via two processes. If the activation energy Eq. 4.2 is changed by changing the surface conditions (*i.e.* by changing the electron work function,  $\phi_-$ ) of a given metal or semiconductor, the thermal desorption of Ps at cryogenic temperatures is facilitated. Thus the mean Ps energy decreases linearly with the sample temperature, for instance for Ps emitted from oxidised Al [108], where  $\sim 12\%$  of the impinging positrons can be emitted as Ps at cryogenic temperatures.

Alternative to cryogenic Ps emission from contaminated metal surfaces, the Ps energy can be decreased by collisions with the wall of porous silica, the grains of silica powders, or the meso-structured silica samples used in the present work. A theoretical approach to the collisional cooling of Ps is

given in the present section, and a review of the subject can be found in [75].

### 6.1.1 Classical collisional cooling

When Ps is formed inside the pillars of the meso-structured silica films described in Chapter 3, it is emitted into the network of open spaces between the pillars at some initial energy,  $E_i$  (typically about 1–3 eV for silica [87]). As the Ps encounters a pillar wall it loses energy by collisions with atoms at the surface. If a description similar to that for cooling in porous silica [17] and silica powders [102] is assumed to apply for the meso-structured silica films, then the Ps energy loss can be described by a classical bouncing-of-the-walls picture if kinetic energy of the Ps is large. To be more specific, this is the case if the de Broglie wavelength is much smaller than the diameter of the confining cavity,  $d$ , and

$$E_{\text{Ps}} \gg \frac{2\pi^2\hbar^2}{m_{\text{Ps}}d^2} \simeq \left(\frac{1 \text{ nm}}{d}\right)^2 753 \text{ meV} \quad (6.1)$$

should be required. For the standard  $\Delta t_{\perp} = 1000 \text{ nm}$  sample, which is used for the Ps cooling measurements presented in the present chapter and [16], the column spacing was found to be  $\bar{L} \sim 160 \text{ nm}$  on average, and with column diameters  $D \sim 60 \text{ nm}$ . Thus the distance between the walls are on average  $\sim 100 \text{ nm}$ . The classical picture is expected to apply quite well for energies at least down to the thermal energy at cryogenic temperatures. Eventually, the classical description of energy loss in structured, silica-based materials is equivalent to the description of Ps collisions in a classical gas. Therefore, due to the finite thermal energy of the gas molecules or the molecules at the silica surface, the minimum Ps energy that can be achieved via collisional cooling in porous materials (including the meso-structured silica sample) equals the thermal energy of the silica,  $E_{\text{th}} = \frac{3}{2}kT$ . Thermal equilibrium is typically achieved after a short time compared with the mean lifetime of ortho-Ps. The classically predicted kinetic energy as a function of the time after Ps formation at the initial energy,  $E_i$ , is expected to hold for pores larger than  $\sim 6 \text{ nm}$  at room temperature [75].

The differential change of the energy per time is given in the classical model as the product of the energy dependent energy loss pr. collision and the mean collision rate [109], which can be estimated as  $\lambda_s = \nu_{\text{Ps}}/\bar{L}$ , where  $\nu_{\text{Ps}}$  is the mean Ps velocity. The spacing between the pillars is quite large compared with the typical mean free path for various types of porous silica, which results in a smaller collision rate and thus it takes a longer time for the Ps to thermalise or reach the minimum energy. Therefore it is necessary to implant the Ps deeper into the sample to facilitate a larger number of Ps collisions with the pillar walls on the way to the surface.

### 6.1.2 Confinement and quantum cooling

In the case of smaller pores or spaces between the pillars, where the Ps de Broglie wavelength is of the order of the pore size or the column spacing, a quantum description is necessary to account for the collisional cooling of Ps. This has been done in [110], where the authors have developed a model for Ps cooling in silica nanochannels directed perpendicular to the surface, and produced via etching of silicon and subsequent oxidation. The interaction between the Ps and the surface is described as a creation and destruction of phonons. If the Ps is described as a particle in a box of sides lengths  $a$ , then the ground state energy of the Ps is given by  $E = \pi^2 \hbar^2 / (m_{\text{Ps}} a^2)$ , which is the lowest attainable energy expected for the Ps atom. However, since the momentum transfer is quantised this energy has been shown to be elevated if the box is smaller than  $\sim 6$  nm. In the longitudinal direction of the nanochannels in [93, 111] the Ps energy is not limited since in that direction there is no confinement.

In some aspects the oxidised silicon nanochannels are similar to the meso-structured silica samples used in this work, since no confinement is expected in the longitudinal direction in either samples. However, the particle in a box picture does not quite apply in the two transverse dimensions for the  $\Delta t_{\perp} = 1000$  nm sample, because the Ps can move around in the open spaces similar to the motion in a gas, but in two dimensions only. On the other hand, as the column spacing becomes smaller and the pillars are more closely packed, which is the case for the films in Figs. 3.4c, 3.8c and 3.8d, the meso-structured thin films will act more and more like nanochannels. However, the advantage of these samples is that the very flexible nanosculpturing still applies, and a wide range of materials can be prepared with the same morphology. Thus, there is a vast parameter space to explore for future investigations.

For now we apply the effective model of [17] to the Ps cooling data presented in this chapter. In this model the cooling is considered classical, whereas the diffusion to the surface is quantum in nature and proceeds via tunnelling in the small pores of the porous silica used in the experiment in [17]. In comparison to the classical model of [112], this means that the minimum achievable energy  $E_{\text{min}}$  is not necessarily equal to the thermal energy, but may be set by the limit of quantum confinement. The mean energy change per collision is therefore assumed to take the form

$$\Delta E = -\alpha (E_{\text{Ps}} - E_{\text{min}}) , \quad (6.2)$$

where  $E_{\text{Ps}}$  is the total energy of the Ps atom and  $\alpha \sim 8 \cdot 10^{-5}$  is the fractional energy loss pr. interaction [113]. If  $N$  such interactions occur between the Ps atom and the  $\text{SiO}_2$  surface, then the mean energy decreases to

$$E_{\text{Ps}} = E_i \exp(-\alpha N) + E_{\text{min}} , \quad (6.3)$$

which can be converted into a positron implantation energy dependency by application of the mean implantation depth to estimate the number of collisions before emission into vacuum. This conversion does necessarily apply here, and some of the parameters only make sense in a porous silica like the one used in [17]. Therefore we only assume that  $N \propto K^{2\nu}$  to get

$$E_{\text{Ps}}(K) = E_i e^{-QK^{2\nu}} + E_{\text{min}} , \quad (6.4)$$

where  $Q$  is an effective cooling rate. Eq. 6.4 is the expression that will be used in the following to describe the Ps cooling measurements, however, as will be discussed later the minimum achievable energy is not assigned to confinement of Ps or the complete thermalisation but stems from the finite thickness of the film used in the experiment.

## 6.2 Experimental setup

The positrons utilised in the Ps cooling experiment stem from the trap based beam line at UCL. This beamline is very similar to the one at Aarhus University, and only a short overview is given here. The positrons emitted by the  $^{22}\text{Na}$  source are moderated by a solid neon moderator, and guided magnetically to a two-stage Surko trap. The trap uses  $\text{N}_2$  as buffer gas and  $\text{CF}_4$  as cooling gas and the rotating wall compresses the positron bunch ( $\sim 5 \cdot 10^5$  positrons per bunch), which is released from the trap by applying a linear electric potential along the beam axis to obtain a 4 ns FWHM pulse at the sample. The positron pulses are implanted into the meso-structured silica sample ( $\Delta t_{\perp} = 1000 \text{ nm}$ ,  $\theta = 7^\circ$  and  $\phi = 6.0 \text{ rpm}$ ) at a frequency of 1 Hz, and the energy is set by applying a negative potential to the target holder. In the present experiment there is no grid in front of the sample, which is mounted on a 3-dimensional manipulator with rotation around the z-axis for easy alignment and switching between the transmission and reflection geometries. The energy gain from the linear potential applied to the trap is about 100 eV, and the FWHM of the positron energy distribution is about 50 eV.

The Ps formation is measured using SSPALS, which was described in Section 4.4, and three normalised lifetime spectra are shown in Fig. 4.7 to reveal the Ps formation fraction. Relative changes  $\sim 1\%$  of the delayed fraction can be measured via SSPALS, and the change of  $f_d$  due to laser ionisation of Ps can be probed effectively. As described in Chapter 4, the  $\gamma$ -ray signal stemming from positron and positronium annihilations in the target region is measured by a  $\text{PbWO}_4$  crystal and a fast PMT, and digitised in a fast oscilloscope after being split in a  $50 \Omega$  tee. The  $\text{PbWO}_4$  detector was pointing perpendicular towards the beam axis in front of (behind) the meso-structured silica sample in the reflection geometry (transmission geometry) so that the

solid angle for the detection of Ps is always maximised. A 1 GHz, 2.5 GS/s, 12-bit oscilloscope (Teledyne Lecroy HDO 4104) ensures a very precise, low noise reproduction of the voltage signal, and the signals from typically 100 – 200 positron pulses were analysed live in a LabVIEW program to extract  $f_d$ , and the final off-line analysis was carried out using ROOT<sup>11</sup>.

The 1S-2P transition in Ps is driven by a wavelength tunable UV laser (centred at 243 nm) and the excited atoms are subsequently photoionised by photon absorption at 532 nm. Since the Ps atoms are travelling either towards or away from the UV laser, the 1S-2P transition will be Doppler shifted and/or broadened. The Doppler shift or broadening depends upon the Ps velocity with respect to the laser and a measurement of the delayed fraction  $f_d$  using SSPALS as a function of the UV wavelength reveals the mean energy of the Ps in a given direction.

The laser setup used for these measurements<sup>12</sup> is shown in Fig. 6.1. The fundamental frequency of the Nd:YAG laser (Continuum, Surelite II-10,  $\lambda = 1064$  nm) was tripled in a harmonic generator (HG) and separated from the fundamental frequency in a harmonic separator (HS) to yield a 7 ns duration pulse at 355 nm and with an energy up to 150 mJ per pulse. This radiation was used to pump the dye laser (Sirah, Cobra Stretch) and produce a tunable pulse of wavelength between 460 nm and 490 nm, which was frequency-doubled in a Beta Barium Borate (BBO) crystal to produce a  $\sim 7$  ns pulse of energy up to 5 mJ at the Lyman- $\alpha$  wavelength of Ps,  $\lambda_0 \approx 243$  nm. The phase-matching angle of the BBO crystal was adjusted to maintain a constant energy of the pulse as the wavelength was changed. In practice the pulse energy was reduced to  $\sim 1.3$  mJ ( $\sim 400$   $\mu$ J) by collimation before entering the interaction vacuum chamber when probing the Ps transverse (longitudinal) energy. The bandwidth of the 243 nm radiation is estimated to be  $\sim 85$  GHz.

When the Ps atom has been excited to the 2P state it is photoionised by the 532 nm,  $\sim 7$  ns pulse produced as the second harmonic of the Nd:YAG laser with a pulse energy controlled by a neutral density (ND) filter to be  $\sim 20$  mJ. The relative timing of the UV pulse and the 532 nm pulse is controlled by adjusting the delay path of the green laser. The delay of the Nd:YAG Q-switch, which controls the overall timing of the lasers is synchronised to the trap extraction so the repetition rate of the lasers is also 1 Hz. However, a final adjustment of the laser delays is done for each specific sample, since the emission of Ps from a given sample may be significantly delayed with respect to the positron implantation time. The green laser enters the interaction region at an angle of  $\sim 5^\circ$  to the horizontal plane, and crosses the horizontal UV

<sup>11</sup>C++ framework developed at CERN (<https://root.cern.ch/>).

<sup>12</sup>The laser setup was ready for the experiment when I arrived at UCL with the silica sample.

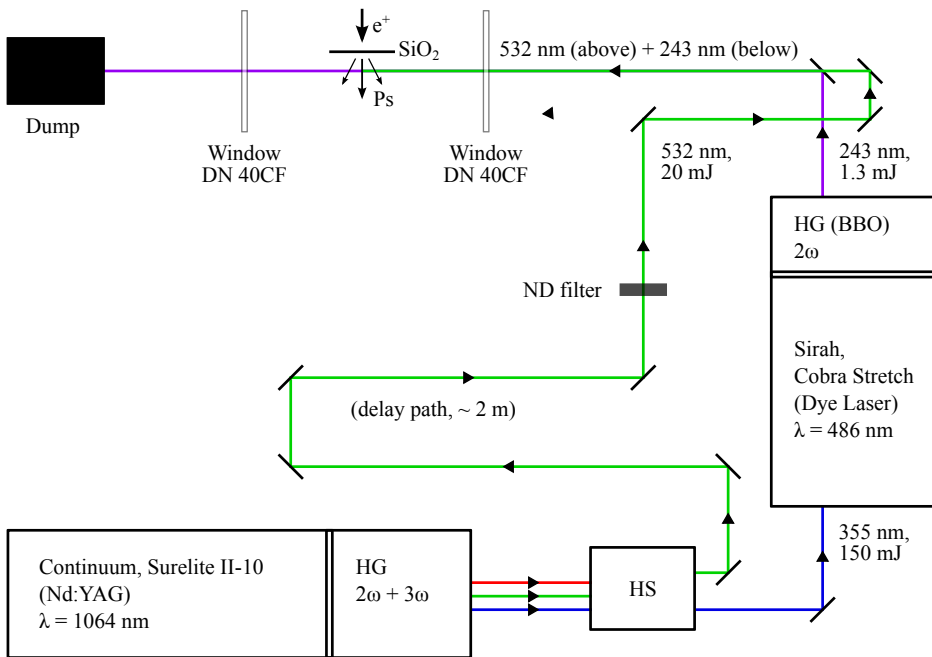


**Figure 6.1:** Overview of the experimental setup used to measure the cooling of Ps in the meso-structured silica film. The UV and green laser pulses overlap with the Ps cloud both in space and time, and the two-photon resonance enhanced ionisation is measured using SSPALS. See the text for a detailed description. Modified from original drawing by Adam Deller.

beam in front of (behind) the structured silica sample when Ps is formed in reflection (transmission), and the two laser beams are aligned to the Ps cloud by blocking of 50% of each beam in front of or behind the sample in reflection and transmission geometries, respectively.

The geometries used in these measurements are defined in Fig. 6.2, where four possibilities are shown. If the meso-structured silica sample is in the reflection geometries then both lasers are directed along the surface to measure the Doppler broadening of the Lyman- $\alpha$  transition and reveal the transverse energy. To measure the longitudinal energy on the other hand, the UV laser is transmitted through the sample, and the Doppler shift is seen. Similarly, when the sample is in the transmission geometry, the transverse energy is probed by both lasers pointing along the surface, whereas the longitudinal energy has the UV laser directed onto the surface. It turns out that the reflected laser beam also interacts with the Ps atoms and a double peak structure appears from the counter propagating laser beam interaction with the Ps atoms for the longitudinal energy measurement in transmission geometry.

All data in the following has been easily acquired by setting up measure-

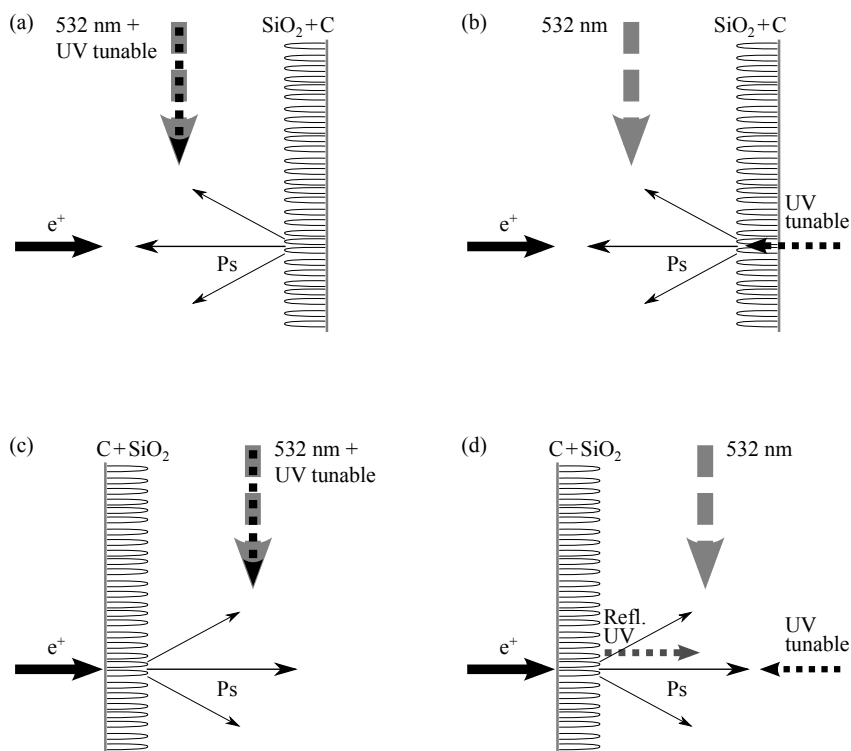


**Figure 6.2:** The four geometries in which the Ps energy is measured. Ps is formed in reflection (a) and (b) and in transmission in (c) and (d). The energy of Ps is measured in the transverse direction in (a) and (c), where both lasers are directed along the sample surface. The longitudinal energy of Ps is probed in (b) and (d), where the UV laser is pointed along the positron beam axis, while the green laser is still directed along the surface of the sample.

ment sequences in the LabVIEW project which also controls the timing of the hardware and the data acquisition by the oscilloscope. This LabVIEW project is very similar to the one that Adam Deller made for the Aarhus setup.

### 6.3 Ps cooling in reflection from meso-structured silica

If the meso-structured silica sample is positioned in the reflection geometry as defined in Fig. 6.2 then the Makhovian implantation profile applies up to some energy, where the positrons start to implant the supporting carbon foil and eventually are transmitted through the sample. Therefore the initial state of the diffusion process changes and the fraction of Ps is modified compared to a infinitely thick sample. Measurements of the transverse and longitudinal energy of the emitted Ps formed in the reflection geometry are presented in

the following.

In order to obtain a good overlap in time between the lasers and the Ps atoms emitted from the meso-structured silica sample, it is necessary to make a scan of the trap delay times with respect to the laser delay and maximise the ionisation probability. The arrival time of the positrons is known from simultaneous measurement of the annihilation  $\gamma$ -rays and the laser beams in a plastic scintillator, as was done in [17], and the positrons are expected to arrive at the same time as the laser pulses if the trap delay is set to  $t_{e^+} = 289.3$  ns. If the wavelength of the UV laser is set to the expected resonance value,  $\lambda_0 \approx 243$  nm then the delay scan yields a typical maximum ionisation probability at the trap delay time  $t_{\text{trap,delay}} \sim 285$  ns ( $t_{\text{trap,delay}} \sim 280$  ns) if the lasers are directed such that the transverse (longitudinal) energy component is measured. The difference between the delays for the two laser configurations may occur because the delay path of the green laser was optimised for the transverse configuration, and may not apply when the laser beams are crossed at right angles, since a small change in the path length could have occurred.

The emission of the Ps occurs almost instantaneously as the positrons implant the meso-structured silica sample. This is in contrast to the delayed emission observed in other porous silica samples [92], where the emission occurs about 25–30 ns after positron implantation. This behaviour is attributed to the very open structure of the meso-structured silica samples used in this work, and it supports the expectations, that no confinement should occur in the silica film.

To quantify the ionisation of Ps via the two-step process, where the Ps excited by the UV laser is ionised by the green laser, the relative change in the delayed fraction is defined as

$$S = \frac{f_b - f_d}{f_b}, \quad (6.5)$$

where  $f_b$  is the background delayed fraction measured when the UV laser is off-resonance and  $f_d$  is the delayed fraction for a given set of parameters (positron implantation energy ( $K$ ), trap delay ( $t_{\text{trap,delay}}$ ) or laser wavelength ( $\lambda$ )). To measure the Doppler broadened 1S-2P transition using SSPALS, a scan of UV laser wavelengths is performed in the range between 242.3 nm and 243.75 nm and single-shot spectra are measured for each wavelength. From these spectra the delayed fraction  $f_d$  is found and seen to decrease when the UV laser becomes resonant with the 1S-2P transition. This decrease occurs because the fraction of Ps present in front of the sample decreases shortly after the emission from the meso-structured silica film as a result of ionisation of Ps. The lasers are positioned quite close (0.5–1.0 mm) to the silica sample, and the positrons stemming from the ionisation events are re-impinging

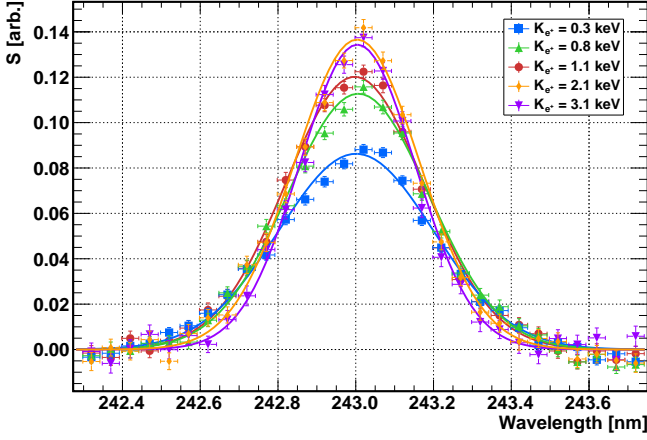


**Figure 6.3:** The relative change  $S$  in the delayed fraction  $f_d$  as a function of the UV laser wavelength  $\lambda$  increases around the Lyman- $\alpha$  transition wavelength and reveals the Doppler broadened resonance for five positron impact energies. The solid lines are Gaussian fits.

upon the silica sample, which is negatively biased to accelerate the positrons onto the sample in the first place. From the value of  $f_d$  at each wavelength,  $S$  can be calculated using Eq. 6.5, where the off-resonance measurement is taken as the average of points far from the resonance wavelength. The Doppler spectra are shown for five different positron implantation energies in Fig. 6.3, and a Gaussian is fitted to each data set (the solid lines in Fig. 6.3). The Doppler widths of the data is extracted from the fits, and the mean squared velocity,  $\langle v_x^2 \rangle$ , of the emitted Ps can be found from

$$\frac{\sigma}{\lambda_0} = \sqrt{\frac{\langle v_x^2 \rangle}{c^2}}, \quad (6.6)$$

where  $\sigma$  is the standard deviation of the Gaussian fits found from each Doppler resonance,  $\lambda_0 = 243 \text{ nm}$  is the Lyman- $\alpha$  resonance wavelength and  $c$  is the speed of light.

The transverse energy of the Ps emitted from the meso-structured silica film is calculated from the classical expression

$$E_{x,\text{Ps}} = \frac{1}{2} m_{\text{Ps}} \langle v_x^2 \rangle, \quad (6.7)$$

where  $m_{\text{Ps}}$  is the mass of Ps. The transverse energy of the emitted Ps can then be plotted as a function of the positron implantation energy as shown in Fig. 6.4, and the transverse Ps energy is clearly seen to decrease with the positron energy, *i.e.* the Ps atoms formed at increasing depth inside the meso-structured silica is cooled down by an increasing number of collisions with

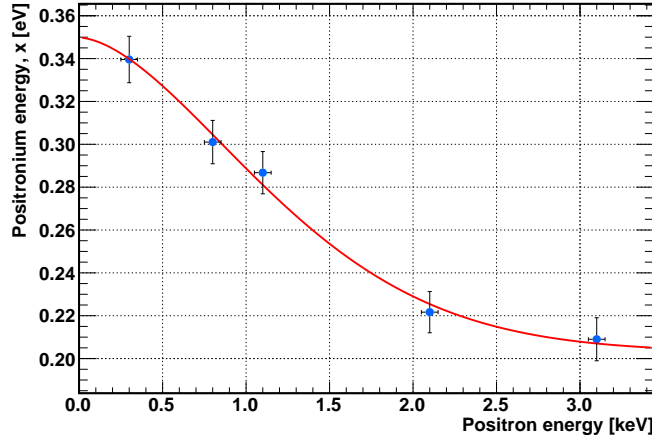


**Figure 6.4:** The transverse energy of the Ps emitted in the reflection geometry from meso-structured silica is plotted as a function of positron implantation energy. The fit is an estimate of the data based on Eq. 6.4.

the pillar walls on the way to the surface. It is noted also that the amplitude of the Doppler profiles is increasing with the positron implantation energy. This is also expected when the energy of the Ps decreases, since the interaction time with the laser will then increase.

The data in Fig. 6.4 is fitted by Eq. 6.4, but the usual value of the parameter  $\nu = 1.7$  is not used here. Instead  $\nu$  is fixed to the value found from the fit to Eq. 4.9 of the data in Fig. 5.11a,  $\nu = 0.844$ , and an effective description of the data is given. With this value fixed, the other parameters found from the fit are; the initial energy,  $E_i = 0.147(14)$  eV, the effective cooling rate,  $Q = 0.54(16)$  eV $^{-2\nu}$ , which is related to the number of Ps-pillar collisions, and the minimum achievable energy,  $E_{\min} = 0.203(12)$  eV.

As mentioned earlier, the latter parameter is usually related to the confinement of Ps in small pores. However that is not the case here since the open spaces are simply too large for confinement to occur and the Ps would thermalise before reaching energies where the de Broglie wavelength is comparable to the distance between the pore walls. The large open spaces also imply a slower decrease in the Ps energy compared to porous silica with smaller pores since the mean free path is long and fewer Ps-pillar collisions occur. In fact, the thickness of the films is what limits the cooling of Ps in this particular sample, since when the positrons have reached the carbon foil no further cooling is possible.

The Ps energy is also measured in the longitudinal direction (Fig. 6.2b) by transmitting the UV laser through a structured silica sample to probe the Doppler shifted Lyman- $\alpha$  resonance of Ps in the longitudinal direction. The

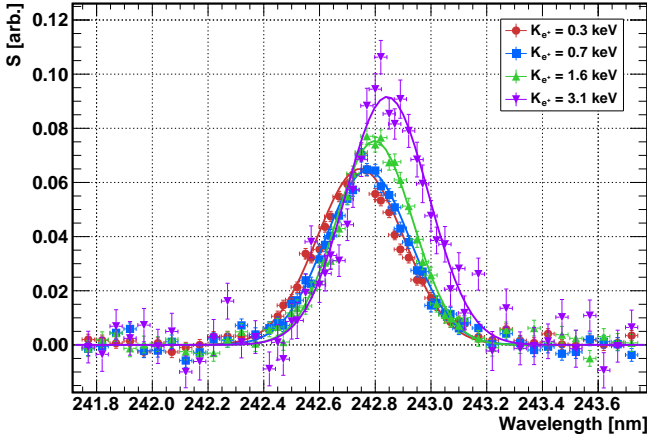


**Figure 6.5:** The Doppler shifted resonance shapes for Ps formed in reflection is used to find the longitudinal energy component at four different positron implantation energies. The amplitude of the profiles are larger when the laser-Ps interaction time is longer *i.e.* when the transverse Ps energy is lower. The solid lines are Gaussian fits.

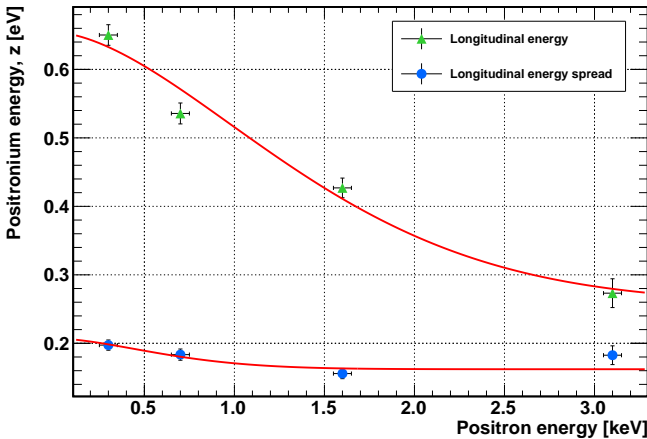


**Figure 6.6:** The longitudinal Ps energy and energy spread are plotted as a function of positron implantation energy. The fits are estimates of the data based on Eq. 6.4.

Ps is then moving away from the laser source and the resonance will be blue shifted. The data for these measurements are shown in Fig. 6.5, and the resonance shapes are fitted to a Gaussian function. The Doppler shifts (the mean values of the Gaussian fits) are used to calculate the Ps longitudinal energy from Eqs. 6.6 and 6.7. The resulting longitudinal energy is seen in Fig. 6.6, as a function of the positron implantation energy. Also plotted in Fig. 6.6 is the energy spread of the emitted Ps in the longitudinal direction, which has been found from the standard deviations of the Doppler shifted profiles.

The longitudinal Ps energy dependency on the positron implantation energy has been fitted to Eq. 4.9 just as in the case of the transverse energy of Ps. The parameters found from the fit in Fig. 6.6 are:  $E_i = 0.40(3)$  eV,  $Q = 0.43(10)$  keV $^{-2\nu}$  and  $E_{\min} = 0.26(3)$  eV. Both the initial energy and the minimum achievable energy are larger in the longitudinal direction than in the transverse direction, but the cooling ‘rate’ is the same within errors for the two energy components. The energy spread in the longitudinal direction is below 200 meV at all positron implantation energies. Also, there is possibly some narrowing of the width of the blue shifted Doppler profiles, which would mean that the Ps atoms are emitted at a more well defined energy as they are formed deeper inside the sample and experience more collisions on their way to the surface of the meso-structured silica films.

There is clear evidence for the ability of this meso-structured silica sample to cool down the Ps via collisional cooling. The effective model used to describe the decrease in the longitudinal and transverse components of the Ps energy in reflection fit the data quite well and give an estimate of the minimum achievable energy,  $E_{\min}$ . The minimum energy is reached when the positrons are implanted deep enough into the sample that some of the positrons start to impinge upon the carbon foil that support the silica film. According to Fig. 4.5a the positrons start to enter the carbon foil at a positron implantation energy of about 2–2.5 keV, which is approximately the positron implantation energy at which the Ps energy start to become constant. If the thickness of the meso-structured silica films is about 800 nm thick, then the positrons are expected to reach the carbon foil on average at an implantation energy of  $\sim 4.2$  keV at which the minimum Ps energy has also been achieved.

If a smaller Ps energy is required (which it typically would be) there are two possibilities. One is to make a thicker silica film, which can easily be achieved by depositing silica at the same glancing angle for a longer time. The second possibility is to deposit the silica at a larger glancing angle to increase the density of the meso-structured silica films. This was done for the samples in Figs. 3.4b or 3.4c and with no sample rotation for the film shown in Figs. 3.8c and 3.8d. Future work to do thus includes a measurement of the Ps formation and cooling in samples grown with these modified parameters, and indeed there is a huge parameter space to explore in order to fully optimise these samples for Ps formation and cooling.

## 6.4 Ps cooling in transmission from meso-structured silica

The meso-structured silica sample is now positioned in the transmission geometry for Ps production and cooling. The Ps formation in transmission was

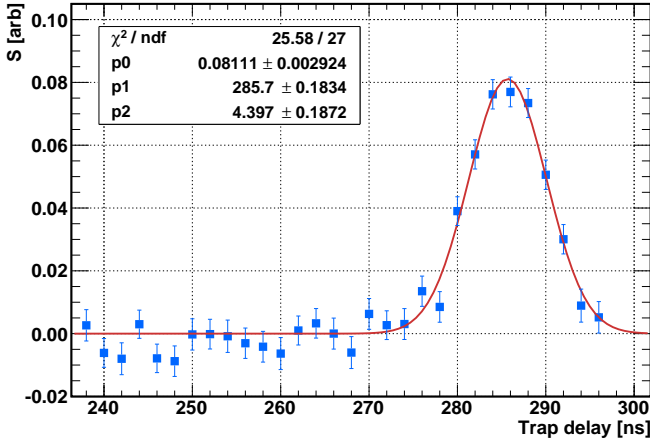


**Figure 6.7:** Delay scan in the transmission geometry. The positron implantation energy is 1.3 eV and the emission time is the same as that found in the reflection geometry when the lasers were directed along the silica surface.

measured in terms of the delayed fraction,  $f_d$  as a function of the positron implantation energy and was shown in Fig. 5.11b, where a significant amount of Ps formed in transmission was seen to occur for positron energies above  $\sim 1$  eV. In this section the transverse and longitudinal energy components of Ps formed in transmission are measured using Doppler spectroscopy and a laser setup identical to that of the previous section, but with the structured silica sample in the transmission geometry as seen in Fig. 6.2c and 6.2d.

When the positron implantation energy is increased and the positrons start to be transmitted through the carbon foil the formation of Ps in transmission is initiated as discussed in Chapter 4. As long as the positron energy is kept fairly low all the emitted Ps will form deep inside the silica sample with respect to the transmission surface, and a large fraction of the Ps atoms will experience the maximum collisional cooling from Ps-pillar collisions. If there were any delay in the emission of Ps it would certainly appear in a delay scan of the trap delay to the laser, when the Ps is formed in transmission. A delay scan to adjust the laser delay to the Ps emission is seen in Fig. 6.7, for Ps formed in the transmission geometry. The peak position is found from a Gaussian fit to give an optimal trap delay time of 285.70(18) ns and the signal height is  $\sim 8\%$  of the off-resonance measurement. The important thing to notice about the delay scan is that the result is the same within errors for the reflection and transmission geometries, when both lasers are directed parallel to the sample surface. In fact, if the UV laser is pointing perpendicular to the sample surface the same result is also obtained for the reflection and transmission geometries, which is, however different from the result in Fig. 6.7.

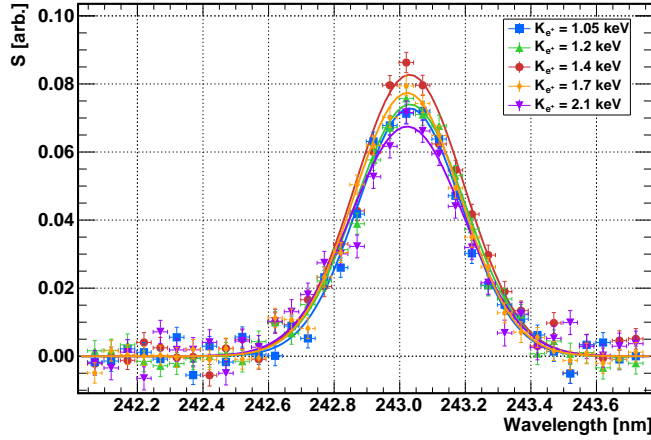


**Figure 6.8:** Doppler broadened resonance shapes for the Lyman- $\alpha$  transition for Ps formed in transmission. The solid lines represent Gaussian fits that are used to extract the transverse Ps energy.

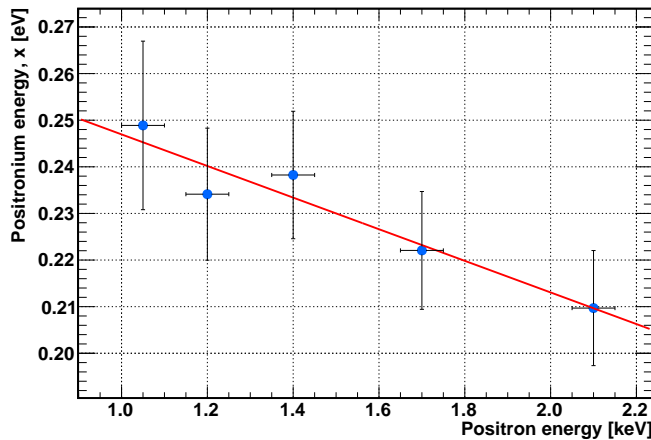


**Figure 6.9:** The transmission-formed Ps transverse energy plotted as a function of positron implantation energy. The red line represents a linear fit of the data to guide the eye.

Therefore the error seems to be systematic and thus may be due to a mismatch between the relative timing of the lasers, which would also explain the notoriously smaller signal when probing the longitudinal energy component.

The Doppler profiles for 1S-2P transition probed transverse to the sample surface is seen in Fig. 6.8. Each resonance profile is fitted to a Gaussian function, and the energy is extracted as in the reflection geometry using Eqs. 6.6 and 6.7. The Ps transverse energy component is shown in Fig. 6.8 as a function of positron implantation energy in the transmission geometry. The

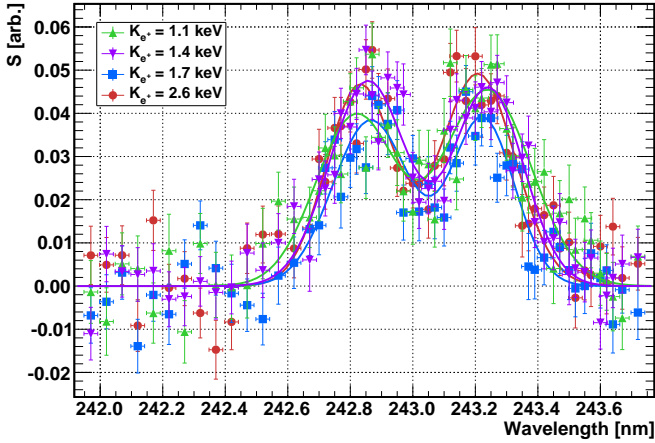


**Figure 6.10:** The double peak structure of these Doppler profiles are due to the reflection of  $\sim 90\%$  of the UV laser, when probing the longitudinal Ps energy. Thus both a blue shift and a red shift is seen.

lowest transverse Ps energy is obtained at the highest implantation energy (2.1 keV) and is 0.210(12) eV, and the Ps energy is seen to decrease slightly as the positron implantation energy is increased within the range of energies used here. The Ps is formed relatively deep inside the meso-structured silica film for all the positron implantation energies, which is why the Ps transverse energy does not increase as the positron energy is increased (the positron implantation energy is not large enough to see this effect). The reason why the Ps energy apparently goes down with the positron energy may be that some Ps is formed in the carbon foil and diffused from there to the transmission surface. The Ps formed in the carbon foil may have a higher energy and therefore the mean energy measured will be higher than expected for the lowest positron implantation energies.

The longitudinal energy of the Ps formed in transmission was also probed. The situation here (see Fig. 6.2d) is again slightly different from the other measurements, since the UV laser is not only passing through the sample. Actually  $\sim 90\%$  of the light is reflected back towards the laser source and a double peak structure is seen in the measurements in Fig. 6.10. The right peak stems from the red shifted Doppler profile occurring because the Ps atoms are traveling towards the laser source, whereas the left peak stems from interaction of the Ps atoms with the reflected laser, where a blue shift occurs because Ps is traveling away from the reflected laser beam. The peak centroid positions and the widths of the two resonances can be found from a double Gaussian fit of the data in Fig. 6.10. The results are slightly asymmetric since the central dip has been shifted with respect to the Lyman- $\alpha$  resonance

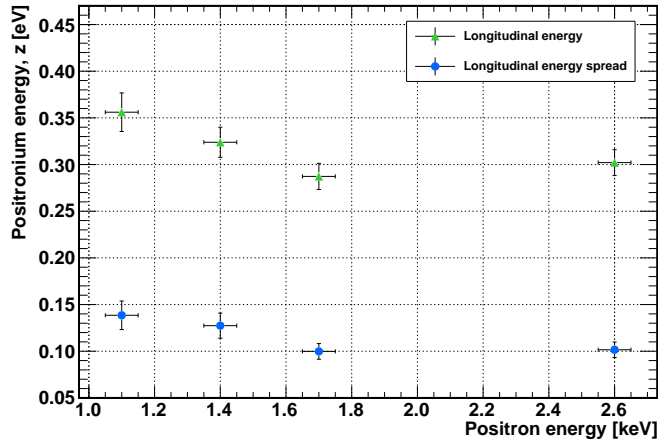


**Figure 6.11:** The longitudinal component of the Ps energy and energy spread as extracted from the Doppler shifted double peak resonance structures, and plotted as a function of positron implantation energy.

wavelength. A shift which presumably occurs because of a misalignment of the laser with respect to the surface of the silica sample as was also observed elsewhere [85].

The longitudinal Ps energy is now found by setting  $\sigma$  in Eq. 6.6 equal to half of the separation of two peaks, and the misalignment of the laser with respect to the surface is automatically taken into account. The widths of the peaks are also combined to estimate the longitudinal spread in energy of the Ps emitted from the meso-structured silica sample. The Ps formation energy and energy spread is shown in Fig. 6.11 as a function of the positron implantation energy. It is noted that the correlation between the fitted centroid positions and standard deviations were taken into account when the errors were calculated. The tendency of the data in Fig. 6.11 is similar to what was seen for the transverse Ps energy. The longitudinal Ps energy decreases up to a positron implantation energy of at least 1.7 keV, where the minimum longitudinal energy is found to be 0.287(14) eV. However, there is an indication that the longitudinal Ps energy is increased as the positron implantation energy increases beyond  $\sim 2$  keV, which would be expected from positrons being stopped closer to the transmission surface. The spread in the longitudinal Ps energy is seen to be very small, which indicates that the emitted Ps atoms experience the same amount of cooling on the way to the surface of the meso-structured silica film.

The minimum energy obtained in the transmission geometry is seen to agree within errors with the minimum energy found in the reflection geometry, both for the transverse and the longitudinal energies. This also supports the idea that the minimum Ps energy that can be achieved by collisional cool-

ing in the meso-structured silica films is obtained when the positrons are stopped closer to the carbon foil. A thicker silica film with a thinner carbon foil for support is therefore required to increase the Ps cooling, presumably until a thermal emission has been obtained.



---

## Conclusions and outlook

The main purpose of the present work has been to characterise the meso-structured silica films in terms of Ps formation and cooling. The novelty of these samples lie in the ability to form and cool Ps in the transmission geometry, but also that the sample allows for optical access along the positron beam axis.

Before being able to form Ps it is necessary to create low energy positron. Therefore the positron beamline was first described, and characterised. The trap has been optimised to output pulses consisting of about  $5 \cdot 10^5$  positrons arriving at the interaction regions within a time of  $\sim 8$  ns, and with a FWHM diameter of about 2.5 mm. The energy spread of the positrons is also very narrow, and simulations show that the buncher only increases the energy spread slightly in the current configuration.

The meso-structured silica films were analysed and the pillars were found to be spaced by about 160 nm, having a diameter of about 60 nm. If no rotation is applied and the glancing angle of deposition is set to be  $\theta = 12^\circ$ , then a denser film with smaller pillars and smaller spaces inbetween is grown. This film is expected to be better for Ps formation and cooling.

The Ps formation fraction was measured for several samples and using both the  $3\gamma$ -method and SSPALS. If the sample thickness is taken into account when analysing the data, then some limits to where the fit applies can be set. With these limits, the theory describe the data quite well. When Ps is formed in transmission, the carbon foil thickness should be very thin to form as much Ps as possible. The maximum achievable Ps formation fraction is  $\sim 50\%$  at low positron implantation energy in the reflection geometry, but the formation fraction falls of quite fast initially and reaches a level  $\sim 20\%$  at 2 keV. In the transmission geometry, the maximum yield is  $\sim 10\%$ .

The Doppler spectroscopy measurements show that the energy of Ps is decreasing with the positron implantation energy, and the until a limit has

been reached. This limit is attributed to the positrons having reached the bottom of the sample, and thus the Ps cannot cool more. However, there is an easy solution, namely to make a thicker or denser silica film. The minimum achievable energy is the same within error for the longitudinal and transverse energies in reflection and transmission geometries, respectively. The minimum longitudinal energy of Ps is thus  $\sim 0.27$  eV, whereas the minimum transverse Ps energy is  $\sim 0.21$  eV.

Quite some work was done to try to measure the multi photon ionisation of Ps. The status is now that the positron beamline is not working. However, the experiment has been setup and aligned and timed, so it should be easy to continue the work to scan over the laser delays and the focal point of the laser beam, once the positrons return. Other than that, there are several optimisations to do regarding sample optimisation to obtain the best parameters of the meso-structured silica to form and cool Ps in transmission.

---

# Bibliography

- [1] P. A. M. Dirac, “Quantised singularities in the electromagnetic field,” *Proceedings of the Royal Society of London. Series A*, vol. 133, no. 821, pp. 60–72, 1931.
- [2] C. D. Anderson, “The positive electron,” *Phys. Rev.*, vol. 43, pp. 491–494, 1933.
- [3] N. Guessoum, R. Ramaty, and R. E. Lingenfelter, “Positron annihilation in the interstellar medium,” *ApJ*, vol. 378, pp. 170–180, 1991.
- [4] G. Gabrielse, S. Rolston, L. Haarsma, and W. Kells, “Antihydrogen production using trapped plasmas,” *Physics Letters A*, vol. 129, no. 1, pp. 38–42, 1988.
- [5] M. Charlton and J. W. Humberston. Cambridge University Press, Cambridge, 2001.
- [6] D. W. Gidley, H.-G. Peng, and R. S. Vallery, “Positron annihilation as a method to characterize porous materials,” *Annual Review of Materials Research*, vol. 36, no. 1, pp. 49–79, 2006.
- [7] R. J. Hicks, “Principles and practice of positron emission tomography,” vol. 45, no. 11, pp. 1973–1974, 2004.
- [8] S. J. Brawley, A. I. Williams, M. Shipman, and G. Laricchia, “Resonant scattering of positronium in collision with CO<sub>2</sub>,” *Phys. Rev. Lett.*, vol. 105, p. 263401, 2010.
- [9] M. Charlton, “Antihydrogen production in collisions of antiprotons with excited states of positronium,” *Phys. Lett. A*, vol. 143, no. 3, pp. 143–146, 1990.

- [10] A. M. Jr. and M. Leventhal, “Can we measure the gravitational free fall of cold rydberg state positronium?,” *Nuclear Instruments and Methods in Physics Research Section B: Beam Interactions with Materials and Atoms*, vol. 192, no. 1–2, pp. 102 – 106, 2002.
- [11] D. B. Cassidy and S. D. Hogan, “Atom control and gravity measurements using rydberg positronium,” *International Journal of Modern Physics: Conference Series*, vol. 30, p. 1460259, 2014.
- [12] P. M. Platzman and A. P. Mills, “Possibilities for bose condensation of positronium,” *Phys. Rev. B*, vol. 49, pp. 454–458, 1994.
- [13] S. G. Karshenboim, “Precision study of positronium: testing bound state QED theory,” *Intl. Jour. of Mod. Phys. A*, vol. 19, pp. 3879–3896, 2003.
- [14] D. B. Cassidy and A. P. Mills, “The production of molecular positronium,” *Nature*, vol. 449, pp. 195–197, 09 2007.
- [15] S. L. Andersen, R. R. Johansen, J. B. Overgaard, J. K. Mortensen, K. K. Andersen, H. D. Thomsen, M. D. Lund, J. Chevallier, H. Knudsen, and U. I. Uggerhøj, “Positronium formation from porous silica in backscattering and transmission geometries,” *The European Physical Journal D*, vol. 68, no. 5, p. 124, 2014.
- [16] S. L. Andersen, D. B. Cassidy, J. Chevallier, B. S. Cooper, A. Deller, T. E. Wall, and U. I. Uggerhøj, “Positronium emission and cooling in reflection and transmission from thin meso-structured silica films,” *submitted to Micropor. Mesopor. Mat.*, 2015.
- [17] D. B. Cassidy, P. Crivelli, T. H. Hisakado, L. Liskay, V. E. Meligne, P. Perez, H. W. K. Tom, and A. P. Mills, “Positronium cooling in porous silica measured via Doppler spectroscopy,” *Phys. Rev. A*, vol. 81, p. 012715, 2010.
- [18] A. Rich, “Recent experimental advances in positronium research,” *Rev. Mod. Phys.*, vol. 53, pp. 127–165, 1981.
- [19] B. A. Kniehl, A. V. Kotikov, and O. L. Veretin, “Orthopositronium Lifetime: Analytic Results in  $\mathcal{O}(\alpha)$  and  $\mathcal{O}(\alpha^3 \ln \alpha)$ ,” *Phys. Rev. Lett.*, vol. 101, p. 193401, 2008.
- [20] “ASACUSA.” <http://asacusa.web.cern.ch/>.
- [21] “First Point Scientific Inc..” <http://www.firstpsi.com/>.

- [22] R. Greaves and J. Moxom, "Design and performance of a trap-based positron beam source," in *Non-Neutral Plasma Physics V: Workshop on Non-Neutral Plasmas*, vol. 692, pp. 140–148, AIP Publishing, 2003.
- [23] P. J. Schultz and K. G. Lynn, "Interaction of positron beams with surfaces, thin films, and interfaces," *Rev. Mod. Phys.*, vol. 60, pp. 701–779, 1988.
- [24] P. Coleman, *The generation and transport of positron beams*. World Scientific, 2000.
- [25] A. P. Mills Jr. and E. M. Gullikson, "Solid neon moderator for producing slow positrons," *Appl. Phys. Lett.*, vol. 49, pp. 1121–1123, 1986.
- [26] E. M. Gullikson and A. P. Mills Jr., "Positron dynamics in rare-gas solids," *Phys. Rev. Lett.*, vol. 57, pp. 376–379, 1986.
- [27] M. P. Petkov, K. G. Lynn, and L. O. Roellig, "Water-induced effects on the positron moderation efficiency of rare gas solids," *J. Phys.: Condens. Matter*, vol. 8, p. 1611, 1996.
- [28] R. Khatri, M. Charlton, P. Sferlazzo, K. G. Lynn, A. P. Mills Jr., and L. O. Roellig, "Improvement of rare-gas solid moderators by using conical geometry," *Appl. Phys. Lett.*, vol. 57, pp. 2374–2376, 1990.
- [29] G. R. Brandes and A. P. Mills, "Work function and affinity changes associated with the structure of hydrogen-terminated diamond (100) surfaces," *Phys. Rev. B*, vol. 58, pp. 4952–4962, 1998.
- [30] C. M. Surko, M. Leventhal, and A. Passner, "Positron plasma in the laboratory," *Phys. Rev. Lett.*, vol. 62, pp. 901–904, 1989.
- [31] C. M. Surko, *Accumulation, storage and manipulation of large numbers of positrons in traps I.-The basics*. IOS Press, Amsterdam and SIF, Bologna, 2010.
- [32] J. P. Marler and C. M. Surko, "Positron-impact ionization, positronium formation, and electronic excitation cross sections for diatomic molecules," *Phys. Rev. A*, vol. 72, p. 062713, 2005.
- [33] T. J. Murphy and C. M. Surko, "Positron trapping in an electrostatic well by inelastic collisions with nitrogen molecules," *Phys. Rev. A*, vol. 46, pp. 5696–5705, 1992.
- [34] R. G. Greaves and C. M. Surko, "Positron trapping and the creation of high-quality trap-based positron beams," *Nucl. Instr. and Meth. B*, vol. 192, pp. 90–96, 2002.

- [35] J. P. Marler and C. M. Surko, “Systematic comparison of positron- and electron-impact excitation of the  $\nu_3$  vibrational mode of  $\text{CF}_4$ ,” *Phys. Rev. A*, vol. 72, p. 062702, 2005.
- [36] F. Anderegg, E. M. Hollmann, and C. F. Driscoll, “Rotating field confinement of pure electron plasmas using trivelpiece-gould modes,” *Phys. Rev. Lett.*, vol. 81, pp. 4875–4878, 1998.
- [37] R. G. Greaves and C. M. Surko, “Inward transport and compression of a positron plasma by a rotating electric field,” *Phys. Rev. Lett.*, vol. 85, pp. 1883–1886, 2000.
- [38] R. G. Greaves and C. M. Surko, “Radial compression and inward transport of positron plasmas using a rotating electric field,” *Physics of Plasmas*, vol. 8, no. 5, pp. 1879–1885, 2001.
- [39] R. G. Greaves and J. M. Moxom, “Compression of trapped positrons in a single particle regime by a rotating electric field,” *Physics of Plasmas*, vol. 15, p. 072304, 2008.
- [40] C. A. Isaac, C. J. Baker, T. Mortensen, D. P. van der Werf, and M. Charlton, “Compression of positron clouds in the independent particle regime,” *Phys. Rev. Lett.*, vol. 107, p. 033201, 2011.
- [41] J. R. Danielson and C. M. Surko, “Torque-balanced high-density steady states of single-component plasmas,” *Phys. Rev. Lett.*, vol. 94, p. 035001, 2005.
- [42] D. B. Cassidy, R. G. Greaves, V. E. Meligne, and A. P. Mills Jr, “Strong drive compression of a gas-cooled positron plasma,” *Applied Physics Letters*, vol. 96, no. 10, p. 101502, 2010.
- [43] C. M. Surko and R. G. Greaves, “Emerging science and technology of antimatter plasmas and trap-based beams,” *Physics of Plasmas*, vol. 11, no. 5, pp. 2333–2348, 2004.
- [44] M. Lund, “Comissioning of the ASACUSA positron beam line,” Master’s thesis, Aarhus University, 2009.
- [45] H. D. Thomsen, *Taming GeV Photons and Antimatter*. PhD thesis, Aarhus University, 2010.
- [46] J. Mills, A.P. and C. Murray, “Diffusion of positrons to surfaces,” *Applied physics*, vol. 21, no. 4, pp. 323–325, 1980.

- [47] J. P. Merrison, M. Charlton, P. Aggerholm, H. Knudsen, D. P. van der Werf, J. Clarke, and M. R. Poulsen, "Development and applications of time-bunched and velocity-selected positron beams," *Rev. Sci. Instrum.*, vol. 74, no. 7, pp. 3284–3292, 2003.
- [48] C. Piochacz and C. Hugenschmidt, "A novel setup for the pulsing and energy enhancement of a positron beam," *Journal of Physics: Conference Series*, vol. 443, no. 1, p. 012093, 2013.
- [49] P. Balling, D. Fregenal, T. Ichioka, H. Knudsen, H.-P. E. Kristiansen, J. Merrison, and U. I. Uggerhøj, "Perspectives for pulsed positrons," *Nucl. Instr. and Meth. B*, vol. 221, pp. 200–205, 2004.
- [50] K. Robbie, L. J. Friedrich, S. K. Dew, T. Smy, and M. J. Brett, "Fabrication of thin films with highly porous microstructures," *J. Vac. Sci. Technol. A*, vol. 13, no. 3, pp. 1032 – 1035, 1995.
- [51] K. Robbie, J. C. Sit, and M. J. Brett, "Advanced techniques for glancing angle deposition," *J. Vac. Sci. Technol. B*, vol. 16, no. 3, pp. 1115–1122, 1998.
- [52] R. Tait, T. Smy, and M. Brett, "Modelling and characterization of columnar growth in evaporated films," *Thin Solid Films*, vol. 226, no. 2, pp. 196 – 201, 1993.
- [53] K. Robbie, M. J. Brett, and A. Lakhtakia, "Chiral sculptured thin films," *Nature*, vol. 384, pp. 616–616, 12 1996.
- [54] A. Amassian, K. Kaminska, M. Suzuki, L. Martinu, and K. Robbie, "Onset of shadowing-dominated growth in glancing angle deposition," *Applied Physics Letters*, vol. 91, p. 173114, Oct 2007.
- [55] D. J. Poxson, F. W. Mont, M. F. Schubert, J. K. Kim, and E. F. Schubert, "Quantification of porosity and deposition rate of nanoporous films grown by oblique-angle deposition," *Applied Physics Letters*, vol. 93, no. 10, pp. –, 2008.
- [56] K. Kaminska, A. Amassian, L. Martinu, and K. Robbie, "Growth of vacuum evaporated ultraporous silicon studied with spectroscopic ellipsometry and scanning electron microscopy," *J. Appl. Phys.*, vol. 97, no. 1, 2005.
- [57] C. Buzea, K. Kaminska, G. Beydaghyan, T. Brown, C. Elliott, C. Dean, and K. Robbie, "Thickness and density evaluation for nanostructured thin films by glancing angle deposition," *Journal of Vacuum Science & Technology B*, vol. 23, no. 6, pp. 2545–2552, 2005.

- [58] C. Buzea, G. Beydaghyan, C. Elliott, and K. Robbie, "Control of power law scaling in the growth of silicon nanocolumn pseudo-regular arrays deposited by glancing angle deposition," *Nanotechnology*, vol. 16, no. 10, p. 1986, 2005.
- [59] R. Ferragut, S. Aghion, G. Tosi, G. Consolati, F. Quasso, M. Longhi, A. Galarneau, and F. Di Renzo, "Positronium production in engineered porous silica," *The Journal of Physical Chemistry C*, vol. 117, no. 50, pp. 26703–26709, 2013.
- [60] S. Tsoi, E. Fok, J. C. Sit, and J. G. C. Veinot, "Superhydrophobic, high surface area, 3-d sio2 nanostructures through siloxane-based surface functionalization," *Langmuir*, vol. 20, no. 24, pp. 10771–10774, 2004.
- [61] FEI, "Versa 3d dualbeam." <http://www.fei.com/products/dualbeam/versa-3d/>.
- [62] "SPIP." <http://www.imagemet.com/>.
- [63] W. Rasband, "Imagej." <http://imagej.nih.gov/ij/>, January 2014. 1.48v.
- [64] "Graphene Supermarket." <https://graphene-supermarket.com/>.
- [65] J. Lahiri, T. Miller, L. Adamska, I. I. Oleynik, and M. Batzill, "Graphene growth on ni(111) by transformation of a surface carbide," *Nano Letters*, vol. 11, no. 2, pp. 518–522, 2011.
- [66] J. Lahiri, T. S. Miller, A. J. Ross, L. Adamska, I. I. Oleynik, and M. Batzill, "Graphene growth and stability at nickel surfaces," *New Journal of Physics*, vol. 13, no. 2, p. 025001, 2011.
- [67] R. Addou, A. Dahal, P. Sutter, and M. Batzill, "Monolayer graphene growth on ni(111) by low temperature chemical vapor deposition," *Applied Physics Letters*, vol. 100, no. 2, 2012.
- [68] T. J. Booth, P. Blake, R. R. Nair, D. Jiang, E. W. Hill, U. Bangert, A. Bleloch, M. Gass, K. S. Novoselov, M. I. Katsnelson, and A. K. Geim, "Macroscopic graphene membranes and their extraordinary stiffness," *Nano Letters*, vol. 8, no. 8, pp. 2442–2446, 2008.
- [69] A. Reserbat-Plantey, D. Kalita, Z. Han, L. Ferlazzo, S. Autier-Laurent, K. Komatsu, C. Li, R. Weil, A. Ralko, L. Marty, S. Guéron, N. Bendiab, H. Bouchiat, and V. Bouchiat, "Strain superlattices and macroscale suspension of graphene induced by corrugated substrates," *Nano Letters*, vol. 14, no. 9, pp. 5044–5051, 2014.

- [70] Z. J. Qi, J. A. Rodríguez-Manzo, A. R. Botello-Méndez, S. J. Hong, E. A. Stach, Y. W. Park, J.-C. Charlier, M. Drndić, and A. T. C. Johnson, “Correlating atomic structure and transport in suspended graphene nanoribbons,” *Nano Letters*, vol. 14, no. 8, pp. 4238–4244, 2014.
- [71] X. Li, Y. Zhu, W. Cai, M. Borysiak, B. Han, D. Chen, R. D. Piner, L. Colombo, and R. S. Ruoff, “Transfer of large-area graphene films for high-performance transparent conductive electrodes,” *Nano Letters*, vol. 9, no. 12, pp. 4359–4363, 2009.
- [72] I. Al-Qaradawi, P. Sellin, and P. Coleman, “Tests of a diamond field-assisted positron moderator,” *Applied Surface Science*, vol. 194, no. 1–4, pp. 29 – 31, 2002.
- [73] S. Ulstrup, J. C. Johannsen, F. Cilento, J. A. Miwa, A. Crepaldi, M. Zaccagna, C. Cacho, R. Chapman, E. Springate, S. Mammadov, F. Fromm, C. Raidel, T. Seyller, F. Parmigiani, M. Grioni, P. D. C. King, and P. Hofmann, “Ultrafast dynamics of massive dirac fermions in bilayer graphene,” *Phys. Rev. Lett.*, vol. 112, p. 257401, 2014.
- [74] K. F. Canter, A. P. Mills, and S. Berko, “Efficient positronium formation by slow positrons incident on solid targets,” *Phys. Rev. Lett.*, vol. 33, pp. 7–10, 1974.
- [75] R. S. Brusa and A. Dupasquier, *Physics with Many Positrons, Proceedings of the International School of Physics “Enrico Fermi”, Course CLXXIV*. IOS Press, Amsterdam and SIF, Bologna, 2010.
- [76] R. H. Howell, I. J. Rosenberg, and M. J. Fluss, “Production of energetic positronium at metal surfaces,” *Phys. Rev. B*, vol. 34, pp. 3069–3075, 1986.
- [77] T. D. Steiger and R. S. Conti, “Formation of  $n=2$  positronium from untreated metal surfaces,” *Phys. Rev. A*, vol. 45, pp. 2744–2752, 1992.
- [78] A. P. Mills, L. Pfeiffer, and P. M. Platzman, “Positronium velocity spectroscopy of the electronic density of states at a metal surface,” *Phys. Rev. Lett.*, vol. 51, pp. 1085–1088, 1983.
- [79] A. P. Mills and L. Pfeiffer, “Desorption of surface positrons: A source of free positronium at thermal velocities,” *Phys. Rev. Lett.*, vol. 43, pp. 1961–1964, 1979.
- [80] R. M. Nieminen, *The Fate of Slow Positrons in Condensed Matter*. World Scientific, 2000.

- [81] A. P. M. Jr., “Thermal activation measurement of positron binding energies at surfaces,” *Solid State Communications*, vol. 31, no. 9, pp. 623 – 626, 1979.
- [82] M. R. Poulsen, M. Charlton, J. Chevallier, B. I. Deutch, L. V. Jorgensen, and G. Laricchia, “Thermal activation of positronium from thin ag(100) films in backscattering and transmission geometries,” *Journal of Physics: Condensed Matter*, vol. 3, no. 17, p. 2849, 1991.
- [83] A. P. Mills, “Positronium formation at surfaces,” *Phys. Rev. Lett.*, vol. 41, pp. 1828–1831, 1978.
- [84] J. Algers, P. Sperr, W. Egger, G. Kögel, and F. H. J. Maurer, “Median implantation depth and implantation profile of 3–18 keV positrons in amorphous polymers,” *Phys. Rev. B*, vol. 67, p. 125404, 2003.
- [85] D. B. Cassidy, T. H. Hisakado, H. W. K. Tom, and A. P. Mills, “Positronium formation via excitonlike states on si and ge surfaces,” *Phys. Rev. B*, vol. 84, p. 195312, 2011.
- [86] O. E. Mogensen, “Spur reaction model of positronium formation,” *The Journal of Chemical Physics*, vol. 60, no. 3, pp. 998–1004, 1974.
- [87] Y. Nagashima, Y. Morinaka, T. Kurihara, Y. Nagai, T. Hyodo, T. Shidara, and K. Nakahara, “Origins of positronium emitted from sio<sub>2</sub>,” *Phys. Rev. B*, vol. 58, pp. 12676–12679, 1998.
- [88] A. Greenberger, A. Mills, A. Thompson, and S. Berko, “Evidence for positronium-like bloch states in quartz single crystals,” *Physics Letters A*, vol. 32, no. 2, pp. 72 – 73, 1970.
- [89] P. Sferlazzo, S. Berko, and K. F. Canter, “Time-of-flight spectroscopy of positronium emission from quartz and magnesium oxide,” *Phys. Rev. B*, vol. 35, pp. 5315–5318, 1987.
- [90] S. Van Petegem, C. Dauwe, T. Van Hoecke, J. De Baerdemaeker, and D. Segers, “Diffusion length of positrons and positronium investigated using a positronbeam with longitudinal geometry,” *Phys. Rev. B*, vol. 70, p. 115410, 2004.
- [91] L. Liskay, F. Guillemot, C. Corbel, J.-P. Boilot, T. Gacoin, E. Barthel, P. Pérez, M.-F. Barthe, P. Desgardin, P. Crivelli, U. Gendotti, and A. Rubbia, “Positron annihilation in latex-templated macroporous silica films: pore size and ortho-positronium escape,” *New Journal of Physics*, vol. 14, no. 6, p. 065009, 2012.

- [92] D. B. Cassidy, T. H. Hisakado, V. E. Meline, H. W. K. Tom, and A. P. Mills, "Delayed emission of cold positronium from mesoporous materials," *Phys. Rev. A*, vol. 82, p. 052511, 2010.
- [93] S. Mariazzi, P. Bettotti, and R. S. Brusa, "Positronium cooling and emission in vacuum from nanochannels at cryogenic temperature," *Phys. Rev. Lett.*, vol. 104, p. 243401, 2010.
- [94] C. He, S. Wang, Y. Kobayashi, T. Ohdaira, and R. Suzuki, "Role of pore morphology in positronium diffusion in mesoporous silica thin films and in positronium emission from the surfaces," *Phys. Rev. B*, vol. 86, p. 075415, 2012.
- [95] A. P. Mills and W. S. Crane, "Beam-foil production of fast positronium," *Phys. Rev. A*, vol. 31, pp. 593–597, 1985.
- [96] P. F. Barker and M. Charlton, "Directed fluxes of positronium using pulsed travelling optical lattices," *New Journal of Physics*, vol. 14, no. 4, p. 045005, 2012.
- [97] T. S. Pedersen, A. H. Boozer, W. Dorland, J. P. Kremer, and R. Schmitt, "Prospects for the creation of positron–electron plasmas in a non-neutral stellarator," *Journal of Physics B: Atomic, Molecular and Optical Physics*, vol. 36, no. 5, p. 1029, 2003.
- [98] D. M. Chen, K. G. Lynn, R. Pareja, and B. Nielsen, "Measurement of positron reemission from thin single-crystal w(100) films," *Phys. Rev. B*, vol. 31, pp. 4123–4130, 1985.
- [99] M. R. Poulsen, G. Laricchia, M. Charlton, K. O. Jensen, and A. B. Walker, "Implantation and diffusion in thin films," *Mater. Sci. Forum*, vol. 105–110, p. 1431, 1992.
- [100] J. P. Merrison, H. Bluhme, J. Chevallier, B. I. Deutch, P. Hvelplund, L. V. Jørgensen, H. Knudsen, M. R. Poulsen, and M. Charlton, "Hydrogen formation by proton impact on positronium," *Phys. Rev. Lett.*, vol. 78, pp. 2728–2731, 1997.
- [101] A. Vehanen, K. Saarinen, P. Hautojärvi, and H. Huomo, "Profiling multilayer structures with monoenergetic positrons," *Phys. Rev. B*, vol. 35, pp. 4606–4610, 1987.
- [102] A. P. Mills, Jr., E. D. Shaw, R. J. Chichester, and D. M. Zuckerman, "Positronium thermalization in  $\text{SiO}_2$  powder," *Phys. Rev. B*, vol. 40, pp. 2045–2052, 1989.

- [103] D. B. Cassidy, S. H. M. Deng, H. K. M. Tanaka, and A. P. Mills, Jr., “Single shot positron annihilation lifetime spectroscopy,” *Appl. Phys. Lett.*, vol. 88, p. 194105, 2006.
- [104] D. Cassidy and A. M. Jr., “A fast detector for single-shot positron annihilation lifetime spectroscopy,” *Nuclear Instruments and Methods in Physics Research Section A: Accelerators, Spectrometers, Detectors and Associated Equipment*, vol. 580, no. 3, pp. 1338 – 1343, 2007.
- [105] E. Soininen, A. Schwab, and K. G. Lynn, “Positron-induced auger-electron study of the ge(100) surface: Positron thermal desorption and surface condition,” *Phys. Rev. B*, vol. 43, pp. 10051–10061, 1991.
- [106] H. H. Jorch, K. G. Lynn, and I. K. MacKenzie, “Anomalous temperature dependence of the positron diffusion constant in ge,” *Phys. Rev. Lett.*, vol. 47, pp. 362–366, 1981.
- [107] M. Eldrup, A. Vehanen, P. J. Schultz, and K. G. Lynn, “Positronium formation and diffusion in a molecular solid studied with variable-energy positrons,” *Phys. Rev. Lett.*, vol. 51, pp. 2007–2010, 1983.
- [108] A. P. Mills, E. D. Shaw, M. Leventhal, R. J. Chichester, and D. M. Zuckerman, “Thermal desorption of cold positronium from oxygen-treated al(111) surfaces,” *Phys. Rev. B*, vol. 44, pp. 5791–5799, 1991.
- [109] Y. Nagashima, M. Kakimoto, T. Hyodo, K. Fujiwara, A. Ichimura, T. Chang, J. Deng, T. Akahane, T. Chiba, K. Suzuki, B. T. A. McKee, and A. T. Stewart, “Thermalization of free positronium atoms by collisions with silica-powder grains, aerogel grains, and gas molecules,” *Phys. Rev. A*, vol. 52, pp. 258–265, 1995.
- [110] S. Mariazzi, A. Salemi, and R. S. Brusa, “Positronium cooling into nanopores and nanochannels by phonon scattering,” *Phys. Rev. B*, vol. 78, p. 085428, 2008.
- [111] S. Mariazzi, P. Bettotti, S. Larcheri, L. Toniutti, and R. S. Brusa, “High positronium yield and emission into the vacuum from oxidized tunable nanochannels in silicon,” *Phys. Rev. B*, vol. 81, p. 235418, 2010.
- [112] H. Saito and T. Hyodo. Kluwer Academic Publishers, Dordrecht, 2001.
- [113] G. W. Ford, L. M. Sander, and T. A. Witten, “Lifetime effects of positronium in powders,” *Phys. Rev. Lett.*, vol. 36, pp. 1269–1272, 1976.

---

# List of Figures

1.1	The positron was first observed by Anderson in 1933, who interpreted the loss of energy of a positive particle passing through a lead plate in a magnetic field as being due to a positron entering from below. From [2]. . . . .	2
1.2	The $n = 1$ and $n = 2$ energy levels of Ps separated into singlet and triplet states. The Lyman- $\alpha$ transition driven by the UV laser in the Ps cooling experiment described in Chapter 6 is also shown. Adapted from [5]. . . . .	4
1.3	Feynman diagrams for the decay of para-Ps (left) into two photons and ortho-Ps into three photons (right). The time is running upwards. . . . .	5
2.1	Overview of the Aarhus positron beam line. The first section contains the source and rare gas moderator, whereas the second section includes the trap and the buncher. Modified from original FPSI drawing. . . . .	7
2.2	The electromagnets and the electrodes comprising the Aarhus positron beamline. Enlarged is the moderator geometry to the left showing the solid neon layer evaporated onto the cone shaped gold-plated copper electrode, and to the right the trap electrode configuration with the azimuthally segmented electrode that provided the rotating quadrupole field to one end of the plasma. Modified from original FPSI drawing. . . . .	8
2.3	The positron reemission probability for positrons impinging upon solid neon at 5K for a given positron impact energy. The dip just above zero and the characteristic energies pointed out by arrows are explained in the text. From [25]. . . . .	10

2.4	In (a) the structure of the potential well in the three stages of decreasing buffer gas pressure is shown. The positrons undergo the transition "A", "B" and "C" and become trapped in the third, low pressure stage (from [22]). (b) shows the cross-sections for Ps formation (filled circles) and electronic excitation of the $a^1\Pi$ state (open triangles) in $N_2$ by positron impact at a given energy. The dashed- and full line mark the threshold for electronic excitation and Ps formation, respectively (from [31] who summarises results from [32]). . . . .	13
2.5	When a new moderator is grown, the old moderator is first evaporated (at $t = 0$ ) by heating the cold head to $\sim 25$ K. After cooling down again the $\gamma$ -ray count rate (black) change as the temperature (red) and the neon pressure (blue) is set by the LabVIEW controlled moderator growth process described in the text. . . . .	18
2.6	The transverse profile of the continuous beam is shown in (a), while (b) shows the data of a retarding field analysis of the continuous beam. The latter constitutes a measurement of the parallel energy and energy spread of the positron beam. . . . .	19
2.7	The bunched beam profile after the rotating wall compression is shown in (a). In (b) the frequency of the rotating wall has been optimised in terms of the transverse $1\sigma$ radius of the beam and the central density normalised to the density when the rotating wall is off-resonance. . . . .	21
2.8	(a) The lifetime of the positrons in the trap is measured by varying the store time and measure the peak height in the NaI detector. In (b) the energy of the positron plasma is found from a retarding field analysis. . . . .	23
2.9	The buncher sits inside the extraction solenoid and the distance to the time focus at the target is $z_0 = 88$ cm as shown in (a). In (b) the three bunching potentials are shown for an initial positron energy of 12 eV. . . . .	25
2.10	Positron bunching simulation with two initial positron energies, 12 eV in (a) and (c) and 24 eV in (b) and (d). Both time and energy profiles are simulated. The black curve is the un-bunched profile, and the other colours are as given in Fig. 2.9b. . . . .	26
2.11	The delay of the bunching potential has been optimised in a measurement as shown in (a) to give the smallest pulse width and the largest peak value. The time compression is illustrated in (b), where the peak normalised time profiles as measured for the initial trap settings, the optimised trap settings and the bunched beam are shown. . . . .	28

2.12	The timing system is illustrated in (a), where TrigOut serves as a pre-trigger for all the hardware timing. In (b) the print board for the trigger selection is shown. . . . .	30
3.1	The meso-structured silica films are grown on a rotating carbon foil at a glancing angle of incidence, $\theta$ . The carbon foil is held by an Al-ring [15]. . . . .	32
3.2	The meso-structured silica films starts to grow from discrete spots (a). As shadowing effects start to set in, pillars will evolve that are leaning towards the deposition source. If the sample is rotated simultaneously to the deposition, then the pillars become vertical is the rotation is rapid (c). If the rotation is slow, the spirals will occur (d). . . . .	33
3.3	(a) The reflection geometry in which the positrons hit the silica thin films directly. (b) The transmission geometry in which the positrons hit the carbon foil first and penetrate through to the meso-structured silica from transmission Ps formation. . . . .	36
3.4	The meso-structured silica films imaged by SEM from a top view for three different samples. (a) Shows a sample with $\Delta t_{\perp} = 1000$ nm, $\theta = 7^{\circ}$ and $\phi = 6.0$ rpm. For the sample in (b) $\Delta t_{\perp} = 1150$ nm, $\theta = 12^{\circ}$ and $\phi = 6.0$ rpm and for the sample in (c) $\Delta t_{\perp} = 840$ nm, $\theta = 17^{\circ}$ and $\phi = 6.0$ rpm. . . . .	37
3.5	The column diameter distribution is shown in (a) for the film of normal thickness 1000 nm. (b) Shows a FFT of the SEM image in Fig. 3.4a, which is used to estimate the columns spacing. See the text. . . . .	38
3.6	Radial profiles of the FFT's of the SEM images in Fig. 3.4. The Gaussian fits are used to extract the typical spacing between the pillars in the meso-structured samples. . . . .	39
3.7	The meso-structured silica films imaged by SEM from a top view for two different samples. (a) Shows a sample with $\Delta t_{\perp} = 1000$ nm, $\theta = 7^{\circ}$ and $\phi = 6.0$ rpm. For the sample in (b) $\Delta t_{\perp} = 1324$ nm, $\theta = 7^{\circ}$ and the film was grown without sample rotation. . . . .	40
3.8	SEM images of two different meso-structured silica films from a top view (a) and (c) and in cross section (b) and (d). In (a) and (b) the $\Delta t_{\perp} = 1000$ nm, $\theta = 7^{\circ}$ and 6.0 rpm sample is seen, whereas a sample with $\Delta t_{\perp} = 1025$ nm, $\theta = 12^{\circ}$ , $\phi = 0$ is seen in (b) and (d). . . . .	41
3.9	SEM images (a) and (b) and a TEM image (c) of a sample which has a non-porous layer (30 nm) of silica between the carbon and the porous silica ( $\Delta t_{\perp} = 1370$ nm, $\theta = 7^{\circ}$ and $\phi = 6.0$ rpm). . . . .	42

3.10	(a) Shows the hole over which the graphene is to be placed. (b) Shows an attempt to transfer the graphene from the Ni to the stainless steel holder and is supported by water. (c) Shows a graphene film with a meso-structured silica film on top. . . . .	44
4.1	Positron implantation into a solid (metal). The processes involved are described in the text. Adapted from [80]. . . . .	48
4.2	(a) Makhovian profiles for positron impact on amorphous carbon and silica at three positron implantation energies. (b) Mean positron implantation depth for carbon, silica and germanium. The mean depth only depends on the density of the material by Eq. 4.5. . . .	51
4.3	Modified positron implantation profiles of thin meso-structured silica films grown onto carbon foils of varying thickness. The carbon foil thicknesses are: (a) 20 nm, (b) 10 nm, (c), 5 nm and (d) 1 nm. 61	
4.4	Stopping probabilities for the transmission geometry within (a) the first 40 nm, (b) the first 80 nm and (c) the first 120 nm of the meso-structured silica, corresponding to 5, 10 and 15% of the layer thickness, respectively. The carbon foil thickness is given in the legend. 62	
4.5	Positron implantation profiles at a range of positron energies in the reflection geometry. (a) Shows the onset of positron transmission through the sample, while (b) illustrates the implantation profiles at the positron energies that yield the highest stopping in the region close to the carbon foil, where most cooling is expected. 63	
4.6	Comparison of positron annihilation energy spectra with 0% and 100% Ps formation and emission into vacuum. The spectra are normalised to a peak height of one. From [15]. . . . .	65
4.7	SSPALS spectra for positrons impinging upon a thin meso-structured silica sample at three different implantation energies. The spectra are normalised to a peak height of one. From [16]. . . . .	66
5.1	The extraction solenoid provides a longitudinal magnetic field that transports the positrons to the interaction chamber, where alignment is done using the empty target position at the bottom of the target holder. The positron energy is controlled by applying a potential difference between the grounded tungsten mesh and the negatively biased target holder. . . . .	70
5.2	The temperature dependency of the Ps formation fraction, $f$ , for the Ge(111) surface. The three data sets were taken under different temperature conditions as described in the text, and the solid red line is an attempt to estimate the data based on Eq. 4.3. The target bias was set to 10V for the reemitted positrons to impinge the surface again. . . . .	72

5.3	The Ps formation fraction as a function of the positron implantation energy for Ge(111) at 1063K and for mica at room temperature. The data has been fitted to Eq. 4.9 . . . . .	74
5.4	The Ps formation fraction in reflection as a function of the positron implantation energy for three meso-structured SiO <sub>2</sub> films produced with different normal thicknesses and the same glancing angle of deposition ( $\theta = 7^\circ$ ) and rotational frequency ( $\phi = 6.0$ rpm). The data has been fitted to Eq. 4.9 but with a constant parameter added to it as described in the text. . . . .	76
5.5	The Ps formation fraction in reflection as a function of the positron implantation energy for three meso-structured SiO <sub>2</sub> films. The film with $\Delta t_\perp = 300$ nm is shown again for comparison, the other two samples have the same normal thickness and rotation frequency, but different glancing angles. The data has been fitted to Eq. 4.9 but with a constant parameter added to it as described in the text. . . . .	78
5.6	The Ps formation fraction as a function of the positron implantation energy for all the five samples studied in reflection. . . . .	79
5.7	The Ps formation fraction as a function of the positron implantation energy for three different meso-structured silica samples positioned in the transmission geometry and for a plain carbon foil. Gaussian fits are performed to estimate the peak values of the Ps formation fraction for Ps formed in transmission. . . . .	80
5.8	The Ps formation fraction as a function of the positron implantation energy for three structured silica films in the transmission geometry, and for a plain carbon foil. The formation occurs in reflection from the carbon foil at low energy in all cases, and the data has been fitted to Eq. 4.9. . . . .	81
5.9	Two independent measurements of the Ps formation fraction in transmission as a function of the positron implantation energy for the same sample. Also shown is a measurement of the Ps formation in a plain carbon foil. (a) Shows the Ps formation at low energy with fits to Eq. 4.9. (b) Shows the total range of the measurements, and Gaussian fits are used to estimate the maximum Ps formation fraction. . . . .	82
5.10	A simple model is developed to describe the Ps formation fraction in transmission. The model is here compared to the data for two difference samples. . . . .	83
5.11	The delayed fraction $f_d$ as a function of the positron implantation energy in (a) the reflection geometry and (b) the transmission geometry for a sample consisting of vertical pillars, <i>i.e.</i> with $\theta = 7^\circ$ , $\phi = 6.0$ rpm, and $\Delta t_\perp = 1000$ nm. These measurements were conducted at UCL and are presented in [16]. . . . .	85

5.12	The delayed fraction $f_d$ as a function of the positron implantation energy measured for a meso-structured silica sample with $\theta = 7^\circ$ , $\phi = 6.0$ rpm, and $\Delta t_\perp = 1370$ nm and a 30 nm layer of bulk silica on top of the carbon foil. Two independent measurements of the same target conducted at Aarhus University. . . . .	87
6.1	Overview of the experimental setup used to measure the cooling of Ps in the meso-structured silica film. The UV and green laser pulses overlap with the Ps cloud both in space and time, and the two-photon resonance enhanced ionisation is measured using SS-PALS. See the text for a detailed description. Modified from original drawing by Adam Deller. . . . .	94
6.2	The four geometries in which the Ps energy is measured. Ps is formed in reflection (a) and (b) and in transmission in (c) and (d). The energy of Ps is measured in the transverse direction in (a) and (c), where both lasers are directed along the sample surface. The longitudinal energy of Ps is probed in (b) and (d), where the UV laser is pointed along the positron beam axis, while the green laser is still directed along the surface of the sample. . . . .	95
6.3	The relative change $S$ in the delayed fraction $f_d$ as a function of the UV laser wavelength $\lambda$ increases around the Lyman- $\alpha$ transition wavelength and reveals the Doppler broadened resonance for five positron impact energies. The solid lines are Gaussian fits. . . . .	97
6.4	The transverse energy of the Ps emitted in the reflection geometry from meso-structured silica is plotted as a function of positron implantation energy. The fit is an estimate of the data based on Eq. 6.4. . . . .	98
6.5	The Doppler shifted resonance shapes for Ps formed in reflection is used to find the longitudinal energy component at four different positron implantation energies. The amplitude of the profiles are larger when the laser-Ps interaction time is longer <i>i.e.</i> when the transverse Ps energy is lower. The solid lines are Gaussian fits. . .	99
6.6	The longitudinal Ps energy and energy spread are plotted as a function of positron implantation energy. The fits are estimates of the data based on Eq. 6.4. . . . .	99
6.7	Delay scan in the transmission geometry. The positron implantation energy is 1.3 eV and the emission time is the same as that found in the reflection geometry when the lasers were directed along the silica surface. . . . .	101
6.8	Doppler broadened resonance shapes for the Lyman- $\alpha$ transition for Ps formed in transmission. The solid lines represent Gaussian fits that are used to extract the transverse Ps energy. . . . .	102

6.9	The transmission-formed Ps transverse energy plotted as a function of positron implantation energy. The red line represents a linear fit of the data to guide the eye. . . . .	102
6.10	The double peak structure of these Doppler profiles are due to the reflection of ~ 90% of the UV laser, when probing the longitudinal Ps energy. Thus both a blue shift and a red shift is seen. . . . .	103
6.11	The longitudinal component of the Ps energy and energy spread as extracted from the Doppler shifted double peak resonance structures, and plotted as a function of positron implantation energy. .	104



---

# List of Tables

2.1	Summary of the default values of the magnetic positron transporting system in the main part of the beamline (source, moderator and trap). . . . .	13
2.2	Default trap parameters after optimisation of the timing output. All the potentials are listed in volts, and the values are as set by the LabVIEW control program. It should be noted that some mismatch between the set voltages and the actual voltages applied to the trap electrodes have been observed. . . . .	16
5.1	Parameters for the fits to Eq. 4.9 of the data shown in Figs. 5.4 and 5.5. The value of $\chi^2/\text{ndf}$ is close to one for all the fits. . . . .	77
5.2	Parameters for the Gaussian fits used to estimate the Ps formation fraction in transmission as shown in Fig. 5.7. The carbon foil does not have a layer of silica grown onto it and $\Delta t_{\perp}$ in this table represents the real thickness for the carbon foil. . . . .	81